

博士論文

**Development of production methods of submillimeter-long
carbon nanotubes**

(サブミリメートル長カーボンナノチューブの合成法の開発)

CHEN Zhongming

陳 忠明

A thesis presented in partial fulfilment of
the requirements for the degree of
DOCTOR OF ENGINEERING

東京大学大学院工学系研究科化学システム工学専攻

Department of Chemical System Engineering

The University of Tokyo

August 2014

Content

Chapter 1 - Introduction	3
1.1 Thesis Organization.....	3
1.2 Types of Carbon Nanotubes (CNTs).....	5
1.3 Synthesis of CNTs by chemical vapor deposition (CVD)	6
1.3.1 Gas phase synthesis by floating catalysts	8
1.3.2 On substrate synthesis by supported catalysts	9
1.3.3 Fluidized bed synthesis by supported catalysts	12
1.4 Mechanism for CNT growth by supported catalysts	12
1.4.1 Root growth	14
1.4.2 Tip growth.....	18
1.5 Characterization of CNTs	19
1.5.1 Raman spectroscopy	20
1.5.2 Electron microscopy	21
1.5.3 Thermogravimetry	22
1.5.4 Brunauer–Emmett–Teller (BET) surface area measurement.....	24
1.6 Application of CNTs to the electric storage devices	24
References	26
Chapter 2 - Methane-assisted CVD yielding millimeter-tall single-wall CNTs (SWCNTs) of small diameter	35
2.1 Introduction	35
2.2 Methods	37
2.3 Overview of CH ₄ -assisted CVD yielding taller vertically aligned (VA)-SWCNTs of higher quality under a wider range of catalyst conditions.....	38
2.4 Effects of CH ₄ during catalyst annealing and CVD	42
2.5 Effects of the addition of CH ₄ during the catalyst annealing on the microstructure of the Fe particles.....	45
2.6 Effect of the addition of CH ₄ during CVD on the diameter of the SWCNTs	51
2.7 Possible role of CH ₄ during catalyst annealing and during CVD.....	54
2.8 Confirmation of absence of the CH ₄ steam reforming effect by gas chromatography.....	56
2.9 Effect of different CH ₄ concentration on SWCNTs synthesis	58

2.10 Effects of other hydrocarbons: Catalyst annealing under H ₂ with CH ₄ , C ₂ H ₄ , and C ₂ H ₂	56
2.11 Cost analysis of the source gases for the production of CNTs	65
2.12 Conclusions	66
References	68
Chapter 3 - Fluidized bed CVD (FBCVD) of submillimeter-long CNTs using an internal heat-exchange reactor.....	71
3.1 Introduction	71
3.2 Methods	73
3.3 Basic design and temperature profile of the FBCVD.....	76
3.4 Semi-continuous production of CNTs and the resulting CNT structure	79
3.5 Conclusions	86
References	87
Chapter 4 - Semi-continuous production of CNTs with smaller diameter using an internal heat-exchange reactor.....	90
4.1 Introduction	90
4.2 Methods	91
4.3 Controlling the amount and size of Fe particles	92
4.4 Effects of catalyst feed on the production amount of CNTs	94
4.5 Keeping small catalyst particles active by moderating C ₂ H ₂ feed and yielding sub-millimeter-long FWCNTs with reduced diameter and improved purity	96
4.6 Conclusions	107
References	108
Chapter 5 – Conclusions	111
Supporting information	115
Acknowledgements	121
Publication list.....	123

Chapter 1 - Introduction

1.1 Thesis Organization

The beginning of this thesis will give a short introduction on the background of carbon nanotubes (CNTs), including: (1) a general introduction for different types of CNTs, such as single-wall CNTs (SWCNTs) and multi-wall CNTs (MWCNTs); (2) synthesis methods of CNTs by chemical vapor deposition (CVD), mainly including gas phase synthesis by floating catalysts, on substrate and fluidized bed synthesis by supported catalysts; (3) mechanisms for CNT growth, including tip growth and root growth; (4) methods for characterization of CNTs, including Raman spectroscopy, electron microscopy, thermogravimetry (TG), and Brunauer–Emmett–Teller (BET) surface area measurement; and (5) applications of CNTs to electric storage devices.

Chapter 2 will present the results of research conducted in this PhD study. Chapter 2 is about the newly developed, methane assisted CVD method, which yields millimeter-long SWCNTs of small diameter. H_2 is widely used as a carrier gas in various CVD processes for CNT production and thus the use of low purity H_2 instead of high purity H_2 is effective in reducing the production cost. In the naphtha cracking process, H_2 gas is produced as a byproduct in addition to various low carbon number hydrocarbons (CH_4 , C_2H_4 , C_2H_6 , C_3H_6 , C_3H_8 , etc.). H_2 is separated by cryogenic distillation from this mixture, but some CH_4 remains in the separated H_2 . This section examines the use of 96 vol% pure H_2 containing 4 vol% CH_4 for the rapid growth of millimeter-tall SWCNTs, and compares the results with those obtained using 99.999 vol%-pure H_2 . I examined whether the impurity (CH_4) disturbs the SWCNT growth, and unexpectedly found that CH_4 has significant effect in suppressing the coarsening

of the catalyst particles and growing taller vertically aligned SWCNTs (VA-SWCNTs) with small diameters. The role of CH₄ in improving the SWCNT growth is also discussed. These effects were observed only for CH₄, and not for C₂H₄ or C₂H₂. CH₄-assisted CVD is an efficient and practical method that uses H₂ containing CH₄ which is available as a byproduct in chemical plants.

Unfortunately, the synthesis of CNTs by CVD on flat substrates, which provide 2-dimensional (2D) reaction space, can yield CNTs at a production scale as small as a few tens of g m⁻² even if CNTs are grown long to a millimeter-scale. This is a major obstacle for the industrial applications of such CNTs. Therefore, the use of 3-dimensional (3D) reaction space such as fluidized bed CVD (FBCVD) instead of 2D surfaces is highly required. Chapter 3 will present the application of an internal heat-exchange reactor to FBCVD, which realizes the synthesis of CNTs with enhanced productivity. In our lab, an original FBCVD was developed, which realized semi-continuous production of submillimeter-long few-wall CNTs (FWCNTs) from C₂H₂ with a subsecond residence time and a high carbon yield $\geq 70\%$ [1]. But the high gas feed causes insufficient heating of the bead bed when scaled up. This time, a new FBCVD reactor is designed and developed, and its performance in producing submillimeter-long CNTs at improved productivity is examined.

FBCVD using the internal heat-exchange reactor yielded CNTs at an improved amount but with an increased diameter of about 11 nm in average. Chapter 4 will present results on the careful control over the catalyst and CVD condition that decreases the diameter of CNTs while keeping the high productivity. By reducing the catalyst feed, small Fe catalyst particles can be prepared but such catalysts can be easily deactivated. By reducing the carbon feed (i.e., C₂H₂) to a moderate concentration, deactivation of such catalysts is prevented, and CNTs with smaller average diameter of ~6.5 nm are produced at a fair productivity.

Finally, a summary of this thesis is provided by discussing the importance of designing CNT production processes logically based on the fundamental understanding of CNT growth process. Remaining issues and future perspectives are presented.

1.2 Types of Carbon Nanotubes (CNTs)

Many scientists put their interests in nanoscale materials, which were defined as having at least one dimension less than 100 nm. They have unique properties and application potentials, differently from their bulk counterparts. Examples that familiar to us contain zero-dimensional nanoparticles [2] such as fullerene, one-dimensional nanowires/nanotubes [3-5] such as CNTs, and two-dimensional (2D) nano-sheets such as graphene [6-8]. With these kinds of structures, electrons can be confined in one or more dimensions, thus novel electrical, optical, and magnetic properties can be achieved in nanostructures. Since S. Iijima, using high resolution transmission electron microscope (HRTEM) and electron diffraction, reported the existence of helical carbon microtubules (now called nanotubes) [9], they have attracted great attentions.

The structure of pure SWCNTs can be visualized as rolled-up a tubular shell of graphene sheet into a cylindrical shape, which is made up of benzene type hexagonal rings of carbon atoms (a schematic of a SWCNT is shown in Figure 1-1a) [10]. Because SWCNTs generally have a large length-to-diameter ratio (aspect ratio) of 10^3 -or more, they are treated as nearly one-dimensional (1D) structures [11]. Depending on the chirality along the graphene sheet, either semiconducting or metallic electronic states are created [12]. Both experiments and

theory have shown that SWCNTs possess high mobility (on the order of $100,000 \text{ cm}^2 \text{ V}^{-1} \text{ s}^{-1}$) [13], high conductivity (up to $400,000 \text{ S cm}^{-1}$), and, for semiconducting nanotubes, tube diameter-dependent band gap ($E_{\text{gap}} \approx 1/R_{\text{tube}}$) [14, 15]. MWCNTs are larger and consist of many SWCNTs stacked one inside the other [10]. As shown in Figure 1-1b, according to the walls of tubes, they can be further clarified as double wall CNTs (DWCNTs) [16] and triple-wall CNTs [17].

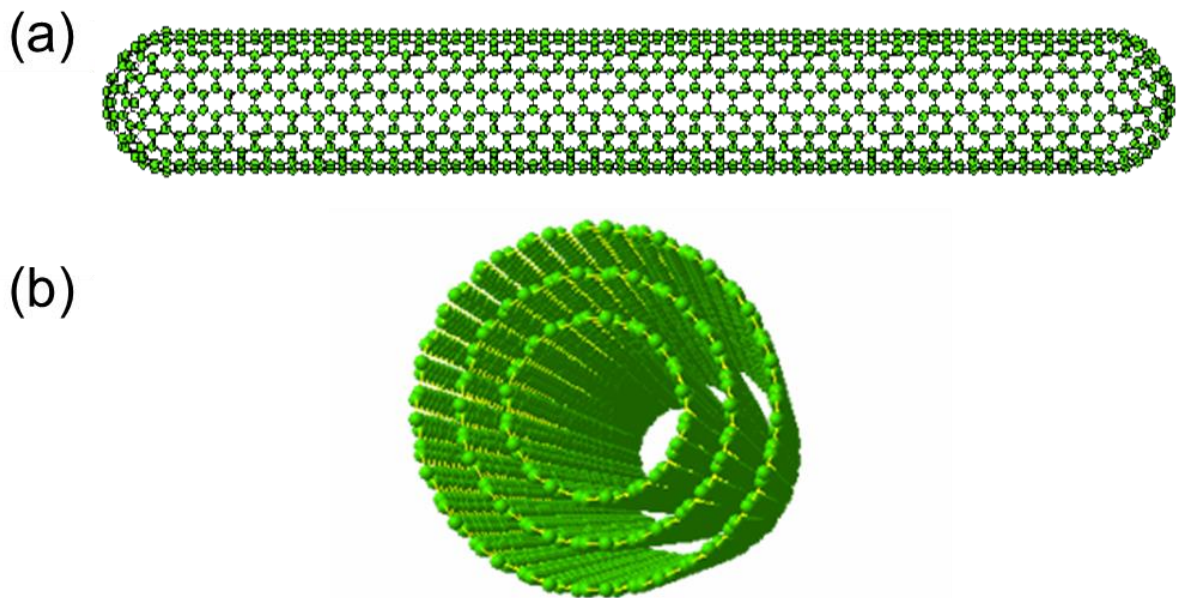


Figure 1-1. Schematics of different types of CNTs: a SWCNT (a) and a MWCNT (b)

(Reprinted with permission from {Ref. [18], <http://www.photon.t.u-tokyo.ac.jp/index-j.html>}).

1.3 Synthesis of CNTs by chemical vapor deposition (CVD)

Since the reported of their synthesis by arc-discharge method by Iijima [9], CNTs aroused world-wide interests on the synthesis methods and applications. Various techniques have been developed and applied to synthesize CNTs with different structures and

morphologies in laboratory scale. Typically, three major methods have been developed for CNT synthesis: arc discharge [19, 20], laser ablation [21], and chemical vapor deposition (CVD) [22-25]. Catalysts, carbon sources, and sufficient energy are the basic elements for the formation of CNTs. In the arc discharge and laser ablation methods, in order to make carbon atoms sublimated from bulk carbon and assemble them into CNTs, it is important to heat the carbon source to a high temperature of several thousand degree C. Because CNTs are synthesized at a very high temperature, CNTs are usually in a high degree of graphitization. However, the requirement for high-energy sources (i.e. arc discharge and laser) and the use of solid carbon sources pose difficulties for continuous large-scale production. On the other hand, in CVD method, gaseous carbon-containing molecules such as hydrocarbon and alcohol are used as the carbon source, and the decomposition of such source gases are promoted by catalysts. The CVD process can thus be operated under mild conditions, such as atmospheric pressure and moderate temperatures ~ 1000 °C, with an ease for continuous feeding of the carbon source. The structure of CNTs, for example, their diameter, length, and alignment, can be more efficiently controlled by a catalyst, either floating in the gas phase or supported on substrates/powders. Therefore, CVD process, which has the advantages of mild operating conditions, easy feed of gaseous carbon sources, and controllable synthesis, is the most promising method for the production of CNTs with increased scales to meet the real applications.

In the CVD process, the characteristics of catalysts largely affect the structure and quality of CNTs as well as the process yield. Nanoparticles of transition metals, such as Fe, Co, Ni, are commonly used as catalysts to synthesize CNTs. It has been found that the structure of CNTs was determined by the size and chemical composition of the metal catalysts. Here, I will first introduce the popular types of CVD methods for CNT synthesis, including

gas phase synthesis by floating catalysts, on-substrate synthesis by supported catalysts, and FBCVD using supported catalysts on powders.

1.3.1 Gas phase synthesis by floating catalysts

This method uses catalyst particles floating in the gas phase for CNT preparation, it was named as floating catalyst CVD method. This method is ideal for continuous operation in which catalyst and carbon source vapors are fed directly to the CVD reactor without any preparation stage and catalyst nanoparticles nucleate and start to grow CNTs. It is also ideal for the efficient use of the three-dimensional space of the reactor. Figure 1-2 shows the schematic for CNT synthesis by floating catalysts.

Many groups put their interests in the gas phase CNT synthesis by floating catalyst method. Cheng and co-workers realized the synthesis of SWCNTs by using catalytic pyrolysis of hydrocarbons and ferrocene as the precursor for catalyst [26, 27]. Nikolaev et al. used CO as carbon feedstock and realized the gas phase catalytic production of SWCNTs. This method resulted in no amorphous carbon overcoating on the product nanotubes due to the formation of CO₂ from CO during CVD [28]. Kauppinen and coworkers studied in detail the mechanism of the formation of SWCNTs by an aerosol method (floating catalyst) in which aerosol catalysts are preformed and introduced to the CVD zone for CNT synthesis [29, 30]. As for the CNT synthesis by floating catalyst, many of the researchers also studied the effect of sulfur additives on the structure and yield of CNTs [32-37]. The basic research for CNT synthesis by floating catalyst CVD is also ongoing in our lab.

Floating catalyst method is one of the promising ways for the synthesis of CNTs with increased scale to meet the commercial application. However, the drawback of this method is

the difficulty in preventing the aggregation of catalyst nanoparticles. Floating catalyst CVD has been used for carbon fibers including "vapor grown carbon fibers (VGCFs) [38]" with a large diameters of > 100 nm. But when it is applied to grow SWCNTs with a diameter ~ 1 nm, individual CNTs of a same length have a weight 4 orders of magnitude smaller than that for VGCFs, resulting in a much smaller productivity. Catalyst nanoparticles, as small as a few nm in diameter, quickly collide, aggregate and/or coalesce with each other due to their quick Brownian diffusion. Thus the concentration of catalyst nanoparticles cannot be increased and the productivity is limited in the synthesis of CNTs by this method.

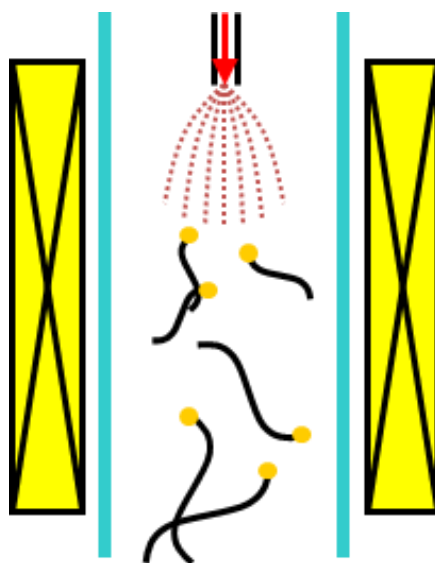


Figure 1-2. A schematic for the gas phase CVD synthesis of CNTs by floating catalysts

1.3.2 On substrate synthesis by supported catalysts

Compared with aggregated CNTs, vertical aligned CNTs (VA-CNTs) on flat substrates can have good electrical and thermal conductivities due to their uniform orientation. As for

VA-MWCNTs, they were first realized by Li et al. using Fe catalysts supported on porous SiO₂ [39]. Several years were required for the synthesis of VA-SWCNTs, which were first reported by Maruyama and coworkers using the Co/Mo bimetallic catalyst and alcohol carbon source. Catalysts were prepared by dip-coating the ethanol solution of Co acetate and Mo acetate on quartz glass substrates, followed by baking in air at 400 °C to remove the acetate and oxidize the metals, and finally reducing the metals under a H₂ environment at the CVD temperature ~ 800 °C. The density of catalysts was about 10⁵/μm² and with diameters of approximately 1.5 nm [40]. It is believed that this high catalyst density leads to the vertically-aligned growth of SWCNTs [41]. Catalyst preparation in solution (Figure 1-3b) is widely used and practical for CNT synthesis.

Hata and coworkers reported *super-growth* of VA-SWCNTs by the water assisted CVD method [42], which aroused lots of interests. Catalysts were prepared by sputtering metal thin films (Fe, Fe/Al, Fe/Al₂O₃, Co/Al₂O₃) on Si wafers. The SWCNT/catalyst weight ratio exceeds 500, more than 100 times as high as that of the high-pressure carbon monoxide (HiPco) process [43,44]. In our lab, for the growth of VA-SWCNTs on flat substrates with supported catalyst have been studied basically and systematically [45-54]. Catalyst was prepared by first sputtering Al or Al₂O₃ as support on Si wafers, then depositing transition metal such as Fe, Co, and Ni as catalysts. CNTs were grown on substrates by using horizontal apparatus shown in Figure 1-4a. Substrates were put at the middle of the furnace, heated to and annealed under a H₂ environment at around 700-850 °C, and then the carbon source gas such as C₂H₂, C₂H₄, and C₂H₅OH is introduced to nucleate and grow CNTs from the catalyst nanoparticles (Figure 1-4b). Prepare catalysts by sputtering (Figure 1-3a) is well established, but not as practical as solution method.

On-substrate growth of CNTs facilitates the understanding of the mechanism. The catalyst particles are fixed on substrates and thus their structure can be easily analyzed for different CVD times. The catalysts and CNTs can be easily separated and thus the catalyst after CVD can be easily analyzed. On the other hand, on-substrate growth of CNTs suffers from the limited productivity as small as a few of tens of g per square meter of substrates even for the millimeter-scale growth due to the 2D reaction space of the flat substrates with limited surface area, which is the major obstacle to put them in industrial applications. Therefore, utilization of 3D space instead of 2D space is highly required for the mass production of CNTs.

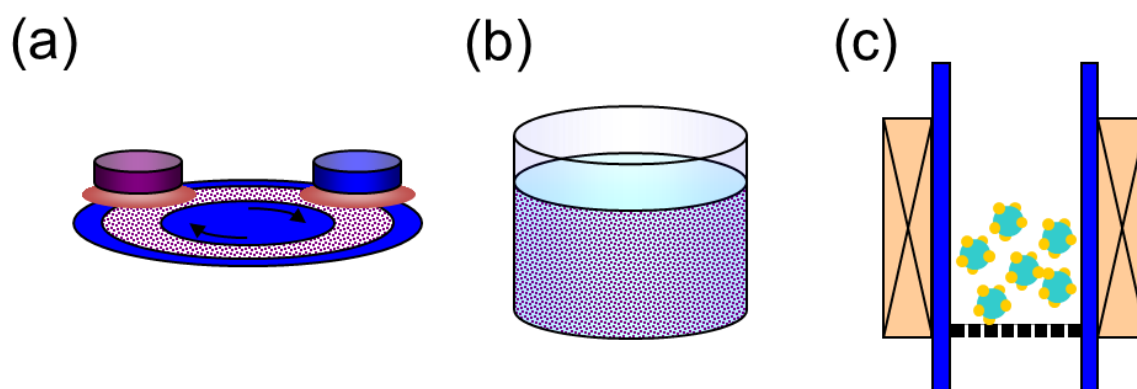


Figure 1-3. Schematics showing different methods for catalyst preparation: sputtering (a), solution (b) and CVD (c).

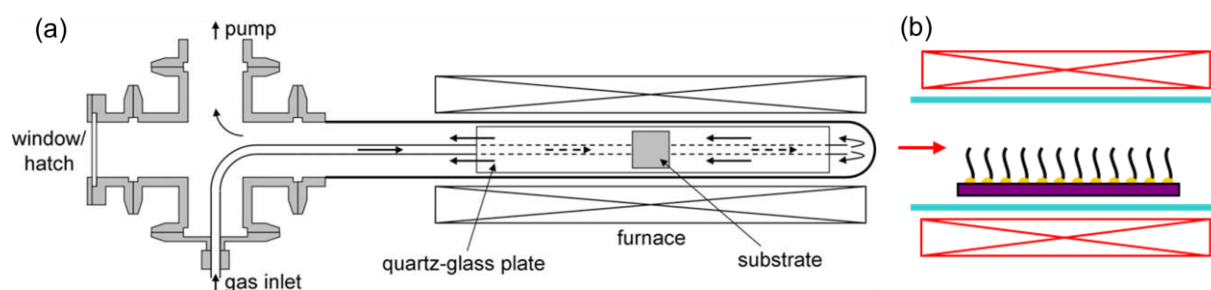


Figure 1-4. Schematics showing horizontal CVD apparatus for CNT growth on flat substrates (a) [111] and the corresponding VA-CNT structures on substrates with supported catalysts (b).

1.3.3 Fluidized bed synthesis by supported catalysts

Catalysts supported on powders realize catalyst particles at a high density and in 3D and thus widely used in industries (Figure 1-3c shows the schematic of catalyst preparation on powders by using CVD method). FBCVD is one of the most popular methods for the mass production of CNTs due to its advantages such as the good heat and mass transfer and the ability to handle powders continuously. As a result, a uniform bed temperature is achievable, which is critical to control the structure and quality of CNTs upon scale up. In addition, this kind of system provides a large contact area among the reactants and catalyst powder, which makes the chemical reactions and heat transfer more effective. Consequently, compared with floating catalyst CVD and on substrate CVD with supported catalysts, FBCVD with catalyst supported on powder is more efficient for synthesis of large quantities of CNTs.

To improve the productivity of CNTs, one method is to prolong the formation of CNTs during CVD, which is difficult because of the deactivation of catalysts, and another is to use supports having larger surface area than flat substrates. Spherical particles have larger surface area than flat substrates. Xiang et al. realized the synthesis of VACNTs on ceramic spheres by using cyclohexane as feedstock [55]. The growth of CNTs needed a delicate pump to quantitatively feed liquid state cyclohexane into the reactor, which decreases the efficiency. Zhang et al. improved the process and successfully obtained VACNT arrays on ceramic spheres by using the floating catalyst process with ethylene as the carbon source [56]. In both cases, although they increased the production of CNTs, the process was performed in horizontal apparatus and in monolayer, and thus CNTs were not mass produced. Catalyst stuck in 3D, such by FBCVD, is highly required.

Zhang et al. developed a lamellar catalyst by impregnation them in catalyst salt solution followed by calcination, and grew several-tens-micrometer-long MWCNTs among the layers of vermiculite at a purity of 84 wt% by FBCVD [57]. They recently reported the mass production of MWCNTs at a rate of 3.0 kg/h using a pilot plant FBCVD reactor with an inner diameter of 0.5 m [58]. These approaches realized better control of CNT diameters than the simultaneous feeding of catalyst and carbon sources [59, 60], however they needed additional apparatuses and times for catalyst predeposition and allowed catalyst contamination (16–25 wt.%). We previously realized the rapid conversion of C_2H_2 into CNTs with yield of around 70 wt% at short residence time of 0.3 s by FBCVD [1]. The CNTs were with 3 walls on average, 8 ± 2 nm in diameter, with 99 wt% carbon purity, which are closed to the structure as CNTs grown on flat substrates. Catalysts were supported on ceramic beads, as shown in Figure 1-5, which is the schematic for FBCVD apparatus for CNT growth on spherical Al_2O_3 beads (a) and the corresponding CNT synthesis on supported catalysts (b). Catalysts were prepared by CVD method (Figure 1-3c), which are of high efficiency and compatible for mass production of CNTs.

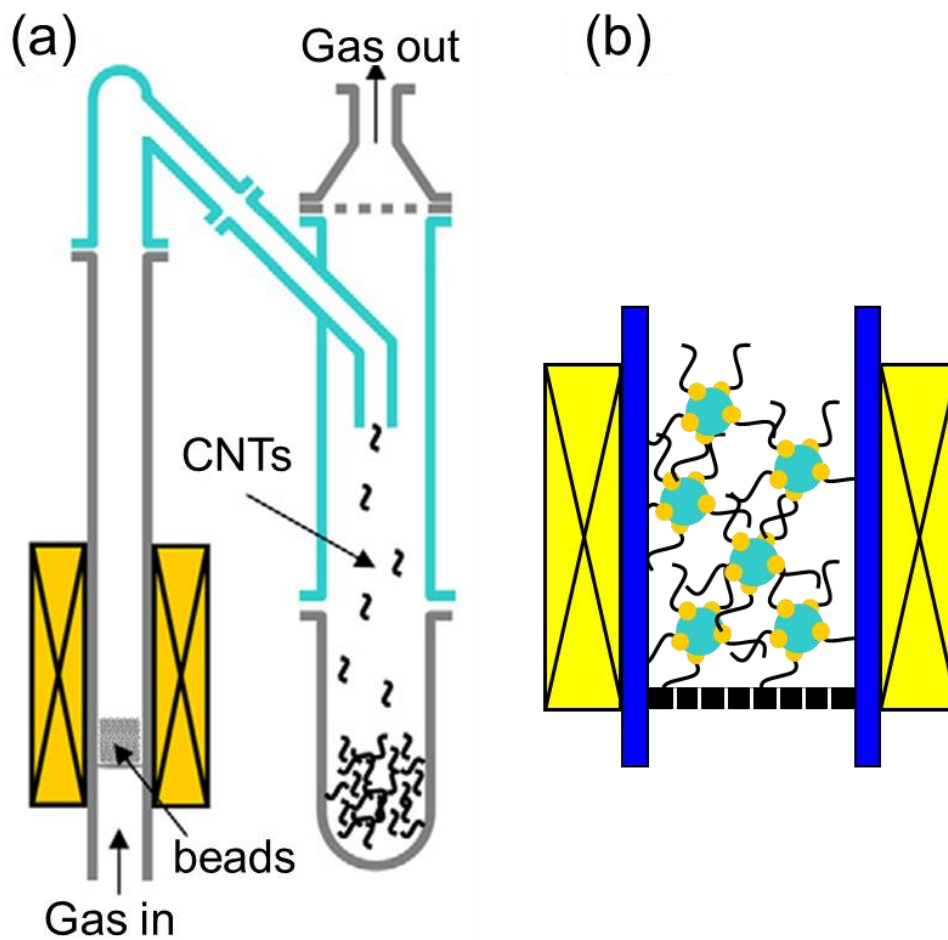


Figure 1-5, Schematics showing fluidized CVD apparatus for CNT growth on spherical Al₂O₃ beads (a) and the corresponding CNT synthesis on supported catalysts (b) [1].

1.4 Mechanism for CNT growth by supported catalysts

Transition metal catalysts such as Fe, Co, and Ni show high activity for CNT growth [61]. Hydrocarbons and other carbon precursors are readily decomposed on the surface of the transition metal, hereafter, surface/bulk diffusion of carbon atoms easily occurs on/in the transition metal catalyst. The growth mechanism for CNTs has been debatable since their discovery. According to the reaction conditions and post deposition product analyses,

different possible mechanisms have been proposed by several groups, which are often contradicting with each other. Nevertheless, widely-accepted most general mechanism can be outlined as follows. Hydrocarbon vapor first decomposes into carbon atoms and hydrogen species on “hot” metal nanoparticles. Then, hydrogen desorbs away and carbon will be dissolved into the metal. After reaching the carbon-solubility limit in the transition metals at a fixed temperature, dissolved carbon precipitates out and crystallizes and CNTs grow. Based on the statuses of catalyst particles staying on or leaving from substrates, the mechanism are separated to “root growth” and “tip growth” of CNTs, which are widely accepted [62, 63].

1.4.1 Root growth

When the catalyst–substrate interaction is strong, initial hydrocarbon decomposition and carbon diffusion take place. Hydrocarbon decomposes on the surface of the metal, carbon diffuses through the metal, and CNT precipitates out from the metal, but cannot push the metal particle up because of the strong force between metal and substrates. Therefore, the precipitates are compelled to emerge out not at the metal/substrate interface but at the free surface of the metal. As shown in Figure 1-6a, at the beginning hemispherical dome like carbon crystals so called fullerene caps will be formed, which then extends up in the form of seamless graphitic tube. Subsequent hydrocarbon deposition keeps on. The whole CVD process is going on with catalyst particles rooted on its base, which is well known as the “base-growth model” [64]. Figure 1-6b shows the real time monitoring for CNT nucleation and growth from iron carbide (Fe_3C) nanoparticles in CVD by in situ environmental transmission electron microscopy showing the root growth mechanism for CNTs [65]. In the “root growth” mechanism, catalysts stay on the substrate throughout the CVD process.

We previously observed a diameter increase for SWCNTs from the top to the bottom and also the size of catalyst particles increased after CVD for CNT growth [49, 51]. These phenomena originate from the catalyst coarsening through Ostwald ripening during CVD, which is one of the major obstacles for the further progress in CNT synthesis [67-74]. Ostwald ripening happens because the smaller particles are energetically more unstable than larger particles. In order to lower its overall energy, molecules on the surface of a small (energetically unfavorable) particle will tend to detach and diffuse over the substrate and then attach to the surface of larger particle. As a result, the number of smaller particles continues to shrink, while larger particles continue to grow. Figure 1-7 shows the schematic for Ostwald ripening and the diameter increase in growing CNTs. Typically, small catalyst particles will get smaller and finally disappear during CVD, which resulted in the CNT growth termination. On the other hand, big particles will get bigger and result in the diameter increasing for CNTs. SWCNTs sometimes grow long keeping single-wall structure with increasing diameter [49]. But SWCNTs sometimes change into MWCNTs, possibly due to the growth termination, re-nucleation and growth of MWCNTs from coarsened particles [45]. How to keep small catalyst particles active for CNT growth and stable against coarsening is a very important and difficult issue toward longer CNTs with smaller diameters.

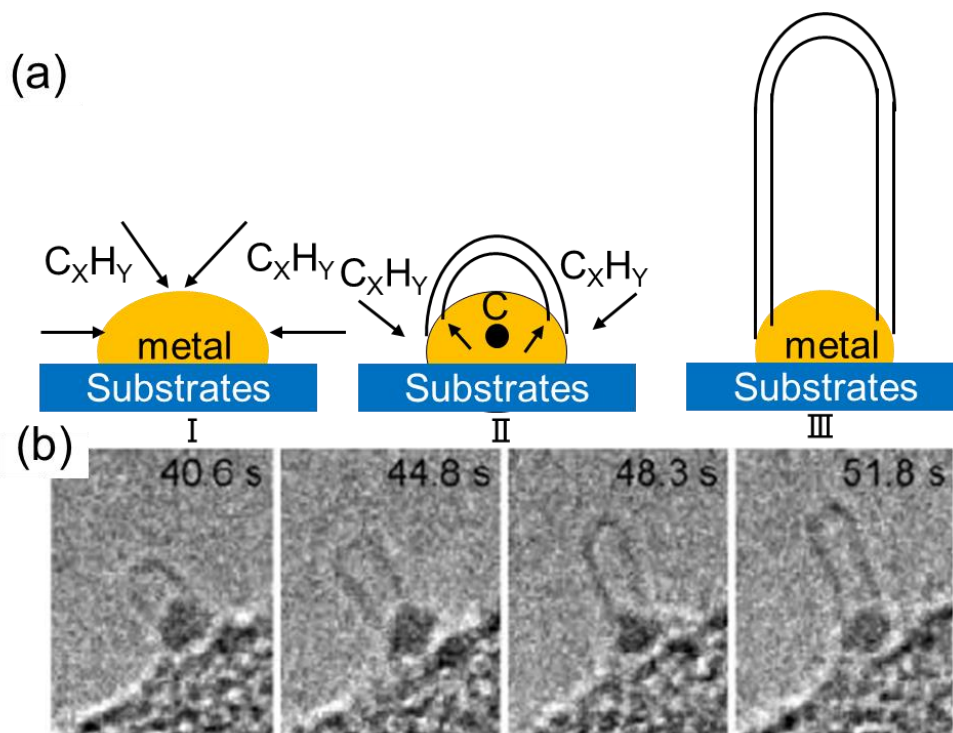


Figure 1-6. (a) Schematic showing the root growth model for CNTs. (b) Real time monitoring of nucleation and growth of a CNT from an iron carbide (Fe_3C) nanoparticle during CVD by in situ environmental TEM. The images clearly shows the root growth mechanism for CNTs (Reprinted with permission from { Ref. [65], Nano Lett. 8 (2008) 2082.}, Copyright 2008

American Chemicals Society).

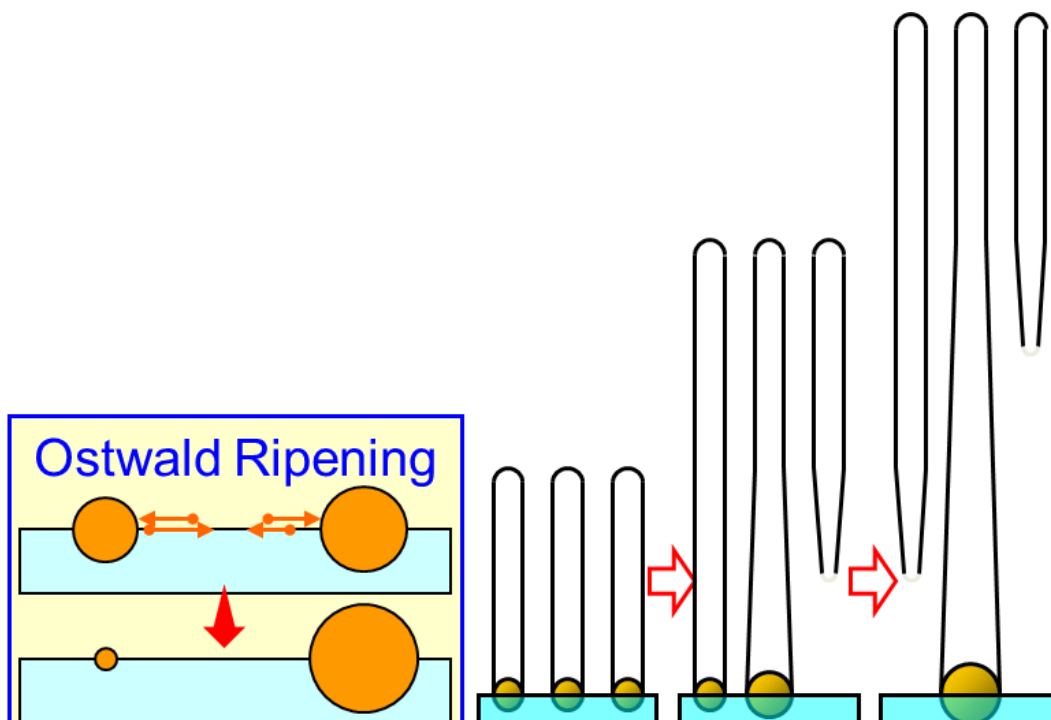


Figure 1-7. Schematics for the coarsening of catalyst particles through Ostwald ripening during CVD and resulting diameter change of SWCNTs.

1.4.2 Tip growth

In contrast to the “root-growth model”, if the catalyst – substrate interaction is weak, , CNT precipitating out from the catalyst particles push the particle off the substrate (Figure 1-8a (Steps I and II)). As long as the metal’s surface is open for hydrocarbon decomposition (concentration gradient exists in the metal allowing carbon diffusion), the CNT continues to grow longer and longer (Figure 1-8a (Step III)). This is widely known as “tip-growth model” [65, 75-79]. Figure 1-8b shows the real time monitoring of a CNT growing from a catalyst particle by in situ environmental TEM, representing the tip growth mechanism for CNTs [78]. For the tip-growth mechanism, since the catalysts were on the tip of the CNTs, there is no limitation for the growth of CNTs (no force inhibits CNTs to grow) [66]. With this advantage,

some researchers realized the ultra-long synthesis of CNTs, which was also known as the “kite mechanism” [80-82]. However, such CNTs grow at a quite low density, typically several CNTs from millimeter-size catalyst patterns.

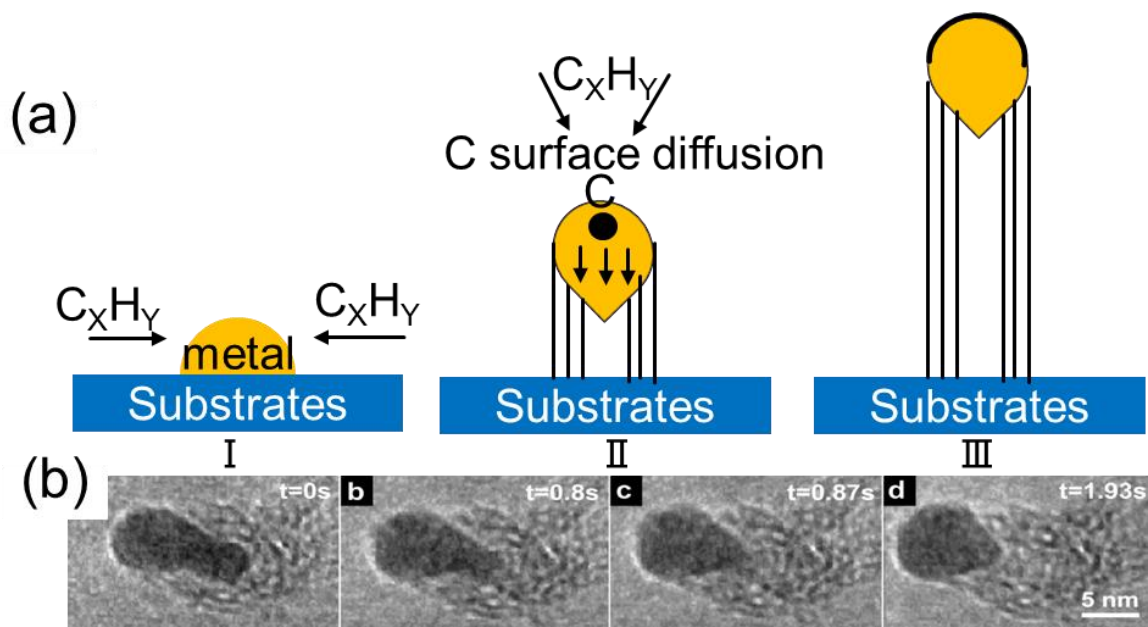


Figure 1-8. (a) Schematic showing the tip growth model for CNT synthesis. (b) Real time monitoring of a CNT growing from a catalyst particle by in situ environmental TEM. The images clearly show the tip growth mechanism for CNTs (Reprinted with permission from { Ref. [78], Nano Lett. 7 (2007) 602.}, Copyright 2007 American Chemical Society).

1.5 Characterization of CNTs

Due to their specific atomic structure, CNTs have interesting chemical and physical properties. Some of the important characterization methods of CNTs will be covered. The optical properties of CNTs will be measured by Raman spectroscopy. The structure and morphology of CNTs will be observed by TEM and scanning electron microscopy (SEM).

The carbon purity of CNTs will be determined by thermo-gravimetric analysis (TGA). The surface area of CNTs is most commonly evaluated by N₂ gas adsorption with the Brunauer–Emmett–Teller (BET) model.

1.5.1 Raman spectroscopy

Raman spectroscopy is an exceedingly powerful tool useful in the study of the vibrational properties and electronic structures of CNTs, especially for characterization of CNTs with respect to their diameters, defects and tube alignment, and assists us to judge the presence of SWCNTs relative to other carbon allotropes [83]. Different carbon materials such as SWCNTs, DWCNTs and MWCNTs can be analyzed by Raman spectroscopy. It has been strikingly successful at describing the structural properties of SWCNTs [84, 85]. However, quantitative determination of each type is not possible at present state of the art [86]. Unfortunately, compared with the output achieved for SWCNTs by Raman spectroscopy, because of the interpretation of the spectra from a MWCNT is often very complicated, it has not yet yielded the same level of output for MWCNTs [87]. Therefore, the interpretation of the experimental spectra is usually based on well-established results obtained for SWCNTs.

Figure 1-9 is a typical Raman spectrum of vertically aligned SWCNTs. It has the following typical features: (a) a low-frequency peak $< 200\text{ cm}^{-1}$, assigned to the symmetry radial breathing mode (RBM). This peak is absent in graphite and is the main signature of SWCNTs. The frequency of this mode depends only on the tube diameter [88]. (b) a group of peaks at around 1340 cm^{-1} was assigned to the disorder present in the graphitic materials, called the “D-band”. (c) a high-frequency bunch (between 1500 and 1600 cm^{-1}), which is the dominant peak in the Raman spectrum, corresponds to a resonant excitation of in-plane optical phonons, reflecting the graphitic nature of the nanotube, called “G-band” [89].

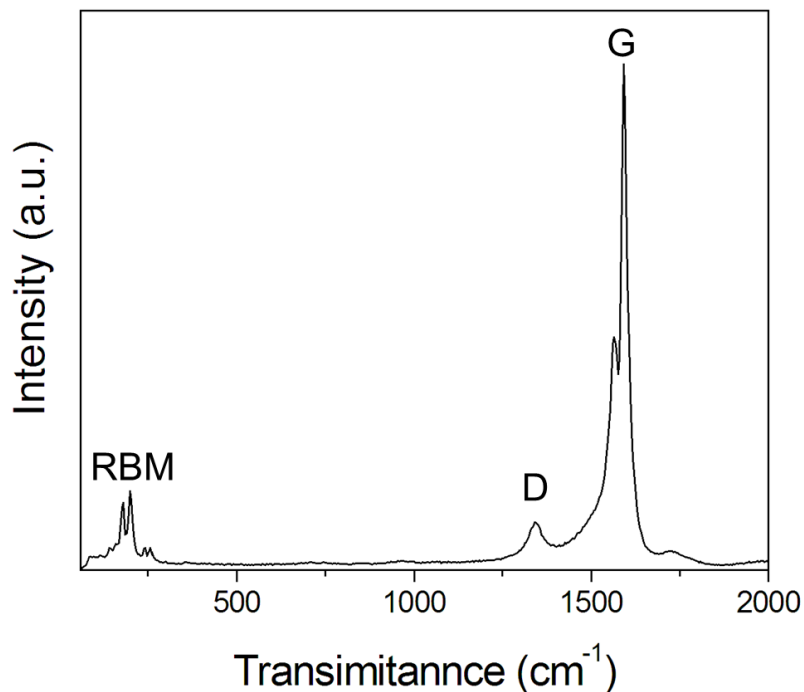


Figure 1-9, A typical Raman spectrum of vertically aligned SWCNTs (488 nm excitation laser).

1.5.2 Electron microscopy

Electron microscopy is an indispensable tool used in many areas of science, by using electrons to produce an image. By scanning an electron beam over a sample in a raster pattern and then detecting the scattered electrons, it can produce images. SEM is one of the microscopes designed for this purpose. A field emission (FE-) SEM, which uses a field emitter to obtain an intense electron beam, can further improve the resolution of images. In addition to the SEM, there is another kind of electron microscope – called TEM – which is capable of even higher magnification.

Figure 1-10 (a) is a typical image for vertical-aligned CNT forests obtained using an FE-SEM, which unambiguously reveals the morphologies, orientation and dimensions of CNT samples on flat substrates. Figure 1-10 (b) shows the TEM image of SWCNT bundles. The

single-layered tube walls as well as bundles of SWCNTs can be seen in the image. A good TEM is capable of atomic resolution, thus gives an extremely accurate picture of the crystal structure of a material. From atomic-resolution image or diffraction pattern of a SWCNT one can determine the chirality of it.

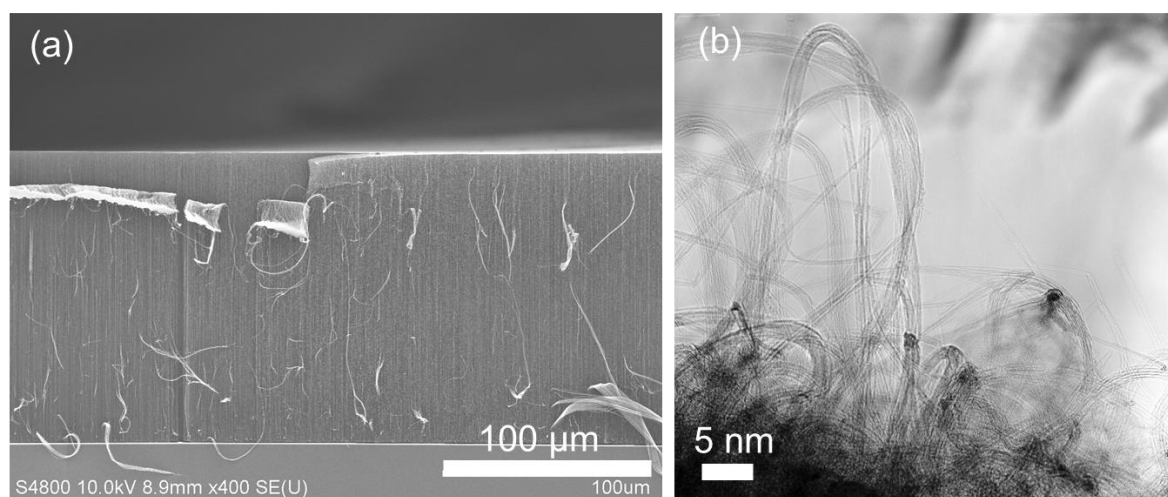


Figure 1-10. (a) A SEM image of a SWCNT array on a flat substrate surface. (b) A TEM image of SWCNT bundles at the top of a SWCNT array.

1.5.3 Thermogravimetry

TGA is a common analytical approach, which is used to determine the thermal stability of a material and its fraction of volatile components based on monitoring the weight change that occurs as a specimen is heated. The measurement is normally carried out in air or in an inert atmosphere, such as N_2 or Ar, and the weight is recorded as a function of increasing temperature. Besides weight changes, the temperature difference between the specimen and one or more reference pans (differential thermal analysis, DTA) or the heat flow into the specimen pan compared to that of the reference pan (differential scanning calorimetry, DSC) are recorded by some instruments. DSC can be used to monitor the energy released or

absorbed via chemical reactions and/or phase transition during the heating process. This measurement can be performed without sample preparation, which is a popular analytical method and many scientists use it for the analysis of the carbon purity for CNTs [90-92].

As for CNTs, the weight change in an air or N_2 atmosphere is typically a superposition of the weight loss due to oxidation of carbon into gaseous carbon dioxide and/or carbon monoxide and the weight gain due to oxidation of residual metal catalyst into solid oxides. Figure 1-11 is the typical TGA curves for MWCNTs. The derivative of the weight loss curve can be observed from the oxidation peaks, which can give information about the quality of the CNTs. The carbon purity of CNTs can be indicated from the width of the oxidation peak, with a narrow peak indicating a cleaner material. The amorphous carbons always decompose at the lower temperatures due to a higher curvature strain [93, 94]. Kim et al. compared the effect of the diameters of MWCNTs on oxidation temperature, it showed that narrow MWCNTs were found to decompose at lower temperatures than larger-diameter MWCNTs [95, 96].

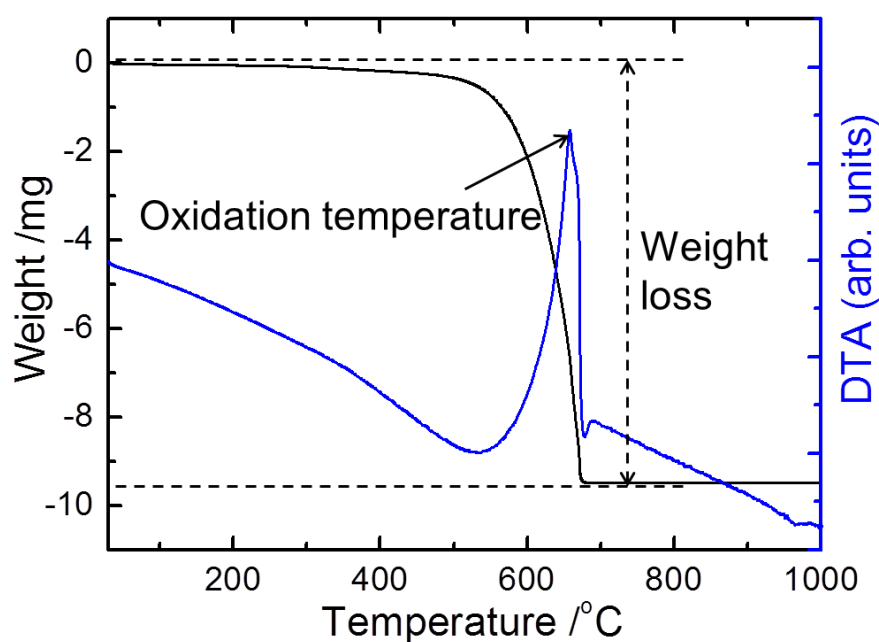


Figure 1-11. Typical TGA curves of pristine MWCNTs.

1.5.4 Brunauer–Emmett–Teller (BET) surface area measurement

One single CNT has a very large specific surface area (named as SSA hereafter) owing to its nanometric diameter. In materials science, the SSA of macroscopic samples of powders or porous materials is most commonly based on the measurement of N₂ adsorption (at 77 K). The Brunauer–Emmett–Teller (BET) isotherm developed in 1938 is a rule for the physical adsorption of gas molecules on a solid surface and serves as the basis for an important analysis technique for the measurement of the SSA of a material [97-99]. BET extends the Langmuir adsorption theory to describe multilayer adsorption of N₂ on the surface of a material, which equates the rate of condensation of one monolayer of adsorbate to the rate of desorption of the previous monolayer coverage on the surface. The observation of the so-called adsorption and desorption isotherms was used to determine the amount of gas molecules adsorbed to a surface. The theoretical external surface area of CNTs as a function of their number of walls and diameters ranges from 50 to 1315 m²/g [100]. For the as-produced MWCNTs, the SSA of them generally ranges from 10 to 500 m²/g.

1.6 Application of CNTs to the electric storage devices

Due to the ever-increasing demand of electric supply, there are growing challenges among a broad range of renewable energy sources. Development of high-energy storage devices is a very important research target these days. Because of their outstanding properties, such as large specific surface area, high chemical/ mechanical stability, and light weight, in addition to their good electrochemical performance, extraordinary tensile strength and flexibility, they are promising candidate for the emerging flexible/stretchable electronics

[101-104]. CNTs are promising as one-dimensional hosts for the intercalation of Li in lithium ion batteries (LIBs). CNTs as a conductive additive can be incorporated at a lower weight loading than conventional carbons, such as carbon black and graphite, which shows a more effective strategy to establish an electrical percolation network. Furthermore, with the capability to be assembled into free-standing electrodes (absent of any binder or current collector), they are popular to be used as an active lithium ion storage material [105-107]. Excellent performance in supercapacitor electrodes was also achieved by using conductive and flexible CNTs. Pushparaj et al. demonstrated the design, fabrication, and packaging of flexible CNT–cellulose–RTIL nanocomposite sheets, which can be used in configuring energy-storage devices such as supercapacitors [108]. Quintero et al. used FWCNTs 3D current collectors for lightweight, high performance and low cost supercapacitor electrodes [109]. The realization of VACNT forest synthesis provided, among the properties and applications of CNTs, some new possibility that has not been achieved or ever expected. One example is drawing continuous yarns from a VA-CNT forest, and their application to energy storage devices has been demonstrated [110].

In order to fully realize the application of CNTs for energy storage applications, understanding the mechanism for CNT growth and synthesizing high quality CNTs at large scale are important. Therefore, my PhD study was conducted to grow SWCNTs on flat substrates to understand their basic growth mechanism firstly. Then, I used FBCVD method to synthesize FWCNTs with increased scale, increased purity, and controlled diameters. The details are introduced in the chapters hereafter.

References

- [1] D.Y. Kim, H. Sugime, K. Hasegawa, T. Osawa, S. Noda, Carbon 49 (2011) 1972.
- [2] A. K. E. Shipway, I. Willner, ChemPhysChem 1 (2001) 18.
- [3] M. Kaempgen, C. K. Chan, J. Ma, Y. Cui, G. Gruner, Nano Lett. 9 (2009) 1872.
- [4] X. Yu, R. Rajamani, K. A. Stelson, T. J. Cui, Nanosci. Nanotechnol. 6 (2006) 1939.
- [5] B. H. Chen, H. C. Lin, T. Y. Huang, J. H. Wei, H. H. Wang, M. J. Tsai, T. S. Chao, Appl. Phys. Lett. 88 (2006) 093502.
- [6] R. Jackson, B. Domercq, R. Jain, B. Kippelen, S. Graham, Adv. Funct. Mater. 18 (2008) 2548.
- [7] K. S. Novoselov, Z. Jiang, Y. Zhang, S. V. Morozov, H. L. Stormer, U. Zeitler, J. C. Maan, G. S. Boebinger, P. Kim, A. K. Geim, Science 315 (2007) 1379.
- [8] C. Berger, Z. M. Song, X. B. Li, X. S. Wu, N. Brown, C. Naud, D. Mayou, T. B. Li, J. Hass, A. N. Marchenkov, E. H. Conrad, P. N. First, W. A. de Heer, Science 312 (2006) 1191.
- [9] S. Iijima, Nature 354 (1991) 56.
- [10] N. Saifuddin, A. Z. Raziah, A. R. Junizah, J. Chem. (2013) 676815, 1
- [11] M. S. Dresselhaus, G. Dresselhaus, A. Jorio, Annu. Rev. Mater. Res. 34 (2004) 247.
- [12] R. Saito, M. Fujita, G. Dresselhaus, M. S. Dresselhaus, Phys. Rev. B 46 (1992) 1804.
- [13] T. G., S. Durkop, E. Cobas, M. S. Fuhrer, Nano Lett. 4 (2004) 35.
- [14] J. W. W. Wintmire, C. T. White, Phys. Rev. Lett. 81 (1998) 2506.

-
- [15] C. L. Kane, E. J. Mele, Phys. Rev. Lett. 78 (1997) 1932.
- [16] Y. A. Kim, H. Muramatsu, T. Hayashi, M. Endo, M. Terrones, M. S. Dresselhaus, Chem. Vap. Dep. 12, (2006) 327.
- [17] E. Flahaut, C. Laurent, A. Peigney, Carbon 43 (2005) 375.
- [18] <http://www.photon.t.u-tokyo.ac.jp/index-j.html>.
- [19] T. W. Ebbesen, P. M. Ajayan, Nature 358 (1992) 220.
- [20] C. Journet, W. K. Maser, P. Bernier, A. Loiseau, M. Lamy de la Chapelle, S. Lefrant, P. Deniard, R. Lee, J. E. Fischer, Nature 388 (1997) 756.
- [21] A. Thess, R. Lee, P. Nikolaev, H. Dai, P. Petit, J. Robert, C. Xu, Y. H. Lee, S. G. Kim, A. G. Rinzler, D. T. Colbert, G. E. Scuseria, D. Tomanek, J. E. Fischer, R. E. Smalley, Science 273 (1996) 483.
- [22] J. Kong, A. M. Cassell, H. Dai, Chem. Phys. Lett., 292 (1998) 567.
- [23] S. Fan, M. G. Chapline, N. R. Franklin, T. W. Tombler, A. M. Cassell, H. Dai, Science 283 (1999) 512.
- [24] C. Bower, O. Zhou, W. Zhu, D. J. Werder, S. Jin, Appl. Phys. Lett. 77 (2000) 2767.
- [25] M. Su, B. Zheng, J. Liu, Chem. Phys. Lett. 322 (2000) 321.
- [26] H. M. Cheng, F. Li, G. Su, H. Y. Pan, L. L. He, X. Sun, M. S. Dresselhaus, Appl. Phys. Lett. 72 (1998) 3282.
- [27] H. M. Cheng, F. Li, X. Sun, S. D. M. Brown, M. A. Pimenta, A. Marucci, G. Dresselhaus, M. S. Dresselhaus, Chem. Phys. Lett. 289 (1998) 602.

-
- [28] P. Nikolaev, M. J. Bronikowski, R. K. Bradley, F. Rohmund, D. T. Colbert, K. A. Smith, R. E. Smalley, *Chem. Phys. Lett.* 313 (1999) 91.
- [29] A. G. Nasibulin, A. Moisala, D. P. Brown, H. Jiang, E. I. Kauppinen, *Chem. Phys. Lett.* 402 (2005) 227.
- [30] A. G. Nasibulin, P. Queipo, S. D. Shandakov, D. P. Brown, H. Jiang, P. V. Pikhitsa, O. V. Tolochko, E. I. Kauppinen, *J. Nanosci. Nanotechnol.* 6 (2006) 1.
- [31] A. Moisala, A. G. Nasibulina, D. P. Brown, H. Jiang, L. Khriachtchev, E. I. Kauppinen, *Chem. Eng. Sci.* 61 (2006) 4393.
- [32] C. H. Kiang, M. S. Dresselhaus, R. Beyers, D. S. Bethune, *Chem. Phys. Lett.* 259 (1996) 41.
- [33] Z. Zhou, L. Ci, X. Chen, D. Tang, X. Yan, D. Liu, Y. Liang, H. Yuan, W. Zhou, G. Wang, S. Xie, *Carbon* 41 (2003) 337.
- [34] W. Ren, F. Li, S. Bai, H. M. Cheng, *J. Nanosci. Nanotechnol.* 6 (2006) 1339.
- [35] D. S. Bethune, *Phys. B* 323 (2002) 90.
- [36] J. Goering, U. Burghaus, *Chem. Phys. Lett.* 447 (2007) 121.
- [37] R. M. Sundaram, K. K. K. Koziol, A. H. Windle, *Adv. Mater.* 23 (2011) 5064.
- [38] M. Endo, *Chem. Tech.* 18 (1988) 568.
- [39] W. Z. Li, S. S. Xie, L. X. Qian, B. H. Chang, B. S. Zou, W. Y. Zhou, R. A. Zhao, G. Wang, *Science* 274 (1996) 1701.
- [40] Y. Murakami, S. Chiashi, Y. Miyauchi, M. Hu, M. Ogura, T. Okubo, S. Maruyama, *Chem. Phys. Lett.* 385 (2004) 298.

-
- [41] R. Xiang, PhD thesis in the University of Tokyo, (2009)
- [42] K. Hata, D. N. Futaba, K. Mizuno, T. Namai, M. Yumura, S. Iijima, *Science*, 306 (2004) 1362.
- [43] R. E. Smalley, K. A. Smith, D. T. Colbert, P. Nikolaev, M. J. Bronikowski, R. K. Bradley, F. Rohmund, R. Smalley, K. Smith, D. Colbert, (Univ Rice) WO200026138A, (2000).
- [44] P. Nikolaev, M. J. Bronikowski, R. K. Bradley, F. Rohmund, D. T. Colbert, K. A. Smith, R. E. Smalley, *Chem. Phys. Lett.* 313 (1999) 91.
- [45] H. Sugime, S. Noda, *Carbon* 48 (2010) 2203.
- [46] H. Sugime, S. Noda, *Carbon* 50 (2012) 2953.
- [47] K. Hasegawa, S. Noda, *ACS Nano* 5 (2011) 975.
- [48] S. Noda, K. Hasegawa, H. Sugime, K. Kakehi, Z. Zhang, S. Maruyama, Y. Yamaguchi, *Jpn. J. App. Phys.* 46 (2007) L399.
- [49] K. Hasegawa, S. Noda, *Appl. Phys. Express* 3 (2010) 045103.
- [50] K. Hasegawa, S. Noda, *Jpn. J. Appl. Phys.* 49 (2010) 085104.
- [51] K. Hasegawa, S. Noda, *Carbon* 49 (2011) 4497.
- [52] R. Itoh, S. Noda, T. Osawa, S. Maruyama, Y. Yamaguchi, 2008 MRS Spring Meeting, P4.26, San Francisco, CA, USA, March 2008.
- [53] S. Noda, H. Sugime, T. Osawa, Y. Tsuji, S. Chiashi, Y. Murakami, S. Maruyama, *Carbon* 44 (2006) 1414.

-
- [54] S. Noda, H. Sugime, K. Hasegawa, K. Kakehi, Y. Shiratori, *Jpn. J. Appl. Phys.* 49 (2010) 02BA02.
- [55] R. Xiang, G. Luo, W. Qian, Y. Wang, F. Wei, Q. Li, *Chem. Vap. Dep.* 13 (2007) 533.
- [56] Q. Zhang, J. Q. Huang, M. Q. Zhao, W. Z. Qian, Y. Wang, F. Wei, *Carbon* 46 (2008) 1152.
- [57] R. Xiang, G. Luo, Z. Yang, Q. Zhang, W. Qian, F. Wei, *Mater. Lett.* 63 (2009) 84.
- [58] Q. Zhang, M. Q. Zhao, J. Q. Huang, J. Q. Nie, F. Wei, *Carbon* 48 (2010) 1196.
- [59] Q. Zhang, J. Huang, M. Zhao, W. Qian, Y. Wang, F. Wei, *Carbon* 46 (2008) 1152.
- [60] Q. Zhang, M. Zhao, J. Huang, Y. Liu, Y. Wang, W. Qian, F. Wei, *Carbon* 47 (2009) 2600.
- [61] Q. Zhang, J. Huang, M. Zhao, W. Qian, F. Wei, *ChemSusChem* 4 (2011) 864.
- [62] M. Kumar, Y. Ando, *J. Nanosci. Nanotechnol.* 10 (2010) 3739.
- [63] J. P. Tessonnier, D. S. Su, *ChemSusChem* 4 (2011) 824.
- [64] R. T. K. Baker, R. J. Waite, *J. Catalysis*, 37 (1975) 101.
- [65] H. Yoshida, S. Takeda, T. Uchiyama, H. Kohno, Y. Homma, *Nano Lett.* 8 (2008) 2082.
- [66] S. Huang, M. Woodson, R. Smalley, J. Liu, *Nano Lett.* 4 (2004) 1025.
- [67] S. Sakurai, H. Nishino, D. N. Futaba, S. Yasuda, T. Yamada, A. Maigne, Y. Matsuo, E. Nakamura, M. Yumura, K. Hata, *J. Am. Chem. Soc.* 134 (2012) 2148.
- [68] P. B. Amama, C. L. Pint, L. McJilton, S. M. Kim, E. A. Stach, P. T. Murray, R. H. Hauge, B. Maruyama, *Nano Lett.* 9 (2009) 44.

-
- [69] S. M. Kim, C. L. Pint, P. B. Amama, D. N. Zakharov, R. H. Hauge, B. Maruyama, E. A. Stach, *J. Phys. Chem. Lett.* 1 (2010) 918.
- [70] I. M. Lifshitz, V. V. Slezhov, *J. Phys. Chem. Solids* 19 (1961) 35.
- [71] C. Z. Wagner, *Electrochem.* 65 (1961) 581.
- [72] B. K. Chakraverty, *J. Phys. Chem. Solids* 28 (1967) 2401.
- [73] A. Baldan, *J. Mater. Sci.* 37 (2002) 2172.
- [74] W. Ostwald. 1896. *Lehrbuch der Allgemeinen Chemie*, vol. 2, part 1. Leipzig, Germany.
- [75] H. Dai, A. G. Rinzler, P. Nikolaev, A. Thess, D. T. Colbert, R. E. Smalley, *Chem. Phys. Lett.* 260 (1996) 471.
- [76] D. Takagi, Y. Kobayashi, H. Hibino, S. Suzuki, Y. Homma, *Nano Lett.* 8 (2008) 832.
- [77] Y. Homma, *Catal.* 4 (2014) 38.
- [78] S. Hofmann, R. Sharma, C. Ducati, G. Du, C. Mattevi, C. Cepek, M. Cantoro, S. Pisana, A. Parvez, F. Cervantes-Sodi, A. C. Ferrari, R. Dunin-Borkowski, S. Lizzit, L. Petaccia, A. Goldoni, J. Robertson, *Nano Lett.* 7 (2007) 602.
- [79] J. C. Charlier, H. Amara, P. Lambin, *ASC Nano* 1 (2007) 202.
- [80] L. X. Zheng, M. J. O'Connell, S. K. Doorn, X. Z. Liao, Y. H. Zhao, E. A. Akhadow, M. A. Hoffbauer, B. J. Roop, Q. X. Jia, R. C. Dye, D. E. Peterson, S. M. Huang, J. Liu, Y. T. Zhu, *Nat. Mater.* 3 (2004) 673.
- [81] S. Huang, M. Woodson, R. Smalley, J. Liu, *Nano Lett.* 4 (2004) 1025.
- [82] R. Zhang, Q. Wen, W. Qian, D. S. Su, Q. Zhang, F. Wei, *Adv. Mater.* 23 (2011) 3387.

-
- [83] M. S. Dresselhaus, G. Dresselhaus, A. Jorio, A. G. Souza Filho, M. A. Pimenta, D. R. Saito, *Acc. Chem. Res.* 35 (2002) 1070.
- [84] L. Kavan, P. Rapt, L. Dunsch, M. J. Bronikowski, P. Willis, R. E. Smalley, *J. Phys. Chem. B* 105 (2001) 10764.
- [85] L. Alvarez, A. Righi, T. Guillard, S. Rols, E. Anglaret, D. Laplaze, J. L. Sauvajol, *Chem. Phys. Lett.*, 316 (2000), 186.
- [86] W. Qian, T. Liu, F. Wei, H. Yuan, *Carbon* 41 (2003) 1851.
- [87] J. H. Lehman, M. Terrones, E. Mansfield, K. E. Hurst, V. Meunier, *Carbon* 49 (2011) 2581.
- [88] A. M. Rao, E. Richter, S. Bandow, B. Chase, P. C. Eklund, K. A. Williams, S. Fang, K. R. Subbaswamy, M. Menon, A. Thess, R. E. Smalley, G. Dresselhaus, M. S. Dresselhaus, *Science* 275 (1997) 187.
- [89] A. A. Mamedov, N. A. Kotov, M. Prato, D. M. Guldi, J. P. Wicksted, A. Hirsch, *Nat. Mater.* 1 (2002) 190.
- [90] Y. Hsieh, Y. C. Chou, C. Lin, T. F. Hsieh, C. M. Shu, *Aerosol Air Qual. Res.* 10 (2010) 212.
- [91] L. S. K. Pang, J. D. Saxby, S. P. Chatfield, *J. Phys. Chem.* 97 (1993) 6941.
- [92] M. Zhang, M. Yudasaka, A. Koshio, S. Iijima, *Chem. Phys. Lett.* 364 (2002) 420.
- [93] A. Lima, A. Musumeci, H. W. Liu, E. Wacławik, G. Silva, *J. Therm. Anal. Calorim.* 97 (2009) 257.
- [94] O. M. Dunens, K. J. MacKenzie, A. T. Harris, *Environ. Sci. Technol.* 43 (2009) 7889.

-
- [95] D.Y. Kima, C. M. Yanga, Y. S. Parkb, K. K. Kima, S. Y. Jeonga, J. H. Hanb, Y. H. Lee, Chem. Phys. Lett. 413 (2005) 135.
- [96] D. Y. Kim, Y. S. Yun, S. M. Kwona, H. J. Jin, Mol. Cryst. Liq. Cryst. 510 (2009) 79.
- [97] A. S. Brunauer, P. H. Emmett, E. Teller, J. Am. Chem. Soc. 60 (1938) 309.
- [98] D. D. Do, Adsorption analysis: equilibria and kinetics. London: Imperial College Press; 1998.
- [99] F. Rouquerol, J. Rouquerol, K. Sing, Adsorption by powders and porous solids, principles, methodology and applications. London: Academic Press; 1999.
- [100] A. Peigney, C. Laurent, E. Flahaut, R. R. Bacsa, A. Rousset, Carbon 39 (2001) 507.
- [101] R. H. Baughman, A. A. Zakhidov, W. A. D. Heer, Science 297 (2002) 787.
- [102] M. F. L. D. Volder, S. H. Tawfick, R. H. Baughman, A. J. Hart, Science 339 (2013) 535.
- [103] D. Sun, M. Y. Timmermans, Y. Tian, A. G. Nasibulin, E. I. Kauppinen, S. Kishimoto, T. Mizutani, Y. Ohno, Nature Nanotechnol. 6 (2011) 156.
- [104] Z. Xiong, Y. S. Yun, H. J. Jin, Mater. 6 (2013) 1138.
- [105] B. J. Landi, M. J. Ganter, C. D. Cress, R. A. DiLeoa, R. P. Raffaellea, Energy Environ. Sci. 2 (2009) 638.
- [106] S.W. Lee, B. M. Gallant, Y. Lee, N. Yoshida, D.Y. Kim, Y. Yamada, S. Noda, A. Yamada, Y. Shao-Horn, Energy Environ. Sci. 5 (2012), 5437.
- [107] Y. Chen, X. Li, K. Park, J. Song, J. Hong, L. Zhou, Y. W. Mai, H. Huang, J. B. Goodenough, J. Am. Chem. Soc. 135 (2013), 16280.

-
- [108] V. L. Pushparaj, M. M. Shaijumon, A. Kumar, S. Murugesan, L. Ci, R. Vajtai, R. J. Linhardt, O. Nalamasu, P. M. Ajayan, PANS 104 (2007) 13574.
- [109] R. Quintero, D. Y. Kim, K. Hasegawa, Y. Yamada, A. Yamada, and S. Noda, RSC Adv. 4 (2014) 8230.
- [110] K. Jiang, J. Wang, Q. Li, L. Liu, C. Liu, S. Fan, Adv. Mater. 23 (2011) 1154.
- [111] H. Sugime, S. Noda, S. Maruyama, Y. Yamaguchi, Carbon 47 (2009) 234.

Chapter 2 - Methane-assisted CVD yielding millimeter-tall single-wall CNTs (SWCNTs) of small diameter

(Part of this chapter has been published in: Zhongming Chen, et al., ACS Nano 7 (2013) 8230.)

2.1 Introduction

Growing longer CNTs with smaller diameters is an ever-lasting challenge. In 1996, Li *et al.* reported the synthesis of VA-CNT arrays *via* CVD using Fe catalysts supported on porous SiO₂ [1]. These were MWCNTs with a diameter of ~30 nm and their height reached 50 µm in 2 h. Later, they improved the height to 2 mm by continuing CVD for as long as 48 h [2]. For SWCNTs, however, several more years were required for such growth to be achieved. Murakami *et al.* first realized the synthesis of VA-SWCNTs using CVD with C₂H₅OH as a feedstock, but the height was a few µm after 60 min of growth [3]. Hata *et al.* reported the "super growth" of VA-SWCNTs *via* water-assisted CVD; in this case, the height reached 2.5 mm in 10 min [4]. These works have driven many researchers to investigate O-containing precursors such as CO [5] in addition to C₂H₅OH [3,6-8], and O-containing additives such as O₂ [9], CO₂ [10], and many other species [11] in addition to H₂O [12-14]. Such species can enhance the lifetime of the catalyst by removing the carbon byproducts that cover the catalyst nanoparticles [12]. Because of such efforts, it is now possible to grow millimeter-tall VA-SWCNTs; however, such SWCNTs tend to have large diameters, of ~3 nm or larger [15-17]. Catalyst nanoparticles gradually become coarsened during CVD through Ostwald ripening [13], resulting in the abrupt termination of the growth and gradual increase in diameter of the growing SWCNTs [14,17-19]. The question of how to keep small catalyst nanoparticles stable

and active for SWCNT growth is a very difficult and important issue. Increasing the length while retaining the small diameter of SWCNTs is highly demanded in applications such as transparent conducting films [20] and spun-fibers [21] where the contacts between SWCNTs limit their electrical and mechanical properties.

To realize the full-scale practical applications of CNTs, it is necessary to achieve low-cost and large-scale production methods. Previously, we coupled the rapid growth of VA-CNTs with the fluidized-bed CVD method to realize the semi-continuous and batch production of submillimeter-long few-wall CNTs [22] and SWCNTs [23], respectively. The bed of catalyst-supported ceramic particles enabled the rapid conversion of C_2H_2 into CNTs with a carbon yield of ~ 70 at%, in residence times as short as 0.2-0.3 s. A large amount of H_2 —which is a common feed gas in many CVD processes for CNT production—is needed for this process. Hence, there is a practical motivation for replacing the expensive high-purity H_2 used in laboratory processes with the low-purity H_2 that is available at a low cost and/or a byproduct in chemical factories. In the naphtha cracking process, H_2 gas is produced as a byproduct in addition to various hydrocarbons (CH_4 , C_2H_4 , C_2H_6 , C_3H_6 , C_3H_8 , *etc.*). H_2 is separated by cryogenic distillation from this mixture, but some CH_4 remains in the separated H_2 . In this work, we examined the use of 96 vol% pure H_2 containing 4 vol% CH_4 for the rapid growth of millimeter-tall SWCNTs, and compared the results with those obtained using 99.999 vol%-pure H_2 . We examined whether the impurity (CH_4) disturbs the SWCNT growth; unexpectedly, we found that CH_4 has significant effects in suppressing the coarsening of the catalyst particles and growing taller VA-SWCNTs with smaller diameters. During the catalyst annealing, carbon deposited at a small amount from CH_4 on the Fe particles, which kept them small and dense. During CVD, CH_4 prevented the Fe particles from coarsening, resulting in an enhanced growth lifetime and suppressed diameter increase of growing

SWCNTs. These effects were observed only for CH₄, and not for C₂H₄ or C₂H₂. CH₄-assisted CVD is an efficient and practical method that uses H₂ containing CH₄ that is available as a byproduct in chemical factories.

2.2 Methods

The SWCNT growth process has been described in detail elsewhere [14,16,19]. Briefly, the catalysts were prepared on silicon wafers with a thermal oxide layer. First, the substrate surfaces were pretreated by dipping them into a mixed solution of H₂SO₄ (98 wt%) and H₂O₂ (30 wt%) (with a volume ratio of 3:1) for 5 min, followed by washing with de-ionized water. A 15 nm-thick Al layer was then sputter-deposited on the substrate, and partially oxidized *via* exposure to air. Finally, Fe catalysts were sputter-deposited on the Al layer, either with a uniform thickness of 0.5, 0.6, 0.7, or 1.0 nm, or with a gradient thickness profile of 0.1-2 nm; this was achieved using our previously described CMD method, in which the deposition flux distribution was formed by a physical filter during the sputter deposition [24,25]. The substrate with the catalysts was placed in a tubular CVD reactor (34 mm inner diameter and 300 mm heating zone length) and annealed during heating to and holding for 5 min at 800°C, under a gas flow of 26 vol% H₂/ 50 ppmv H₂O/ Ar, or 25 vol% H₂/ 1 vol% CH₄/ 50 ppmv H₂O/ Ar, at ambient pressure. During this heat treatment, the Fe formed nanoparticles of a certain diameter and number density, depending on the initial Fe thickness. CVD was then carried out by adding C₂H₂ to the gas. The standard CVD conditions were either 0.3 vol% C₂H₂/ 26 vol% H₂ / 50 ppmv H₂O/ Ar (without CH₄), or 0.3 vol% C₂H₂/25 vol% H₂/ 1 vol% CH₄/ 50 ppmv H₂O/ Ar (with CH₄), both fed at a flow rate of 500 sccm, at ambient pressure. The samples were monitored during CVD using a digital camera to obtain side-view images every 10 s, through a window on one side of the reactor tube. The spacial resolution was 0.03

mm per pixel. The catalyst particles were analyzed after annealing using AFM (Shimadzu SPM-9600), and XPS (JEOL JPS-9010TR) with a monochromatized Mg K α X-ray source. After CVD, the resulting CNTs were analyzed using SEM (Hitachi S-4800), Raman scattering spectroscopy (Horiba HR800), and TEM (JEOL 2000EX). The TEM samples were prepared by picking up a portion of the VA-SWCNTs and laying it on a TEM grid using tweezers [17]. The composition of the effluent gas from the C₂H₂-CVD reactor was measured by gas chromatography (GC, Shimadzu, GC-2014) equipped with a flame ionization detector (FID).

2.3 Overview of CH₄-assisted CVD yielding taller vertical aligned (VA)-SWCNTs of higher quality under a wider range of catalyst conditions

Using the CMD method [16,24,25], we could easily optimize the catalyst conditions for the SWCNT growth. Fe/AlO_x catalysts with a range of nominal Fe thicknesses (t_{Fe}) were prepared by sequentially sputter-depositing Al and Fe on silicon wafers with a thermal oxide layer (Figure 2-1a,b), and by annealing these samples in a 26 vol% H₂/ Ar mixture (named here as “without CH₄”), or a 25 vol% H₂/ 1.0 vol% CH₄/ Ar mixture (named here as “with CH₄”), both with 50 ppmv H₂O, at ambient pressure and 800 °C for 5 min in a tubular CVD reactor. CVD was then carried out by switching the gas mixture to 0.3 vol % C₂H₂/ 26 vol% H₂/ Ar, or 0.3 vol % C₂H₂/ 25 vol% H₂/ 1.0 vol% CH₄/ Ar, both with 50 ppmv H₂O, at ambient pressure.

Figure 2-1c,d shows digital images of the CNTs grown on the combinatorial catalyst library using H₂/ without and with CH₄, respectively. The CNTs were vertically aligned (Figure 2-2), and their height was largely dependent on t_{Fe} , as reported previously [14]. The

VA-CNTs were 0.7 mm tall at $t_{\text{Fe}} \approx 0.5$ nm, became shorter with $t_{\text{Fe}} < 0.5$ nm, and the CNTs hardly grew with $t_{\text{Fe}} < 0.3$ nm (Figure 2-1g). The CVD conditions for Figure 2-1d were the same as those used for Figure 1c, except that 1.0 vol% H_2 was replaced with 1.0 vol% CH_4 ; however, the height of the VA-CNTs was very different. The CNTs were approximately 0.9 mm in height at $t_{\text{Fe}} \approx 0.5$ nm, and were taller than those produced without CH_4 over a wide range of t_{Fe} values (Figure 2-1g). Figure 2-1e,f shows the Raman spectra for the CNTs shown in Figure 2-1c,d, respectively, taken at their tops at different positions. For the VA-CNTs grown without CH_4 at $t_{\text{Fe}} \leq 0.6$ nm (Figure 1e), the G-band peak at $\approx 1590 \text{ cm}^{-1}$ was branched, and the RBM peaks appeared clearly, illustrating the growth of the SWCNTs, as we reported previously [14,16,19]. For the VA-CNTs grown with CH_4 (Figure 2-1d), however, the Raman spectra were quite different. The G-band peak was sharp and branched, and RBM peaks were clearly observed for a wider range of t_{Fe} , showing that the SWCNTs were synthesized under a wider range of catalyst conditions. The G-band to D-band peak intensity ratios (Figure 2-1h) were much larger for the CNTs grown with CH_4 than for those grown without CH_4 , which indicated the higher quality of the former compared with the latter. In the following sections, we carefully examined these remarkable effects of CH_4 in enhancing the height and quality of VA-SWCNTs for $0.5 \leq t_{\text{Fe}} \leq 1$ nm; under these conditions, the SWCNTs grew to ~ 1 mm in height.

Figure 2-2 shows the photographs of VA-SWCNTs synthesized without (a) and with (b) the addition of CH_4 throughout annealing and CVD process with a uniform catalyst of $t_{\text{Fe}} = 0.7$ nm, and the corresponding SEM images. It can be found that the height of SWCNTs with CH_4 (around 1.3 mm, Figure 2-2b) is larger than without CH_4 (around 1.1 mm, Figure 2-2a). SEM images taken at the middle of the arrays showed that they were vertical aligned. Raman spectra taken at the top of the forests showed that G-band to D-band peak intensity ratios was

much larger for with CH_4 ($I_G/I_D=12.6$, Figure 2-2b,d) compared to without CH_4 ($I_G/I_D=5.4$, Figure 2-2a,c), this was agreed with the results of CNTs grown on the combinatorial catalyst library using H_2 / without and with CH_4 .

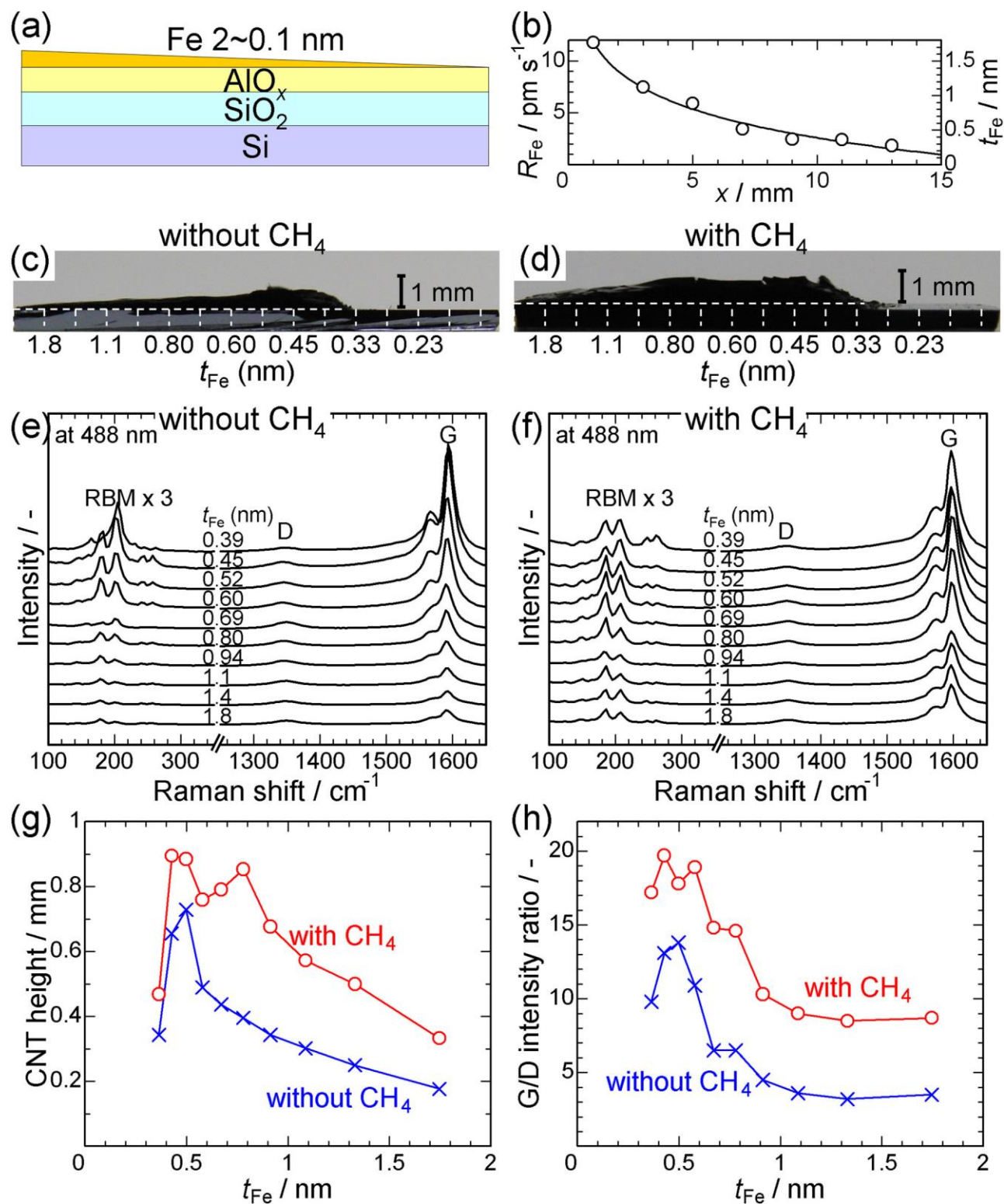


Figure 2-1. VA-CNTs grown on combinatorial Fe/AlO_x catalyst libraries under standard conditions for 10 min without and with CH₄. (a) Schematic of the Fe/AlO_x catalyst library. (b) Profiles of Fe deposition rate (R_{Fe}) and nominal Fe thickness (t_{Fe}) vs. position in the library (x). Digital images (c,d) and Raman spectra (e,f) for the CNTs grown on the libraries under the condition of 26 vol% H₂/ 50 ppmv H₂O/ 0.3 vol% C₂H₂/ Ar without CH₄ (c,e) and 25 vol% H₂/ 50 ppmv H₂O/ 0.3 vol% C₂H₂/ Ar with 1 vol% CH₄ (d,f). Heights (g), and G/D intensity ratios (h) of the CNTs at different t_{Fe} . The Raman spectra were taken at the top of the VA-CNTs, using an excitation wavelength of 488 nm.

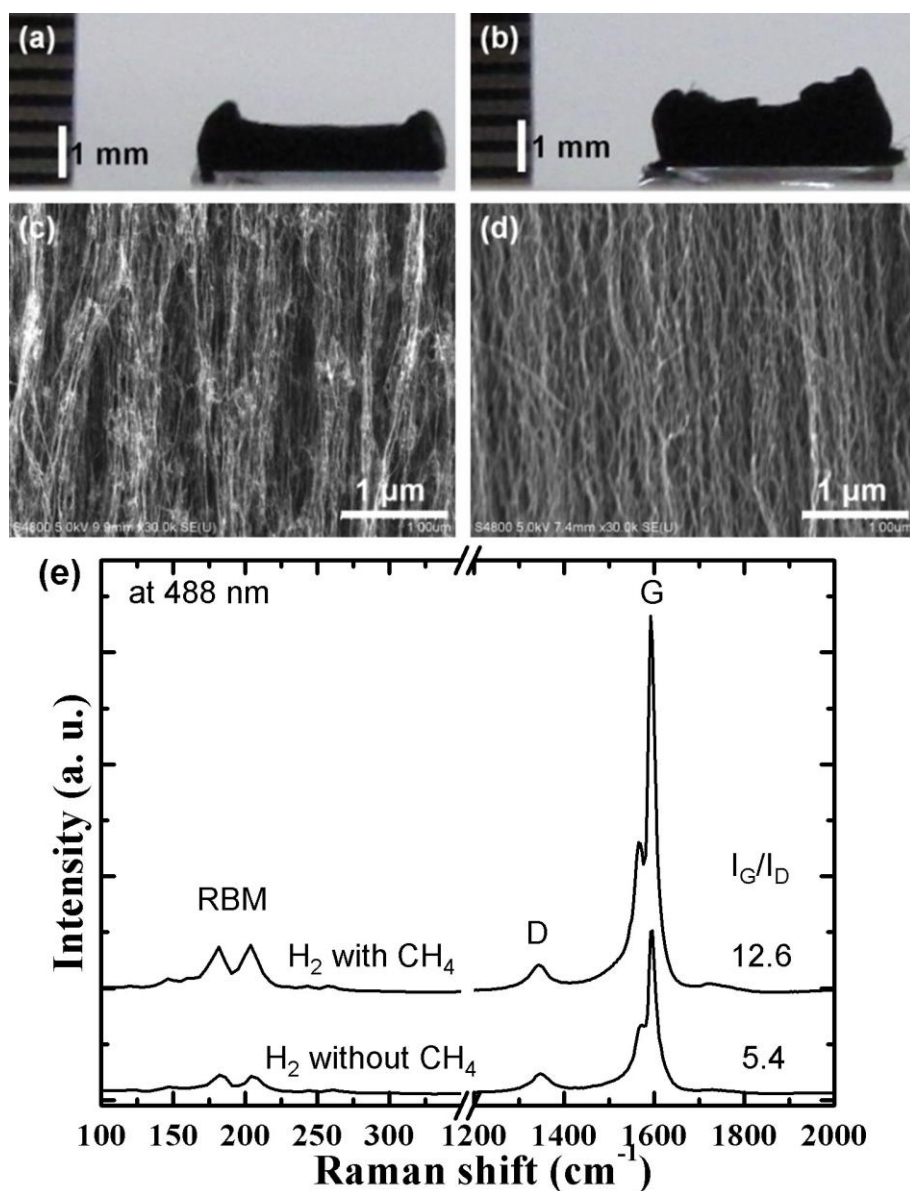


Figure 2-2. Photographs (a,b), and SEM images (c,d) of the SWCNT arrays synthesized 26 vol% H₂/ 50 ppmv H₂O/ 0.3 vol% C₂H₂/ Ar without CH₄ (a,c), and 25 vol% H₂/ 50 ppmv H₂O/ 0.3 vol% C₂H₂/ Ar with 1 vol% CH₄ (b,d), without CH₄ (a,c) and with CH₄ (b,d) throughout catalyst annealing and CVD. CVD was carried out for 10 min. The SEM images were taken in the middle of the arrays. (e) Raman spectra of the SWCNT arrays, measured at the top of the arrays using an excitation wavelength of 488 nm.

2.4 Effects of CH₄ during catalyst annealing and CVD

To investigate the effects of CH₄ during the synthesis of the SWCNTs, we used a digital camera to monitor the growth of VA-CNTs every 10 s. The photos shown in Figure 2-3 were taken at 3 min intervals under the conditions: (a) annealing and CVD without CH₄, (b) annealing with CH₄ and CVD without CH₄, (c) annealing without CH₄ and CVD with CH₄, and (d) annealing and CVD with CH₄. At the beginning of the CNT growth, the CNT heights were similar in all of the samples, except for the threshold in t_{Fe} for the VA-CNT growth; (a) ~ 0.6 nm, (b,c) ~ 0.5 nm, and (d) < 0.5 nm (see the photos taken at 6 min). The differences in the heights became prominent in the later stages; in the final stage, the VA-CNTs were the shortest (~ 1.5 mm) under the (a) conditions, and the tallest (maximum height > 2.5 mm) under the (d) conditions (see the photos taken after the samples were cooled). Near the threshold Fe thickness, the VA-CNTs peeled off from the substrates, due to the tension produced by the VA-CNTs growing faster and taller nearby [14]. Figure 2-4 shows the time profiles for the heights of the VA-CNTs at $t_{Fe} = 0.7$ nm. The VA-CNTs peeled off the substrate at 650-700 s with (a) and 750-800 s with (c), whereas they grew continuously for ~1300 s with (b), and ~1500 s with (d). The growth lifetime and final height were the shortest

for (a) (750-800 s and 0.9 mm), and the largest for (d) (1500 s and 2.2 mm). The growth rate for (c) is somewhat larger than the others (a,b,d). As discussed later for Figure 2-5, annealing without CH₄ resulted in the lower density of catalyst particles, which may resulted in the lower mass density of the CNT forests and thus the larger height increase (growth rate). But the growth curves obtained using the catalyst library is not suitable for the detailed discussion because the CNTs growing nearby at different t_{Fe} interact with each other. The addition of CH₄ during the catalyst annealing and CVD enhanced the VA-CNT height, mainly by enhancing their growth lifetime rather than the growth rate.

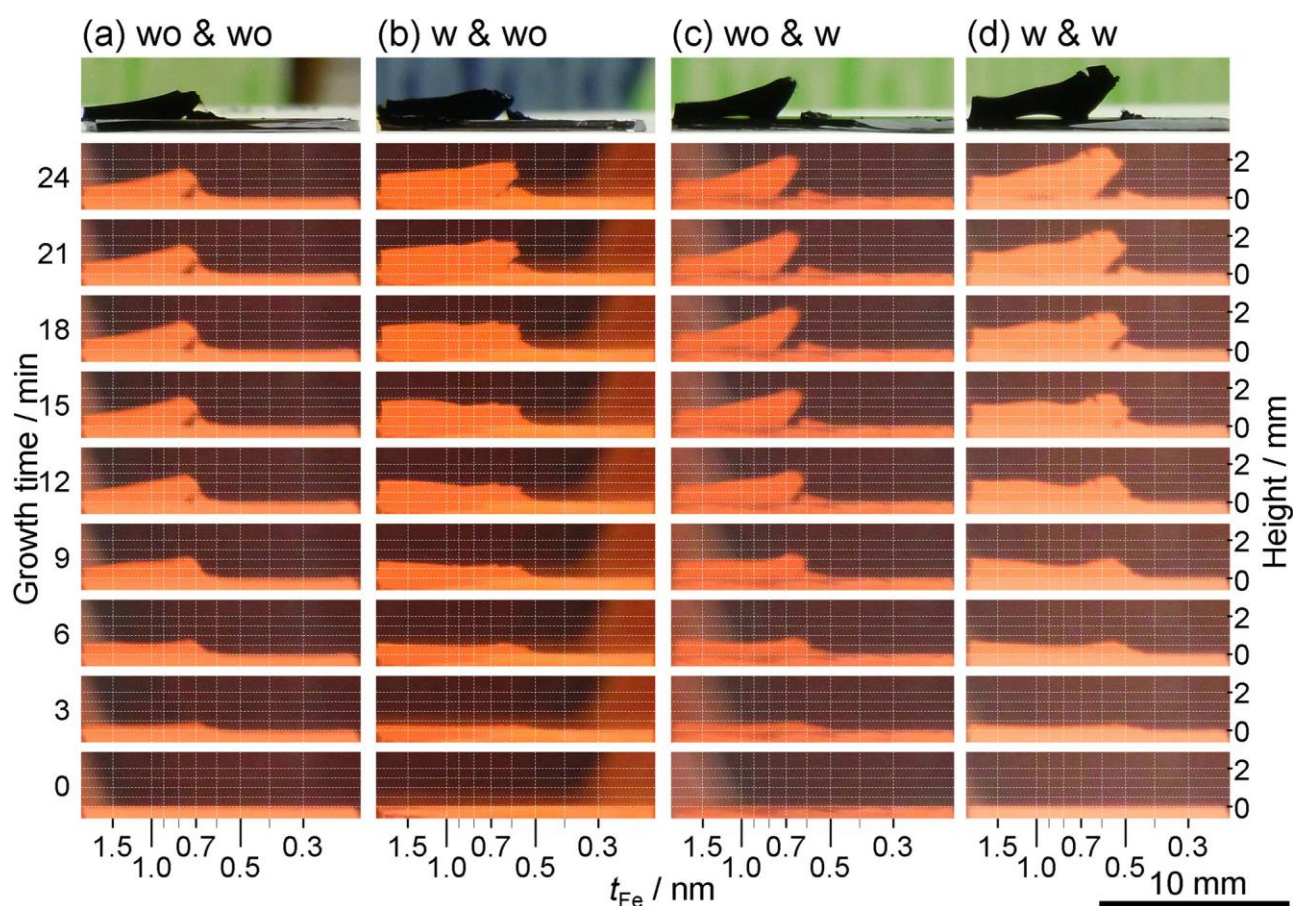


Figure 2-3. Photographs of the VA-CNTs taken at 3 min intervals during growth, under the conditions of: (a) annealing 26 vol% H₂/ Ar/ 50 ppmv H₂O/ Ar balance and CVD 26 vol%

H₂/ 50 ppmv H₂O/ 0.3 vol% C₂H₂/ Ar without CH₄, (b) annealing 25 vol% H₂/ 1 vol% CH₄/ Ar/ 50 ppmv H₂O/ Ar balance and CVD 26 vol% H₂/ 50 ppmv H₂O/ 0.3 vol% C₂H₂/ Ar without CH₄, (c) annealing 26 vol% H₂/ Ar/ 50 ppmv H₂O/ Ar balance without CH₄ and CVD 25 vol% H₂/ 50 ppmv H₂O/ 0.3 vol% C₂H₂/ Ar with 1 vol% CH₄, (d) annealing 25 vol% H₂/ 1 vol% CH₄/ Ar/ 50 ppmv H₂O and CVD 25 vol% H₂/ 50 ppmv H₂O/ 0.3 vol% C₂H₂/ Ar with 1 vol% CH₄. The top images were taken after the corresponding samples were cooled.

The scale bar applies for all of the images.

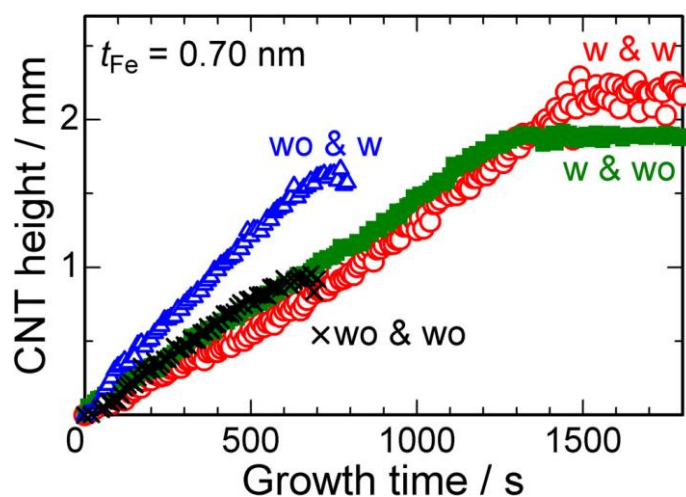


Figure 2-4. Time profiles of CNT heights for $t_{Fe} = 0.70$ nm, under the conditions of: annealing 25 vol% H₂/ 1 vol% CH₄/ Ar/ 50 ppmv H₂O and CVD 25 vol% H₂/ 50 ppmv H₂O/ 0.3 vol% C₂H₂/ Ar with 1 vol% CH₄ (red open circles), annealing 25 vol% H₂/ 1 vol% CH₄/ Ar/ 50 ppmv H₂O/ Ar balance and CVD 26 vol% H₂/ 50 ppmv H₂O/ 0.3 vol% C₂H₂/ Ar without CH₄, (green closed squares), annealing 26 vol% H₂/ Ar/ 50 ppmv H₂O/ Ar balance without CH₄ and CVD 25 vol% H₂/ 50 ppmv H₂O/ 0.3 vol% C₂H₂/ Ar with 1 vol% CH₄ (blue open triangles), and annealing 26 vol% H₂/ Ar/ 50 ppmv H₂O/ Ar balance and CVD 26 vol% H₂/ 50 ppmv H₂O/ 0.3 vol% C₂H₂/ Ar without CH₄ (black crosses). The samples shown are the same as those shown in Figure 2-3.

2.5 Effects of the addition of CH₄ during the catalyst annealing on the microstructure of the Fe particles.

Figure 2-5 shows AFM images of the Fe/AlO_x surfaces at three different stages: as deposited (a,d,g,j), after annealing under H₂ without CH₄ (b,e,h,k), and after annealing under H₂ with CH₄ (c,f,i,l). Fe was deposited uniformly on separate substrates, with different thicknesses of $t_{\text{Fe}} = 1.0$ nm (a-c), 0.7 nm (d-f), 0.6 nm (g-i), and 0.5 nm (j-l). The inset data shows the number density of the Fe islands or particles. The number density of the Fe particles was approximately 1.5-1.7 times higher when the samples were annealed under H₂ with CH₄ than when they were annealed under H₂ without CH₄. For example, nominally 0.7 nm-thick Fe formed very small islands with a number density of $1.8 \times 10^{12} \text{ cm}^{-2}$, as deposited on the AlO_x surface. After annealing under H₂ without CH₄ (Figure 2-5e), the Fe layer transformed in particles of a larger size and a wider size distribution (see the height distribution on the right of each AFM image), and their number density decreased to $0.90 \times 10^{12} \text{ cm}^{-2}$. After annealing under H₂ with CH₄ (Figure 2-5f), the Fe particles were small and uniform, with number densities as high as $1.3 \times 10^{12} \text{ cm}^{-2}$. Similar results were found for all of the t_{Fe} in Figure 2-5. It is clear that CH₄ had a significant effect in keeping the Fe particles stable with small sizes and high number densities.

We then analyzed the Fe/AlO_x surfaces after annealing (and prior to CVD) using X-ray photoelectron spectroscopy (XPS). Figure 2-6 shows the XPS spectra for the Fe/ AlO_x surfaces after annealing in H₂ without and with CH₄. Note that analysis of the catalyst after CVD is impossible because of the huge amount of CNTs formed on the catalysts. If CNTs are mechanically separated from the substrate, some CNTs remain on the surface. Oxidation can remove the carbon residue, but at the same time the Fe is oxidized. Au is sputtered at a very small thickness on the samples to avoid the charge-up effects and for use as an internal

reference for binding energy values. The shape and intensity of the Au 4d peaks exactly matched (Figure 2-6f), supporting the quantitative comparison of the elemental composition by XPS.

First, we checked if carbon deposits from CH₄ on AlO_x surfaces by comparing the Fe-free AlO_x surfaces annealed under H₂ without and with CH₄. As can be seen in Figure 2-6a, the C 1s peak matches exactly in position and intensity for both surfaces. This result means that carbon does not deposit on AlO_x surface from CH₄ under the annealing condition of this work and the carbon peak originates from the contamination from the environment during transfer from the CVD reactor to the XPS chamber.

Then we analyzed the Fe/ AlO_x surfaces after annealing under H₂ without and with CH₄ (Figure 2-6b–e). Annealing under H₂ without CH₄ yielded the same C 1s peak as in Figure 2-6a, showing only the carbon contamination from the environment. Whereas the annealing under H₂ with CH₄ yielded the enhanced C 1s peak, showing carbon deposition from CH₄ on Fe (note that carbon does not deposit from CH₄ on AlO_x as confirmed by Figure 2-6a). The subtraction of the spectra of the peak without CH₄ (black broken curve) from that with CH₄ (red solid curve) yielded a sharp peak (blue dotted curve), which corresponds to the carbon deposited on Fe. The sharpness of the peak shows the more uniform chemical state of carbon than those from contamination, suggesting graphitic carbon on Fe.

We also evaluated the surface elemental compositions and summarized in Table 2-1. The O/Al atomic ratio was 1.35–1.40, somewhat smaller than the stoichiometric Al₂O₃. The Fe/Al ratio was 0.14, which is much smaller than the expected value of ~1.0 for 0.7-nm-thick Fe (55.85 g/mol-Fe, 7.87 g/cm³, 0.14 mol-Fe/cm³) on 1.3-nm-thick Al₂O₃ beneath the Fe (50.98 g/mol-AlO_{1.5}, 4 g/cm³, 0.078 mol-Al/cm³). The diffusion of Fe into the AlO_x layer possibly

caused the reduction of Fe on the surface to ~ 0.1 nm in nominal thickness [26]. The C/Fe ratio was 3.0 and 7.4 for the Fe/ AlO_x annealed without and with CH_4 , respectively. The subtraction (4.4) should correspond to the carbon deposited due to Fe. This amount corresponds to multiple carbon layer on Fe or monolayer whole over the substrate surface although its structure/chemical state has not been clarified yet. It is possible that CH_4 stabilized the Fe particles during the catalyst annealing by saturating and passivating them with carbon, thus reducing their surface energy, where the passivation layer was thin enough to allow the CNT growth in the successive CVD step and to allow the oxidation of Fe particles during their exposure to air.

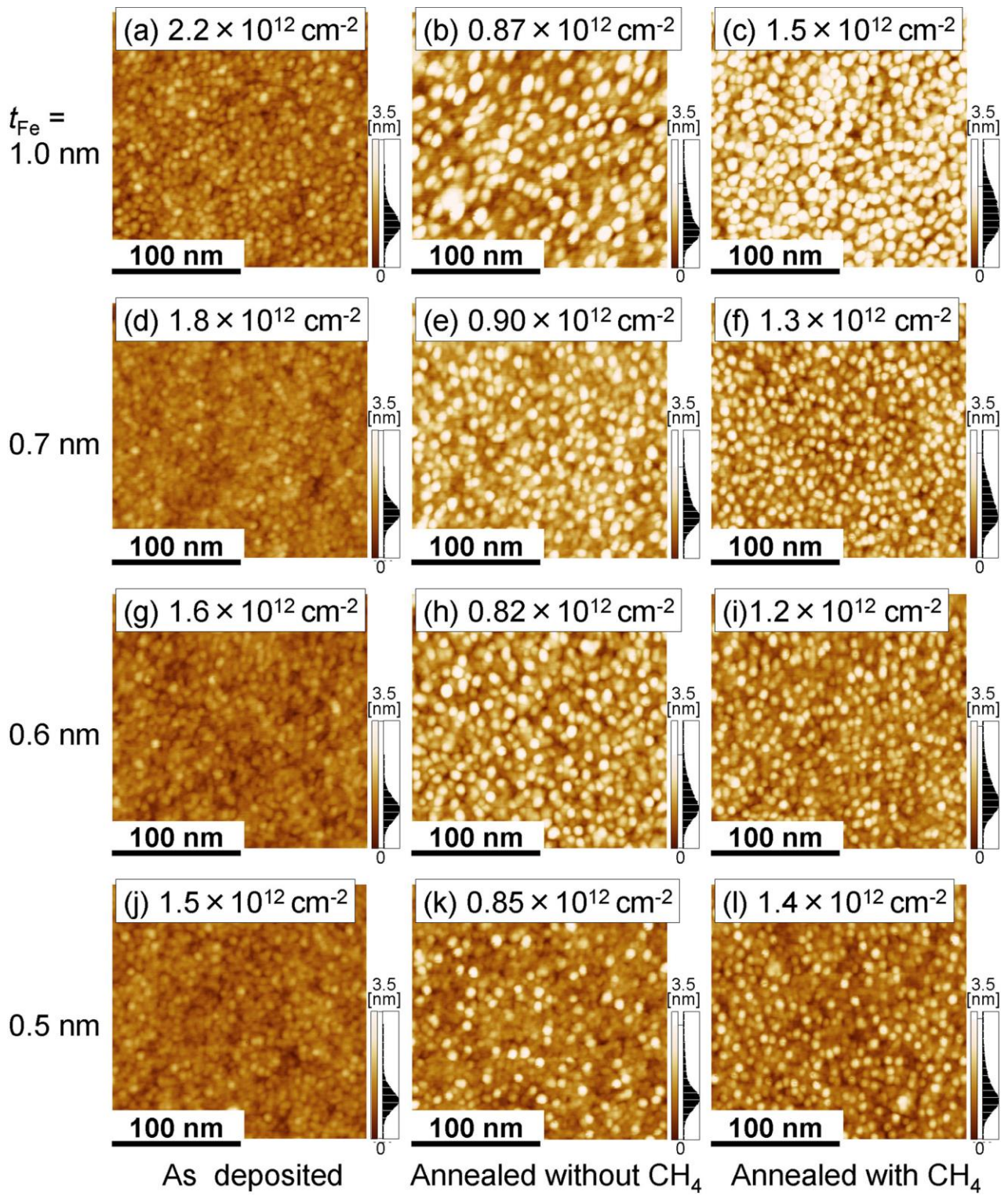


Figure 2-5. AFM images of the Fe/AlO_x surfaces as-deposited (a,d,g,j), after annealing at 800 °C for 5 min under 26 vol% H₂/ Ar/ 50 ppmv H₂O/ Ar balance without CH₄ (b,e,h,k), and annealing under 25 vol% H₂/ 1 vol% CH₄/ Ar/ 50 ppmv H₂O/ Ar balance (c,f,i,l). The catalysts were prepared on separate substrates with uniform thicknesses of $t_{\text{Fe}} = 1.0$ nm (a-c), 0.7 nm (d-f), 0.6 nm (g-i), and 0.5 nm (j-l). The insets show the number density of the Fe islands and particles.

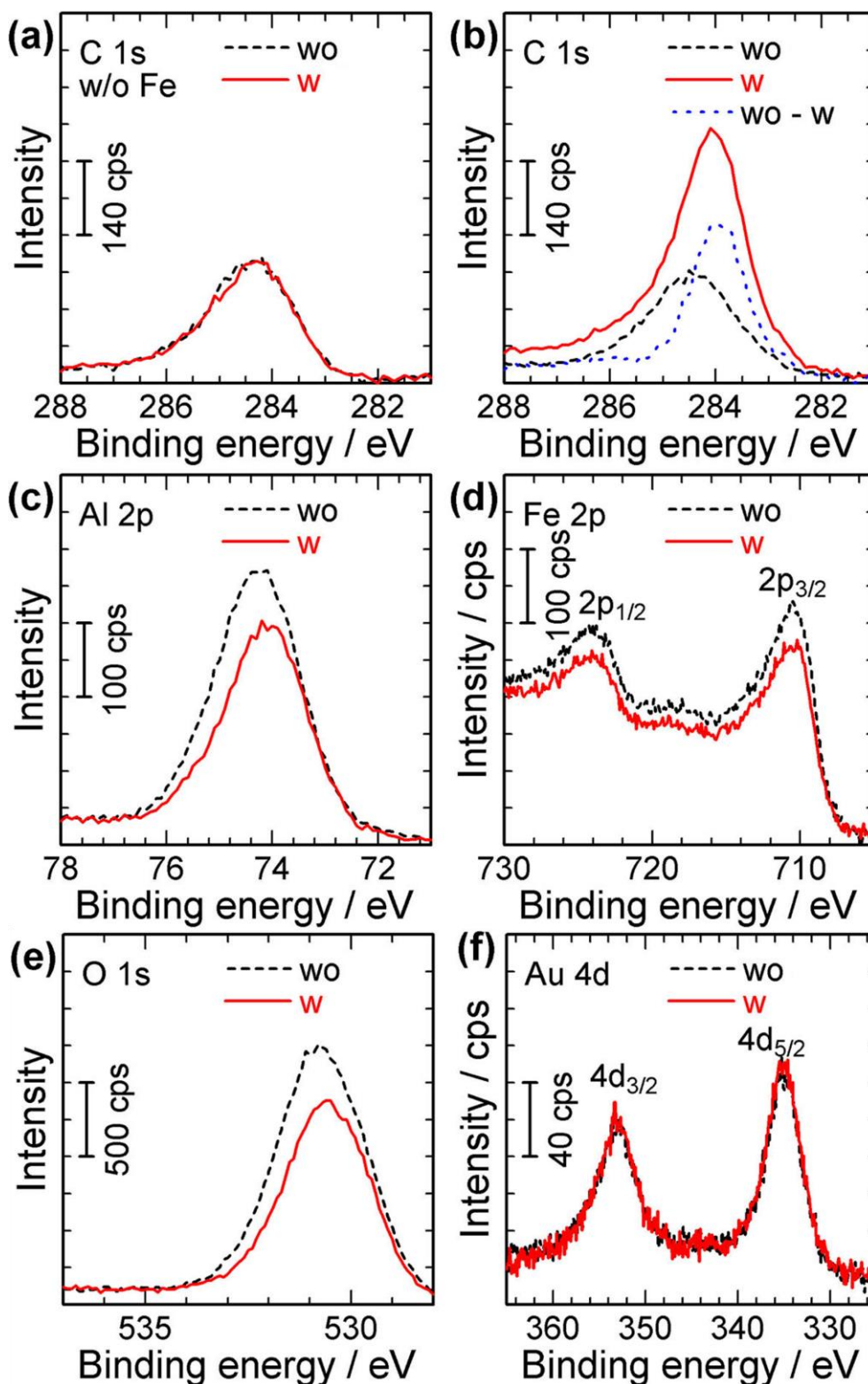


Figure 2-6. XPS spectra for the AlO_x (a), and Fe/AlO_x (b-f) surfaces after reduction at 1073 K for 5 min by 26 vol% H_2 / Ar/ 50 ppmv H_2O / Ar balance without CH_4 , and 25 vol% H_2 / 1 vol% CH_4 / Ar/ 50 ppmv H_2O / Ar balance. For Fe/AlO_x , the Fe was uniformly deposited on

separate substrates with $t_{\text{Fe}} = 0.7$ nm. Prior to the XPS measurements, a thin Au layer was sputter deposited on these two samples as a reference, and the binding energy was calibrated using the Au 4d_{5/2} peak at 335.1 eV. The exact coincidence of the Au 4d spectra between the two samples (f) supported the direct and quantitative comparison of these two samples. The exact coincidence of the C 1s spectra for the AlO_x surfaces (a) showed that there was no carbon deposition on the Fe-free AlO_x surfaces during annealing with CH₄. For the C 1s spectra for the Fe/AlO_x surfaces (b), the difference between the two spectra is also shown.

Table 2-1. Elemental compositions and ratios of the annealed Fe/AlO_x surfaces by XPS.

Condition (CH ₄)	Fe / at% (2p _{3/2})	O / at% (1s)	Au / at% (4d _{5/2})	C / at% (1s)	Al / at% (2p _{3/2})	O/Al	Fe/Al	C/Fe
without	4.6	46.7	1.6	13.6	33.5	1.40	0.14	3.0
with	3.8	37.9	2.0	28.4	28.0	1.35	0.14	7.4

2.6 Effect of the addition of CH₄ during CVD on the diameter of the SWCNTs

We previously observed an increase in the diameter of millimeter-tall VA-SWCNTs, from 1.5-2 nm at the top, to 3-4 nm at the bottom [14,17,19]; this was attributed to the coarsening of the Fe particles[14,17,19] through Ostwald ripening [13] during CVD. The coarsening of the catalyst is also closely related to the termination of CNT growth [18,27]. Because there is a close relationship between the diameter of the catalyst particles and that of the SWCNTs [28,29], the change in the diameter of the SWCNTs at different positions along their height should reflect the history of the change in the diameter of the catalyst particles

during CVD. We therefore analyzed the SWCNTs in detail using transmission electron microscopy (TEM).

We synthesized VA-SWCNTs on separate substrates with a uniform catalyst of $t_{\text{Fe}} = 0.7$ nm, without and with CH_4 throughout catalyst annealing and CVD. As shown in Figure 2-2, the SWCNTs were vertically aligned, and were taller when CH_4 was added. The Raman spectra and the G-band to D-band intensity ratios confirmed that the SWCNTs were of better quality when CH_4 was added, which was consistent with the results shown in Figure 2-1. A portion of the VA-SWCNTs was picked up using tweezers, laid on a TEM grid, and observed (using TEM) at various depths from the top of the VA-SWCNTs (Figure 2-7) [17]. All of the CNTs were SWCNTs, and no MWCNTs were observed at any depths, similar to our previous reports [14,17,19]. The inset histograms for the SWCNT diameter distributions showed that the diameter was smaller when the synthesis was performed with CH_4 , and that it increased with increasing depth. Figure 2-7i shows the average diameter of the SWCNTs at different depths from the top of the VA-SWCNTs. The diameter increased from 2.1 to 3.6 nm in the case without CH_4 addition, while it increased from 1.9 to 3.0 with CH_4 addition. Because SWCNTs grow in the root growth mode, this result shows that the diameter of SWCNTs increased with time during CVD. Although the SWCNTs increased in diameter regardless of the addition of CH_4 , SWCNTs with smaller diameters nucleated and grew from the smaller catalyst particles (Figure 2-5), and retained their smaller diameters when CVD was performed with the addition of CH_4 . CH_4 suppressed the coarsening of the catalyst to some extent, during both the catalyst annealing and the CVD, yielding taller VA-SWCNTs (Figures 2-1,2) with smaller diameters (Figure 2-7).

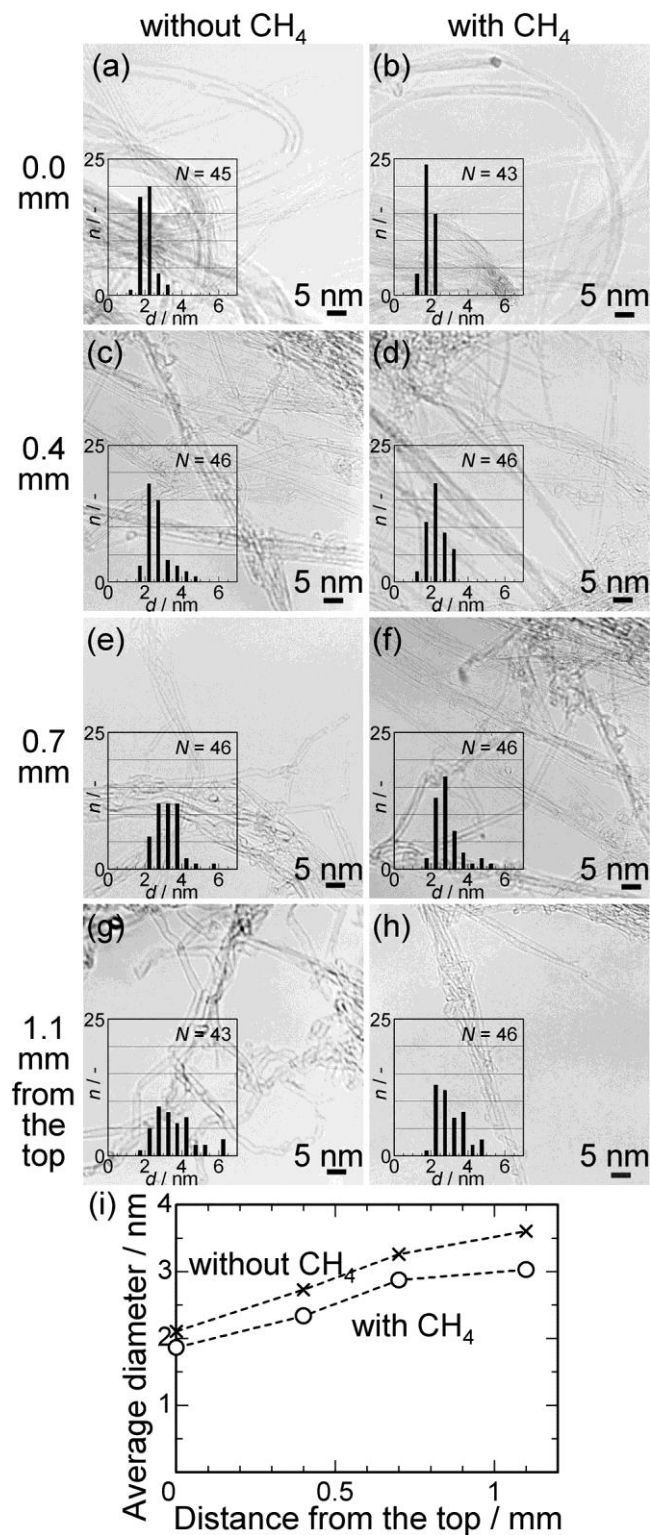


Figure 2-7. TEM images and diameter distributions of SWCNTs, observed at different depths from the top of the VA-SWCNTs. The SWCNTs were grown for 10 min on separate substrates with a uniform catalyst of $t_{\text{Fe}} = 0.7$ nm, under the conditions of 26 vol% H₂/ 50

ppmv H₂O/ 0.3 vol% C₂H₂/ Ar without CH₄ (a,c,e,g) and 25 vol% H₂/ 50 ppmv H₂O/ 0.3 vol% C₂H₂/ Ar with 1 vol% CH₄ (b,d,f,h), without CH₄ (a,c,e,g) and with CH₄ (b,d,f,h) throughout catalyst annealing and CVD. The change in the average diameter of the SWCNTs was plotted against the depth from the top of the VA-SWCNTs in (i).

2.7 Possible role of CH₄ during catalyst annealing and during CVD

Figure 2-8 summarizes the possible role of CH₄ during the catalyst annealing and the CVD growth of the VA-SWCNTs. After sputter-deposition and exposure to air, the Fe was in an oxidized state, and had a very fine particulate island structure (Figures 2-5a,d,g,j). When annealed under H₂ without CH₄, the increased surface energy of the reduced Fe drove the coarsening of the Fe particles, resulting in larger Fe particles and reduced number densities (Figures 2-5b,e,h,k). In contrast, when the annealing was performed under H₂ with CH₄, carbon deposited at a small amount (Figure 2-6), which possibly saturated Fe particles and passivated their surface, reducing their surface energy and thus suppressing the driving force for the coarsening process, resulting in small Fe particles with high number densities (Figures 2-5c,f,i,l). However, CH₄ neither deactivated the catalyst particles by forming "onions", nor grew CNTs under our experimental conditions. The reactivity of CH₄, which is much smaller than that of C₂H₂ [30], should have been sufficient to just stabilize small Fe particles. The addition of CH₄ was also effective in the subsequent CVD step, in allowing the SWCNTs to grow taller (Figure 2-4), and in suppressing increases in the diameter of the growing SWCNTs (Figure 2-7). Such effects can be understood in a fashion similar to the annealing step; *i.e.*, CH₄ stabilized the small Fe particles, and prevented them from coarsening through Ostwald ripening. Although we did not observe the mass loss of Fe through the subsurface

diffusion to the AlO_x underlayer, which reportedly occurs at the later stage than Ostwald ripening [31], CH_4 may show some effect in suppressing the mass loss, too, for the case of longer CVD time. The question remains as to why CH_4 was needed during CVD, because there was a much larger influx of carbon from the C_2H_2 (millimeter length corresponding to 10^{6-7} layers) than from the CH_4 (up to a few layers).

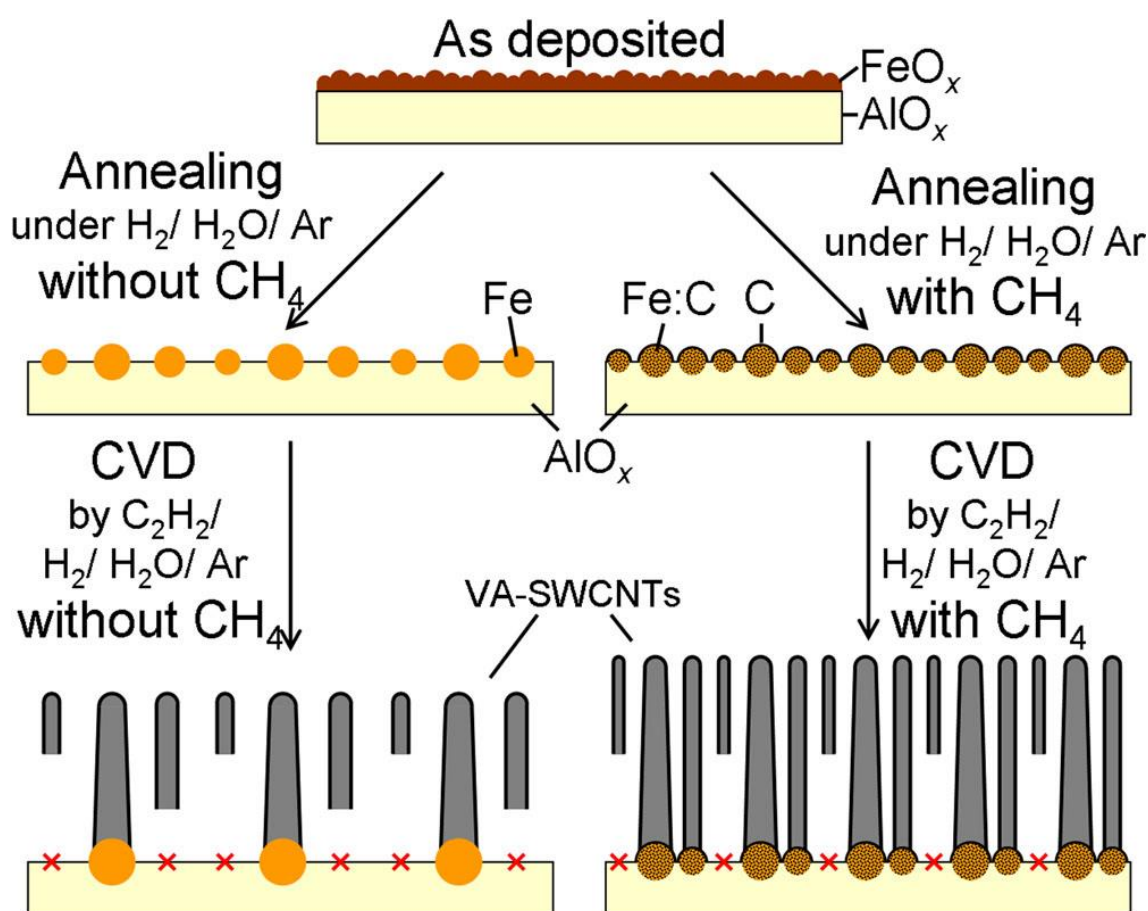


Figure 2-8. Schematic representation of the catalyst annealing and CVD growth of VA-SWCNTs, without and with CH_4 .

2.8 Confirmation of absence of the CH₄ steam reforming effect by gas chromatography

XPS analysis showed that CH₄ is supposed to stabilize the Fe particles during the catalyst annealing by saturating and passivating them with carbon, thus reducing their surface energy and realizing catalyst particles small and dense. However, it is unclear if there is methane steam reforming occurring or not during CVD. In order to confirm this, we analyzed the composition of the carbon-containing species in the effluent gas from the C₂H₂-CVD reactor by GC-FID at 1 min interval during 10 min CVD (Figure 2-9). We first supplied the CVD gas to the reactor tube at room temperature (r. t.) to eliminate the influence of the catalytic reaction, and used the data as the reference. Under the condition without CH₄ addition and with 50 ppmv H₂O (Figure 2-9a), for the effluent gas during CVD, CH₄, C₂H₂, C₂H₆ and C₂H₄ were the main carbon containing species, and CO and CO₂ were below the detection limit (1 pg/s). With 1 vol% CH₄ addition without H₂O (Figure 2-9b), the carbon-based content of CH₄ is 1.3 times higher than C₂H₂ because we inlet 1 vol% CH₄ with 0.3 vol% C₂H₂ during CVD. Although there is some deviation for the CH₄ content from the inlet content, the gas composition in (b) except for CH₄ was the same as (a), showing the minimal decomposition of CH₄ under the condition (b). Figure 2-9c shows the effluent gas composition during CVD under the condition with 1 vol% CH₄ and 50 ppmv H₂O addition. Compared with condition (b), the gas composition of (c) was the same, again showing the minimal decomposition of CH₄ during CVD. Because of the very small content of H₂O, no CH₄ steam was found during CVD. I also checked the change in CH₄ concentration during catalyst annealing without and with H₂O addition, and confirmed that there was negligible change (from 1.0 vol% to 0.98 vol% for both conditions (d) and (e)). Both CO and CO₂ were below the detection limit for both conditions (d) without H₂O and (e) with 50 ppmv H₂O.

Therefore, we conclude that the effect of CH₄ steam reforming is negligible during both catalyst annealing and CVD process.

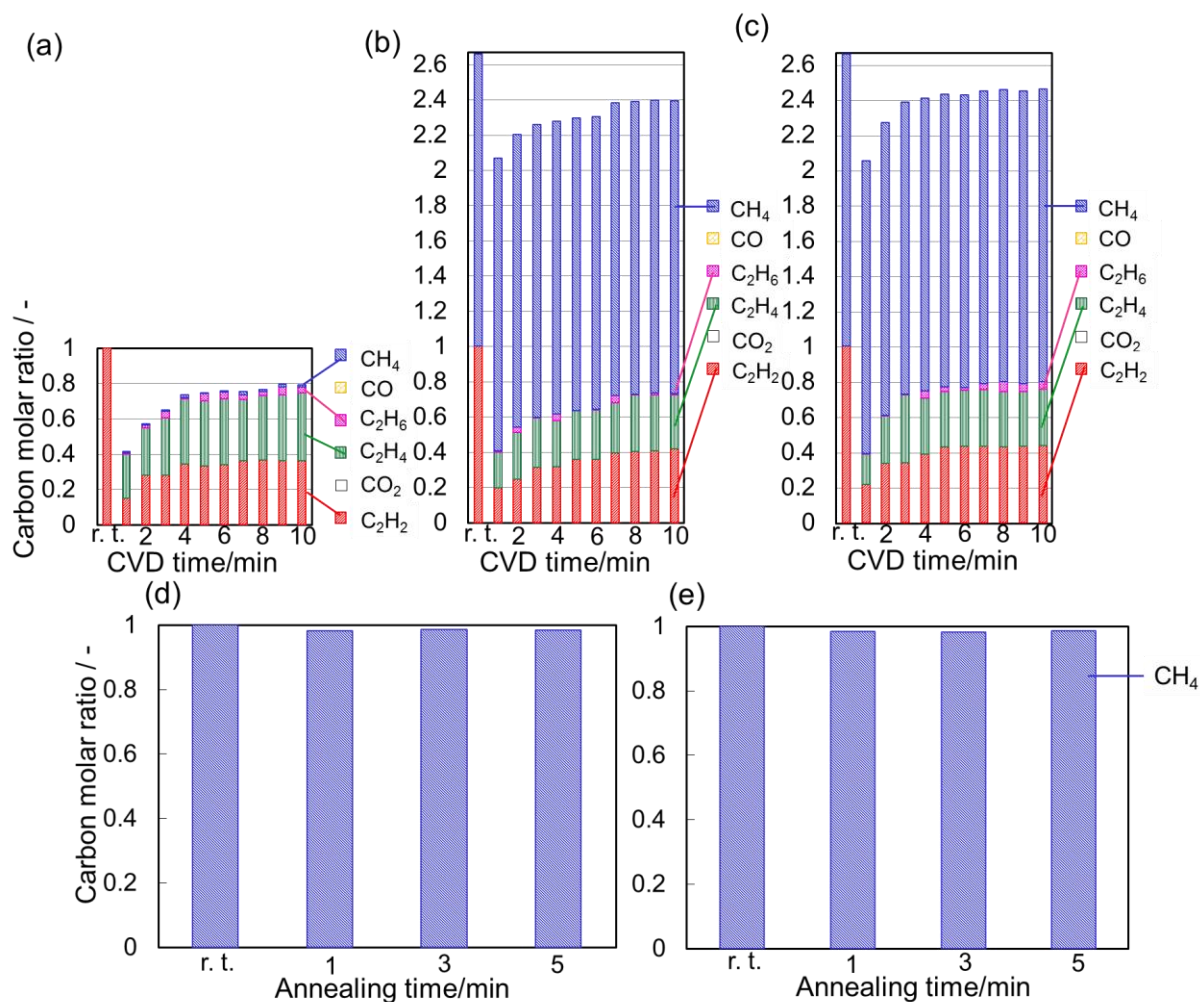


Figure 2-9. Gas compositions of the effluent gas during CVD analyzed by GC under the conditions of 26 vol% H₂/ 50 ppmv H₂O/ 0.3 vol% C₂H₂/ Ar with 0 vol% CH₄ (a), 25 vol% H₂/ 0 ppmv H₂O/ 0.3 vol% C₂H₂/ Ar with 1 vol% CH₄ (b), and 25 vol% H₂/ 50 ppmv H₂O/ 0.3 vol% C₂H₂/ Ar with 1 vol% CH₄ (c). Gas compositions of the effluent gas during catalyst annealing under the condition of 25 vol% H₂/ 1 vol% CH₄/ Ar without H₂O (d) and with 50 ppmv H₂O (e).

2.9 Effect of different CH₄ concentration on SWCNT synthesis

With 1 vol% CH₄ addition, we obtained SWCNTs with larger height and smaller diameter. In order to confirm the effect of different CH₄ addition on SWCNT synthesis, we performed additional experiments with CH₄ concentrations of 0 (Figure 2-10a), 0.1 (Figure 2-10b), 1 (Figure 2-10c) and 10 vol% (Figure 2-10d). Figure 2-10 shows the photographs of SWCNTs grown on Fe/AlO_x surface with $t_{\text{Fe}} = 0.70$ nm and also the corresponding cross-section SEM images for them under different CVD conditions. Table 2-2 shows the results comparing the height of SWCNTs and their graphitic to defect peak intensity ratio (I_G/I_D) with different CH₄ concentrations. With 0.1 vol% CH₄ addition (Figure 2-10b), VA-SWCNTs is around 1.1 mm in height with $I_G/I_D = 7.3$. Compared with the condition without CH₄ addition with 1 mm in height (Figure 2-10a), there is a little improved, while the G band and D band ratio is larger, which means that CH₄ addition can improve the quality of SWCNTs. After increasing CH₄ addition to 10 vol% (Figure 2-10b,d), we can notice that the height of VASWCNTs is larger compared with both without and with 0.1 vol% CH₄ (Figure 2-10a and c), which is around 1.2 mm. However, the height is not as large as with 1 vol% CH₄ addition (1.3 mm in height, Figure 2-10c) and the G band to D band ratio is also smaller ($I_G/I_D = 10.7$). Therefore, SWCNTs are of higher quality with the addition of CH₄. 1 vol% CH₄ addition is the best to improve the height and quality of SWCNTs. The CH₄ addition showed the best effect at 1 vol% addition but improved the SWCNT growth to a certain extent for a wide range from 0.1 to 10 vol%. The change in the height of SWCNTs was not so significant, whereas the change in the graphitic to defect peak intensity ratio (I_G/I_D) by Raman spectroscopy was more significant.

Table 2-2. Comparing of SWCNTs synthesized with different CH ₄ concentrations				
CH ₄ concentration	0 vol%	0.1 vol%	1 vol%	10 vol%
Height of VASWCNTs	1.0 mm	1.1 mm	1.3 mm	1.2 mm
I_G/I_D	5.2	7.3	13.1	10.7

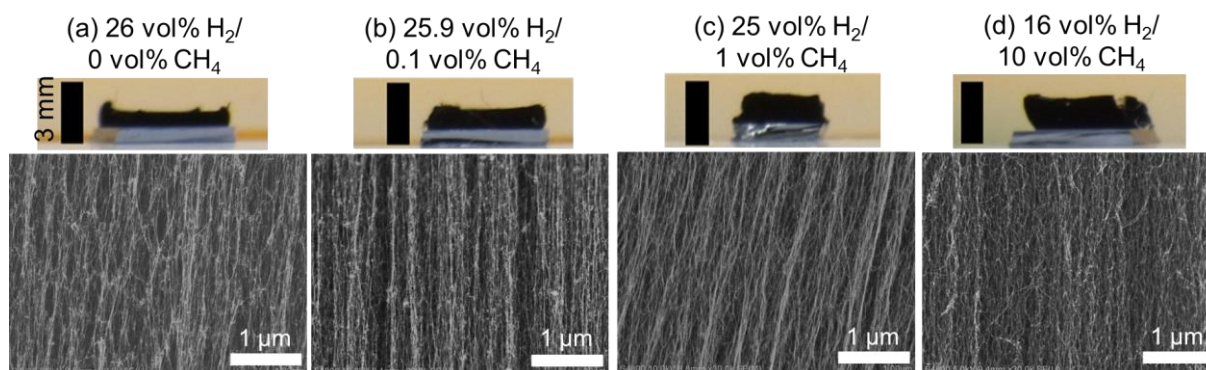


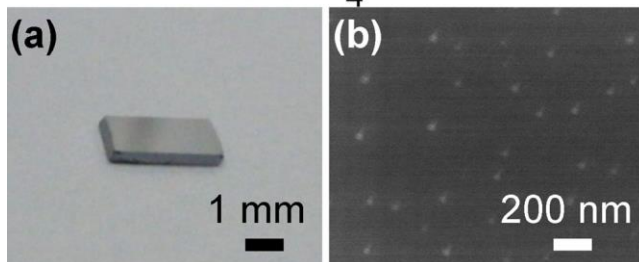
Figure 2-10. Photographs (a,b,c,d) and the corresponding cross-sectional SEM images of VA-SWCNTs synthesized on Fe/AlO_x surface with $t_{Fe} = 0.70$ nm under the CVD conditions of 26 vol% H₂/ 50 ppmv H₂O/ 0.3 vol% C₂H₂/ Ar without CH₄ (a), 25.9 vol% H₂/ 50 ppmv H₂O/ 0.3 vol% C₂H₂/ Ar with 0.1 vol% CH₄ (b), 25 vol% H₂/ 50 ppmv H₂O/ 0.3 vol% C₂H₂/ Ar with 1 vol% CH₄ (c), and 16 vol% H₂/ 50 ppmv H₂O/ 0.3 vol% C₂H₂/ Ar with 10 vol% CH₄ (d).

2.10 Effects of other hydrocarbons: Catalyst annealing under H₂ with CH₄, C₂H₄, and C₂H₂.

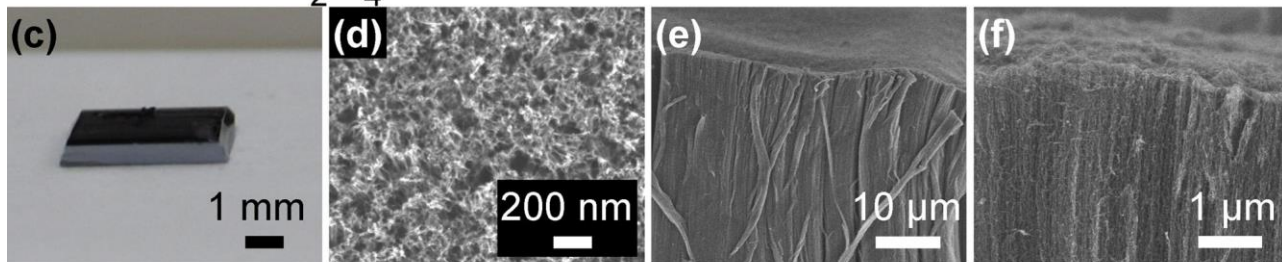
We next examined the addition of C₂H₂ and C₂H₄—which are popular and efficient carbon feedstocks for SWCNTs—during "catalyst annealing", *i.e.*, during heating to and holding for 5 min at 800 °C, and compared their effects with that of CH₄. Figure 2-11a,c,g

shows photographs of the Fe/AlO_x surfaces ($t_{\text{Fe}} = 0.70$ nm) after "annealing" under H₂ with CH₄, C₂H₄, and C₂H₂, respectively. No CNTs grew with the addition of CH₄ (Figures 2-11a,b) and only catalyst annealing took place. Irregularly big particles were observed at a very low density on the substrate surface (Figure 2-11b). Note that the resolution of the SEM was insufficient to observe the tiny particles observed by AFM (Figure 2-5). When C₂H₄ was added, not only the catalyst annealing but also CVD took place and 0.1 mm-tall VA-CNTs grew uniformly on the substrate (Figures 2-11c-f). The CNTs were well aligned vertically, and their Raman spectrum (Figure 2-13a) showed a branched G-band peak with a RBM peak, which are characteristic for SWCNTs. Their G/D ratio of 5.7 was similar to that of SWCNTs grown using C₂H₂, without the addition of CH₄ (Figure 2-1e,h); this indicated that C₂H₄ played a role as a carbon feedstock, but did not play a role in keeping the Fe particles small and dense. Note that C₂H₄ pyrolyzes and yields C₂H₂ under our experimental conditions (a residence time of 4 s at 800 °C) [32], resulting a CNT growth from C₂H₄ [16-18] that was similar to that from C₂H₂ [14,19]. With the addition of C₂H₂, the catalyst annealing as well as CVD took place, however, the CNTs grew only over a part of the substrate in a dotted pattern (Figure 2-11h). In their Raman spectrum (Figure 2-13b), the G-band peak was broad, the RBM peaks were absent, and the G/D intensity ratio was as small as 0.96, indicating the formation of low-quality MWCNTs. These results show that CH₄, which has the lowest reactivity [30], was effective in forming small and densely packed Fe particles that resulted in tall VA-SWCNTs with small diameters; C₂H₄, which has a moderate reactivity [30], had no significant effect on the stability of the Fe particles, and functioned as a feedstock for the VA-SWCNTs; and C₂H₂, which has the highest reactivity [30], deactivated the small Fe particles and yielded MWCNTs during the annealing step (*i.e.*, heating the sample to and holding it at 800 °C under an H₂ environment).

with 1 vol% CH₄



with 1 vol% C₂H₄



with 1 vol% C₂H₂

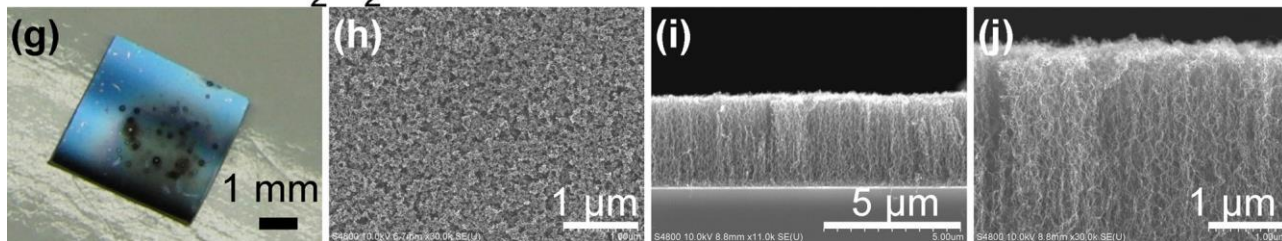
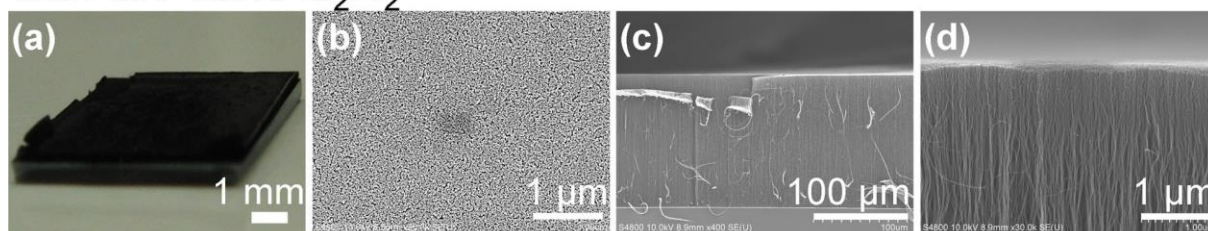


Figure 2-11. Photographs (a,c,g), top-view SEM images (b,d,h), and cross-sectional SEM images (e,f,i,j) of the Fe/AlO_x surfaces ($t_{\text{Fe}} = 0.70$ nm) after "annealing" (*i.e.*, heating to and holding for 5 min at 800 °C) under 25 vol% H₂/ 50 ppmv H₂O/ Ar with 1 vol% CH₄ (a,b), 1 vol% C₂H₄ (c-f), and 1 vol% C₂H₂ (g-j). No CNTs grew with the addition of CH₄ (a), VA-CNTs grew uniformly with the addition of C₂H₄ (c), and VA-CNTs grew in a small part of the substrate with the addition of C₂H₂ (g). SEM images (h-j) were taken at the black dotted patterns in (g).

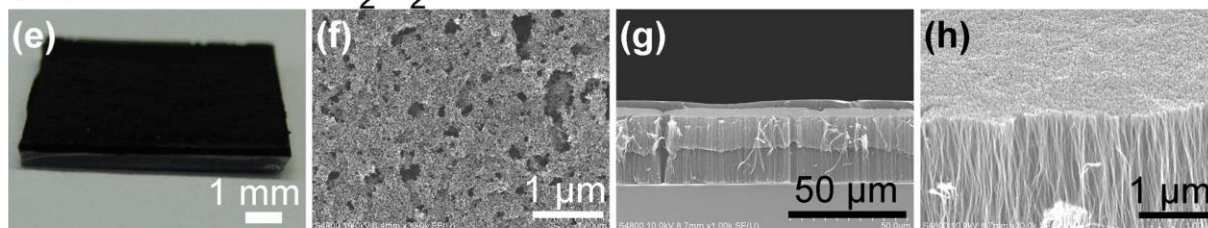
Here arises a question; which are important, the reactivity of the hydrocarbon additives or the carbon deposition rate? We then studied the effect of the C₂H₂ addition for a range of its concentration. With 0.1 and 0.01 vol% C₂H₂, VA-CNTs grew uniformly over the substrate (Figure 2-12a-h). In their Raman spectrum (Figure 2-13c,d), however, the G-band peak was

broad, the RBM peaks were absent, and the G/D intensity ratio was as small as 1.2 and 2.9, respectively, indicating the formation of low-quality MWCNTs. Further decrease in C_2H_2 concentration to 0.002 vol% resulted in no CNT growth (Figure 2-12i,j), and only the irregularly big particles at a very low density were observed in the top-view SEM image. Because this result with 0.002 vol% C_2H_2 was similar with that with 1 vol% CH_4 , we examined CVD using this catalyst. We first "annealed" the Fe/ AlO_x sample under 26 vol% H_2 / 50 ppmv H_2O / Ar with 0.002 vol% C_2H_2 and then carried out CVD with 0.302 vol% C_2H_2 with 26 vol% H_2 / 50 ppmv H_2O / Ar at 800 °C for 10 min, mimicking the condition "with CH_4 throughout" but replacing 1 vol% CH_4 with 0.002 vol% C_2H_2 and 1 vol% H_2 . VA-CNTs grew uniformly over the substrate (Figure 2-12k-n) and had a height of 0.40 mm and G/D ratio of 8.4. Compared with the VA-SWCNTs grown "without CH_4 throughout" having a height of ~ 1 mm and G/D ratio of 5.4 (Figure 2-2), the height was smaller and the G/D ratio was larger. Compared with the VA-SWCNTs grown "with CH_4 throughout" having a height of > 1 mm and G/D ratio of 12.6 (Figure 2-2), both the height and G/D ratio were smaller. It was very difficult to achieve the similar effect of 1 vol% CH_4 by adjusting the C_2H_2 concentration. We conclude that CH_4 having a low reactivity is effective in forming small and densely packed Fe particles and growing tall VA-SWCNTs with small diameters.

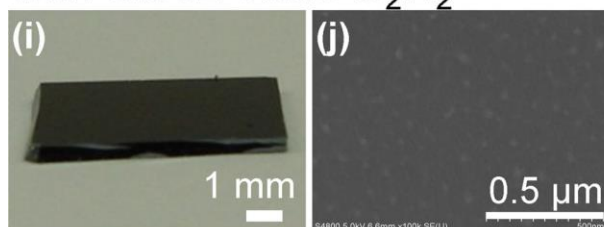
with 0.1 vol% C_2H_2



with 0.01 vol% C_2H_2



with 0.002 vol% C_2H_2



annealing with 0.002 vol% C_2H_2 + CVD

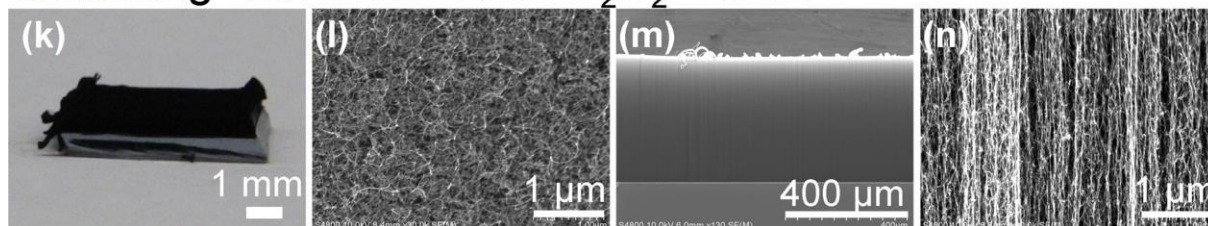


Figure 2-12. Photographs (a,e,i,k), top-view SEM images (b,f,j,l), and cross-sectional SEM images (c,d,g,h,m,n) of the Fe/AlO_x surfaces ($t_{Fe} = 0.70$ nm) after "annealing" (heating to and holding for 5 min at 800 °C) under 26 vol% H₂/ 50 ppmv H₂O/ Ar with C₂H₂ of 0.1 (a-d), 0.01 (e-h), and 0.002 vol% (i,j,k-n). For (k-n), CVD was also done with 0.302 vol% C₂H₂/ 26 vol% H₂/ 50 ppmv H₂O/ Ar at 800 °C for 10 min after annealing.

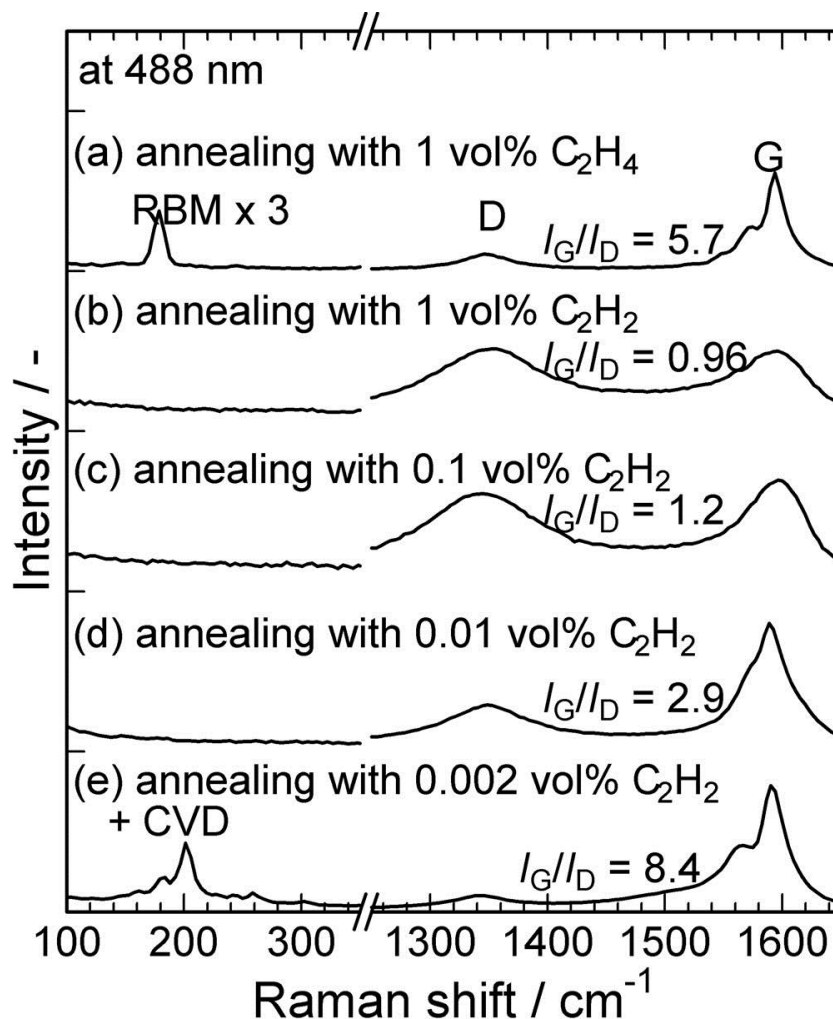


Figure 2-13. Raman spectra for the Fe/AlO_x surfaces with $t_{\text{Fe}} = 0.70$ nm after "annealing" (heating to and holding for 5 min at 800 °C) under 25 vol% H₂/ 50 ppmv H₂O/ Ar with either (a) 1 vol% C₂H₄ (a) or (b) 1 vol% C₂H₂, and under 26 vol% H₂/ 50 ppmv H₂O/ Ar with (c) 0.1 vol% C₂H₂ and (d) 0.01 vol% C₂H₂. For (e), the sample was "annealed" under 26 vol% H₂/ 50 ppmv H₂O/ Ar with 0.002 vol% C₂H₂ and then CVD was done with 0.302 vol% C₂H₂/ 26 vol% H₂/ 50 ppmv H₂O/ Ar at 800 °C for 10 min. The samples were the same as those shown in Figures 2-11c-f (a), 2-11g-j (b), 2-12a-d (c), 2-12e-h (d), and 1-12k-n (e).

2.11 Cost analysis of the source gases for the production of CNTs

This work was in the collaboration with a private company targeting at practical production, they made a cost evaluation and told us that the price of H_2 was not so cheap. But I must make a survey by myself, of course, and made it and showed the results below.

We made a cost analysis not for the basic research on the on-substrate growth of this chapter but for the applied research on the FBCVD in Chapters 3 and 4. In our FBCVD process, productivity (0.6–0.8 g-CNT/ 0.5 L-reactor/h, corresponding to 1.2–1.6 kg-CNT/ m^3 -reactor/ h, reference from Chapter 3 and 4) and carbon yield (40%) are high (about half of those for the gas-phase polymerization process for polyethylene). But the reactant C_2H_2 is fed at a concentration as low as 0.37–1.1 vol% and thus the cost of the other gases are not negligible as shown below. During the survey, we learnt that the price changes largely for the industrial scale, depending on the amount and the contract, and such information is very confidential. The prices of the gas can be obtained in cylinders for the laboratory use mainly and thus use those values in the thesis.

Ar is currently used at the largest amount in our experiments (Table 2-3), it is highly required to replace Ar (725 yen/ m^3) with less expensive N_2 (400 yen/ m^3) as balance gas to decrease the total cost for CNT synthesis. Our group member has already confirmed that CNTs can be synthesized when Ar is replaced with N_2 . If we use liquid N_2 -based N_2 gas, the price decrease further to 75 yen/ m^3 . Under these conditions, N_2 accounts for ~50,000 yen/kg-CNTs and H_2 accounts for ~20,000 yen/kg-CNT. N_2 and H_2 will be recycled in the future process, and the cost will decrease to 1/10. Because the target price of CNTs is ~50,000 yen/kg-CNTs for use as additives and ~5,000 yen/kg for use as main component in

batteries/capacitors, these costs for N₂ and H₂ are not negligible and thus there is a strong demand replacing high-purity H₂ with low-purity H₂ (please note that the price of low purity H₂ is confidential and we could not obtain it). Moreover, H₂ is widely used for various CVD processes for CNT production and our finding of the "CH₄-assist effect" would be beneficial for such processes.

Table 2-3. Amount and the commercial price of the gases used to produce 1 kg CNTs.

		Ar	N ₂	O ₂	H ₂	C ₂ H ₂	Total(Ar)	Total(N ₂)
Amount	m ³ /kg-CNT	691.5	691.5	79.3	90.2	2.5		
Industrial price	yen/m ³	725	400	400	700	2321.93		
	yen/kg-gas					2000		
Gas-cost without gas recycle	yen/kg-CNT	¥501,311	¥276,585	¥31,707	¥63,128	¥5,890	¥602,036	¥377,311
Ar accounts for more than 80% of the total gas-cost and thus must be replaced with N ₂ .								
90% gas-recycle for Ar, N ₂ , and H ₂								
Amount	m ³ /kg-CNT	69.1	69.1	7.9	9.0	2.5		
Gas-cost with 90% gas-recycle for Ar, N ₂ , and H ₂	yen/kg-CNT	¥50,131	¥27,659	¥3,171	¥6,313	¥5,890	¥65,504	¥43,032

*The price is for the 7 Nm³-cylinders. For the industrial scale, it will be reduced by several times.

**Only one of Ar or N₂ is used. In my experiment, I normally use Ar but we have confirmed that N₂ can be used in place of Ar.

***Ar/N₂ and H₂ will be recycled in the practical process. Estimation is made in the lower columns assuming the 90% recycling for these gases.

2.12 Conclusions

In summary, we found that the addition of CH₄ in both the annealing and CVD steps is effective in keeping the Fe particles small and dense, and yielding taller VA-SWCNTs with smaller diameters. During the catalyst annealing, the CH₄ deposited carbon at a small amount on the Fe particles, which prevented the coarsening of the Fe particles through Ostwald ripening, possibly by reducing the surface energy of the Fe particles. CH₄ also prevented the coarsening of the Fe particles during CVD, enhancing the growth lifetime and preventing

increases in the diameter of the VA-SWCNTs. Further study is needed to clarify the role of CH_4 , because there was a huge influx of carbon to the Fe particles from C_2H_2 during CVD. These effects of CH_4 widened the window of catalyst conditions suitable for the rapid growth of VA-SWCNTs. When C_2H_4 (which has a moderate reactivity) was added during the catalyst annealing, it functioned only as a feedstock for CVD, yielding VA-SWCNTs without improving the quality of the SWCNTs. When C_2H_2 (which has a high reactivity) was added during the catalyst annealing, it deactivated the small catalyst particles and yielded non-uniform VA-MWCNTs. CH_4 -assisted CVD is an efficient and practical method that uses H_2 containing CH_4 , which is available as a byproduct in chemical factories.

References

- [1] W. Z. Li, S. S. Xie, L. X. Qian, B. H. Chang, B. S. Zou, W. Y. Zhou, R. A. Zhao, G. Wang, *Science* 274 (1996) 1701.
- [2] Z. W. Pan, S. S. Xie, B. H. Chang, C. Y. Wang, L. Lu, W. Liu, W. Y. Zhou, W. Z. Li, L. X. Qian, *Nature* 394 (1998) 631.
- [3] Y. Murakami, S. Chiashi, Y. Miyauchi, M. Hu, M. Ogura, T. Okubo, S. Maruyama, *Chem. Phys. Lett.* 385 (2004) 298.
- [4] K. Hata, D. N. Futaba, K. Mizuno, T. Namai, M. Yumura, S. Iijima, *Science* 306 (2004) 1362.
- [5] L. Zhang, Y. Q. Tan, D. E. Resasco, *Chem. Phys. Lett.* 422 (2006) 198.
- [6] H. Ohno, D. Takagi, K. Yamada, S. Chiashi, A. Tokura, Y. Homma, *Jpn. J. Appl. Phys.* 47 (2008) 1956.
- [7] H. Sugime, S. Noda, *Carbon* 48 (2010) 2203.
- [8] H. Sugime, S. Noda, *Carbon* 50 (2012) 2953.
- [9] G. G. Zhang, D. Mann, L. Zhang, A. Javey, Y. M. Li, E. Yenilmez, Q. Wang, J. P. McVittie, Y. Nishi, J. Gibbons, H. J. Dai, *PNAS* 102 (2005) 16141.
- [10] Q. Wen, W. Z. Qian, F. Wei, Y. Liu, G. Q. Ning, Q. Zhang, *Chem. Mater.* 19 (2007) 1226.
- [11] D. N. Futaba, J. Goto, S. Yasuda, T. Yamada, M. Yumura, K. Hata, *Adv. Mater.* 21 (2009) 4811.

-
- [12] T. Yamada, A. Maigne, M. Yudasaka, K. Mizuno, D. N. Futaba, M. Yumura, S. Iijima, K. Hata, Nano Lett. 8 (2008) 4288.
- [13] P. B. Amama, C. L. Pint, L. McJilton, S. M. Kim, E. A. Stach, P. T. Murray, R. H. Hauge, B. Maruyama, Nano Lett. 9 (2009) 44.
- [14] K. Hasegawa, S. Noda, ACS Nano 5 (2011) 975.
- [15] T. Yamada, T. Namai, K. Hata, D. N. Futaba, K. Mizuno, J. Fan, M. Yudasaka, M. Yumura, S. Iijima, Nat. Nanotechnol. 1 (2006) 131.
- [16] S. Noda, K. Hasegawa, H. Sugime, K. Kakehi, Z. Zhang, S. Maruyama, Y. Yamaguchi, Jpn. J. App. Phys. 46 (2007) L399.
- [17] K. Hasegawa, S. Noda, Appl. Phys. Express 3 (2010) 045103.
- [18] K. Hasegawa, S. Noda, Jpn. J. Appl. Phys. 49 (2010) 085104.
- [19] K. Hasegawa, S. Noda, Carbon 49 (2011) 4497.
- [20] A. Kaskela, A. G. Nasibulin, M. Y. Timmermans, B. Aitchison, A. Papadimitratos, Y. Tian, Z. Zhu, H. Jiang, D. P. Brown, A. Zakhidov, E. I. Kauppinen, Nano Lett. 10 (2010) 4349.
- [21] R. M. Sundaram, K. K. K. Koziol, A. H. Windle, Adv. Mater. 23 (2011) 5064.
- [22] D. Y. Kim, H. Sugime, K. Hasegawa, T. Osawa, S. Noda, Carbon 49 (2011) 1972.
- [23] D. Y. Kim, H. Sugime, K. Hasegawa, T. Osawa, S. Noda, Carbon 50 (2012) 1538.
- [24] S. Noda, H. Sugime, T. Osawa, Y. Tsuji, S. Chiashi, Y. Murakami, S. Maruyama, Carbon 44 (2006) 1414.

-
- [25] S. Noda, H. Sugime, K. Hasegawa, K. Kakehi, Y. Shiratori, Jpn. J. Appl. Phys. 49 (2010) 02BA02.
- [26] S. M. Kim, C. L. Pint, P. B. Amama, D. N. Zakharov, R. H. Hauge, B. Maruyama, E. A. Stach, J. Phys. Chem. Lett. 1 (2010) 918.
- [27] E. R. Meshot, A. J. Hart, Appl. Phys. Lett. 92 (2008) 113107.
- [28] C. L. Cheung, A. Kurtz, H. K. Park, C. M. Lieber, J. Phys. Chem. B, 106 (2002) 2429.
- [29] A. G. Nasibulin, P. V. Pikhitsa, H. Jiang, E. I. Kauppinen, Carbon, 43 (2005) 2251.
- [30] G. Eres, A. A. Kinkhabwala, H. T. Cui, D. B. Geohegan, A. A. Puretzky, D. H. Lowndes, J. Phys. Chem. B 109 (2005) 16684.
- [31] S. M. Kim, C. L. Pint, P. B. Amama, D. N. Zakharov, R. H. Hauge, B. Maruyama, E. A. Stach, J. Phys. Chem. Lett. 1 (2010) 918.
- [32] R. Itoh, S. Noda, T. Osawa, S. Maruyama, Y. Yamaguchi, 2008 MRS Spring Meeting, P4.26, San Francisco, CA, USA, March 2008.

Chapter 3 - Fluidized bed CVD (FBCVD) of submillimeter-long CNTs using an internal heat-exchange reactor

(Part of this chapter has been published in: Zhongming Chen, et al., Carbon, 2014.)

3.1 Introduction

CNTs have attracted a lot of attention owing to their unique one-dimensional nanostructure and extraordinary electrical, thermal, mechanical, and optical properties. Their ability to form self-organized conductive networks as well as their large specific surface area, high chemical/mechanical stability, and light weight make them an attractive candidate for electrodes of batteries, capacitors, and solar cell devices [1–6]. The low-cost production of CNTs will open many opportunities for their practical application. Different methods have been used to produce high-quality CNTs, including electric arc discharge [7,8], laser vaporization [9], CVD [10–12], and plasma-enhanced CVD [13]. Among these methods, CVD is one of the most commonly used techniques for laboratory- and commercial-scale controllable synthesis of CNTs. FBCVD is one of the most popular ways for the mass production of CNTs because of advantages in terms of providing sufficient surface area for supporting catalysts and growing CNTs, excellent mass and heat transfer, easy scale-up, and continuous operation [14–17]. SWCNTs to MWCNTs have been mass produced by FBCVD. However, CNTs tend to entangle with catalysts and supports and thus need post treatment, which creates additional costs and damages the CNTs.

Since the report in 1996 [18], VA-CNT arrays have been a focus in CNT production because of the uniform tube length, uniform orientation, and extra high purity. Impurity-free,

millimeter-long, SWCNTs have been produced by the water-assisted CVD method [19], and such synthesis is now possible using several CVD recipes on catalyst-supported flat substrates [20–23]. However, the limited surface area of the 2D growth substrate is a major obstacle for the mass-production of such CNTs. To improve the productivity of CNT arrays, some researchers have chosen 3D support materials to extend the reaction surface. Xiang et al. used spherical ceramic beads in a thin fixed-bed and synthesized MWCNT arrays [24–26]. Zhang et al. used vermiculite as catalyst carrier and grew micrometer-tall MWCNT arrays among the layers of vermiculite via FBCVD, and realized the mass production of CNTs at 3.0 kg/h using a pilot plant reactor with an inner diameter of 0.5 m [16,27].

We previously developed an original FBCVD method and realized semi-continuous production of submillimeter-long few-wall CNTs (FWCNTs) from acetylene (C_2H_2) at a high carbon yield $\geq 70\%$ and short gas residence time of ~ 0.3 s [17]. The high gas feed enabled the rapid conversion of C_2H_2 to CNTs but caused insufficient heating of the bead bed when scaled up. In situ catalyst deposition on spherical alumina (Al_2O_3) beads by the FBCVD enabled the semi-continuous operation of catalyst deposition, CNT growth, and CNT separation/collection. However, the catalyst vapor fed through the distributor caused stacking after ~ 20 cycles and resulted in an interrupted semicontinuous operation. In this study, we designed and developed a new FBCVD reactor with an internal heat-exchange and preheating zone, and investigated its performance in producing sub-millimeter-long CNTs. With the new design of the reactor tube, CVD gas can be preheated before contacting with beads. The CNT amount was increased from 0.25 to 0.82 g/cycle while CNTs retained the submillimeter-long array structure. From the transmission electron microscopy (TEM) analysis, we found that the average diameter of the CNTs increased to 11 nm.

3.2 Methods

All processes for catalyst (re)deposition, catalyst reduction, CNT growth, CNT separation, and removal of residual carbons were performed in a single FBCVD reactor (Figure 3-1), similarly to our previous work [17] but using a new reactor tube with an internal heat-exchange and preheating zone. Commercially available Al_2O_3 beads (purity > 99.95 wt.%, 0.5 mm average diameter, and 3.89 g cm^{-3} density, Taimei Chemicals, Japan) were loaded in the reactor with a static bed height of 30 mm. All of the gases except for the catalyst vapor were fed into the outer tube (inner and outer diameters of 50 and 55 mm, respectively). The gas flew down and was preheated by the furnace and the hot effluent gas in the inner tube, and then flew into the inner tube (inner and outer diameters of 40 and 44 mm, respectively) through the distributor at the bottom of the reactor tube. Catalyst vapors of aluminum-isopropoxide and ferrocene were fed directly into the bed through the catalyst line penetrating the distributor from the bottom, minimizing their decomposition in the catalyst line while promoting their decomposition on the “hot beads” (Figure 3-1a, see also the detailed structure in Supplementary data, Figure S1). An AlO_x support layer was formed on the beads in 2 min by supplying aluminum isopropoxide vapor, which was sublimated in an evaporator at 130°C and carried in $450 \text{ standard cm}^3$ Ar gas [$225 \text{ standard cubic centimeter (sccm)}$, 3 atm for 2 min]. AlO_x support layer of a few tens of nanometers in thickness is very important to activate the Fe particles, not only for the growth on flat substrates but also for the FBCVD growth on Al_2O_3 beads with sputtered catalyst. We have carefully adjusted the Ar carrier gas volume to make Fe particles active and fixed it at $450 \text{ standard cm}^3$. Then, Fe particles were formed on the AlO_x layer by sublimating ferrocene carried in $50\text{--}250 \text{ standard cm}^3$ Ar gas ($25\text{--}125 \text{ sccm}$, 2.5 atm for 2 min) at 120°C to adjust the amount of Fe. Deposition of both AlO_x and Fe was performed with 4 vol% O_2/Ar to completely decompose the vapor, and at 20 slm to fluidize

the bed well and uniformly deposit the catalyst on the beads. After reducing the deposited Fe by flowing 26 vol% H₂/0.06 vol% H₂O/Ar at 9.48 slm for 10 min, CVD was performed by flowing 0.37–1.1 vol% C₂H₂/26 vol% H₂/0.06 vol% H₂O/Ar at 9.48 slm for 10–20 min (Figure 3-1b). Note that, the time for catalyst deposition was separated from that for CNT growth to obtain better control of the catalyst diameter (and thus the CNTs) and to ensure the continuous growth of CNTs from the catalysts on the bead's surface [17]. The CNTs were then separated from the beads by vigorously fluidizing the bed with Ar gas at 20 slm for 10 min (Figure 3-1c). The residual carbon on the beads was removed by oxidizing with 20 vol% O₂/Ar at 5 slm for 5 min. The cycle was then moved to the redeposition process. Note that the AlO_x support layer was deposited every cycle to cover the coarsened Fe particles and have fresh Fe particles to maintain the small diameter of the catalyst particles and CNTs for further cycles [17]. These processes were repeated at a constant bed temperature of 745 °C by changing the gas flow to minimize the time and energy consumed for cooling/heating the bed [17]. Al₂O₃ beads with a relatively large diameter of 0.5 mm were used to keep the beads in the reactor tube under a high gas flow for growth and separation of CNTs. For such big beads, the minimal fluidization velocity is about 0.1 m s⁻¹ [17]. We kept the flow rates and thus the gas velocities high enough for all steps of catalyst deposition (20 slm total flow rate and 1.0 m s⁻¹ gas velocity), catalyst reduction (9.48 slm and 0.47 m s⁻¹), CNT growth (9.48 slm and 0.47 m s⁻¹), CNT separation (20 slm and 1.0 m s⁻¹), and oxidation of the residual carbon (5 slm and 0.25 m s⁻¹), resulting in a slugging fluidized bed (ambient pressure for all steps).

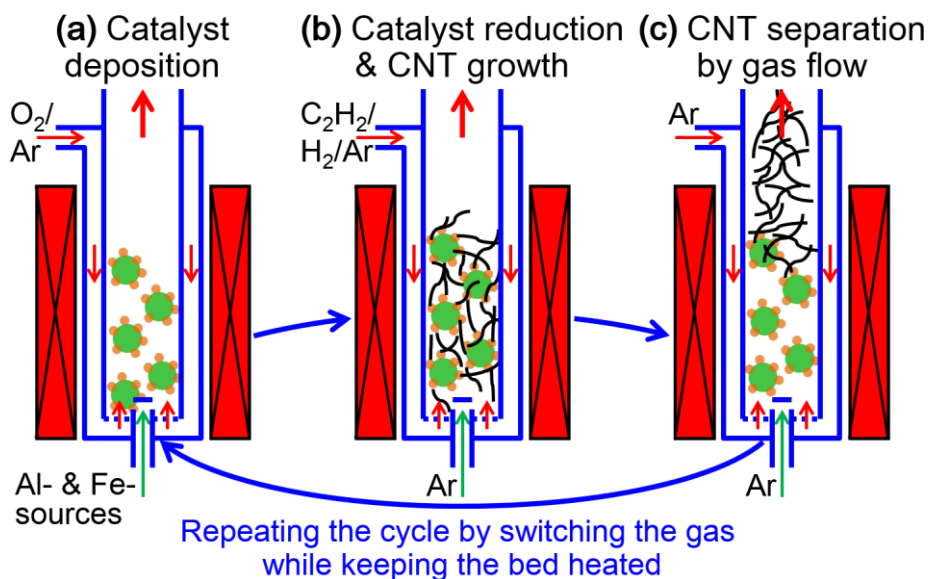


Figure 3-1. Schematic of the semi-continuous fluidized-bed process: (a) deposition of AlO_x support layer from aluminum-isopropoxide followed by deposition of Fe catalyst particles from ferrocene; (b) reduction of Fe catalyst by introducing H_2 followed by CNT growth by feeding C_2H_2 ; and (c) separation of CNTs from beads by increasing Ar gas flow. After removing the residual carbon on the beads by introducing O_2 , the next cycle is carried out starting at step (a). The whole process can be repeated by just changing the gas flow while keeping the bed heated at a fixed temperature for tens of cycles without changing the beads.

The synthesized CNT samples were characterized by field emission SEM (S-4800, Hitachi, Japan). Some VA-CNTs were transferred from the beads to copper microgrids using tweezers and observed via TEM (JEOL 2000EX, Japan). The CNT powders after separation were characterized by TG-DTA with a ramp rate of $5\text{ }^\circ\text{C}/\text{min}$ in air (TG8120, Rigaku, Japan). The BET surface areas of the CNT samples were determined by N_2 (77 K) volumetric adsorption (Quantachrome Instruments Autosorb 1C, FL, USA) after pre-evacuation at 423 K and 10^{-4} Pa for 2 h. The CNT paper made by dispersion in ethanol and vacuum filtration was analyzed by X-ray fluorescence spectroscopy (XRF, ZSX Primus 2, Rigaku, Japan) to determine its elemental composition. The nominal thickness of the deposited Fe on the beads

and the composition of the ash of the CNTs after the TG-DTA measurement were analyzed using an energy dispersive X-ray spectrometer (EDS, EDAX Genesis) coupled with SEM. The catalyst deposited on the bead surface was analyzed by atomic force microscopy (AFM; SPM 9600; Shimadzu, Kyoto, Japan). The composition of the effluent gas from the FBCVD reactor was measured using a GC (GC-2014, Shimadzu, Japan) equipped with a FID.

3.3 Heating state of the bed in the reactor with an internal heat-exchange and preheating zone

We first investigated and compared the heating states of the bead bed (30 mm static height) using the old single tube (22 mm in inner diameter, Figure 3-2a) and the new coaxial double tube (40 mm in inner diameter for the bed, Figure 3-2b) using the same furnace (300 mm in length, the distributor set at 32 mm from the furnace bottom, and the thermocouple for furnace control set outside of the reactor tube at 150 mm from the furnace bottom) with the same set temperature of 820 °C and various Ar flow rates. As with the old singular reactor tube (Figure 3-2a), the top region of the bed was heated well to 830 °C at 140 mm from the distributor, but the bottom of the bed was insufficiently heated (690 °C) for an Ar flow rate of 3.16 slm. The temperature of the distributor of the reactor tube decreased to 630 °C with an Ar flow rate of 10 slm. Although fluidized beds are known to effectively enhance mass and heat transport, rapid gas feed with a residence time ≤ 0.3 s causes insufficient heating. Such insufficient heating becomes more serious for larger reactor tubes. In contrast, for the new reactor tube with two feed lines (Figure 3-2b), one line from the bottom directly to the bed for catalyst vapors and the other line for the other gases from the top through the heat-exchange and preheating zone and the distributor at the bottom, the temperature was more uniform. For

the low total gas feed rate of 5 slm, the temperature at the distributor of the reactor tube was 750 °C because 1 slm Ar gas was directly fed into the bed from the catalyst line without preheating. With the increase in the total gas feed, the effect of the cold Ar gas decreased, the temperature became more uniform, and the temperature at the bottom of the reactor tube increased, reaching 780 °C at a high Ar gas feed rate of 30 slm (corresponding to a space velocity as high as 3600 h⁻¹). It should be noted that this more uniform heating was achieved for a reactor tube with a larger diameter (40 mm) than the old reactor tube (22 mm).

We also did computational fluid dynamics simulation using the Fluent software for both the old and new reactor tubes to compare the heating state of them with different gas flow rates. The simulation was done just with Ar gas feed without beads and the set temperature is 820 °C. In Supporting Information, Figure S2, we can find that the temperature profile changed a lot with the gas flow rate increase, which agrees with the measured temperature profile in Figure 3-1a. We can notice that the condition is quite opposite to the new tube, the temperature profile keeps constant with the increase in the gas flow rate and agrees with the measured temperature profile in Figure 3-1b. The uniform heating even with the cold catalyst line gas will realize the efficient control of CNT growth by FBCVD with minimal catalyst stuck in the feed line. In addition, improved heating for the increased gas feed rate suggests good compatibility with scale-up. Furthermore, the heat-exchange zone will enable the reduction of the heating power consumption by heating the cold inlet gas with the hot effluent gas.

Next, I discuss the effect of the reactor diameter on the heat transfer efficiencies for the conventional single tube reactor and the new coaxial double tube reactor. Equation (1) is for the heat flow Q for a fluid with a heat transfer area A , thermal conductivity k , temperature difference between the reactor wall and the fluid ΔT , and the boundary film thickness δ .

Figure S3 shows the relationships between A , δ , and the inner diameter of the reactor tube d for each factor. In case of the conventional single tube reactor (old tube), $\delta \propto d$. Thus, according to equation (1), $Q \propto d^0$. Whereas, the gas flow rate $F \propto d^2$ and thus the heat needed to heat the gas increase with d^2 . With the diameter increase by 10 times, the heat needed to be transferred increases by 100 times whereas the heat flow remains unchanged. Thus it results in the insufficient heating of the gas upon scale up. On the other hand, in case of the new coaxial double tube, δ can be kept constant for increasing d . According to equation (1), $Q \propto d$. With the diameter increase by 10 times, the heat needed to be transferred increases by 100 times whereas the heat flow increases by 10 times. Therefore, the new coaxial double tube is more compatible with scale-up compared with the old single tube (conventional reactor). These results are consistent with the temperature profiles of both reactor tubes in Figure 3-2 and Figure S1.

$$Q = Ak\Delta T/\delta \quad \dots\dots\dots \quad \text{Equation (1)}$$

For laboratory experiments, keeping the bed at the setting temperature is crucially important to carefully control the catalyst particle size and the resulting CNT diameter. Thus we used this reactor as a convenient and effective means. For the practical aspect, because the reaction temperature is as high as 745 °C, the connection between preheater or heat exchanger with reactor is not so easy. In addition, we have to carry such hot gas within sub-seconds to avoid the gas-phase non-catalytic pyrolysis. Therefore, this configuration would be useful also for the practical CNT production.

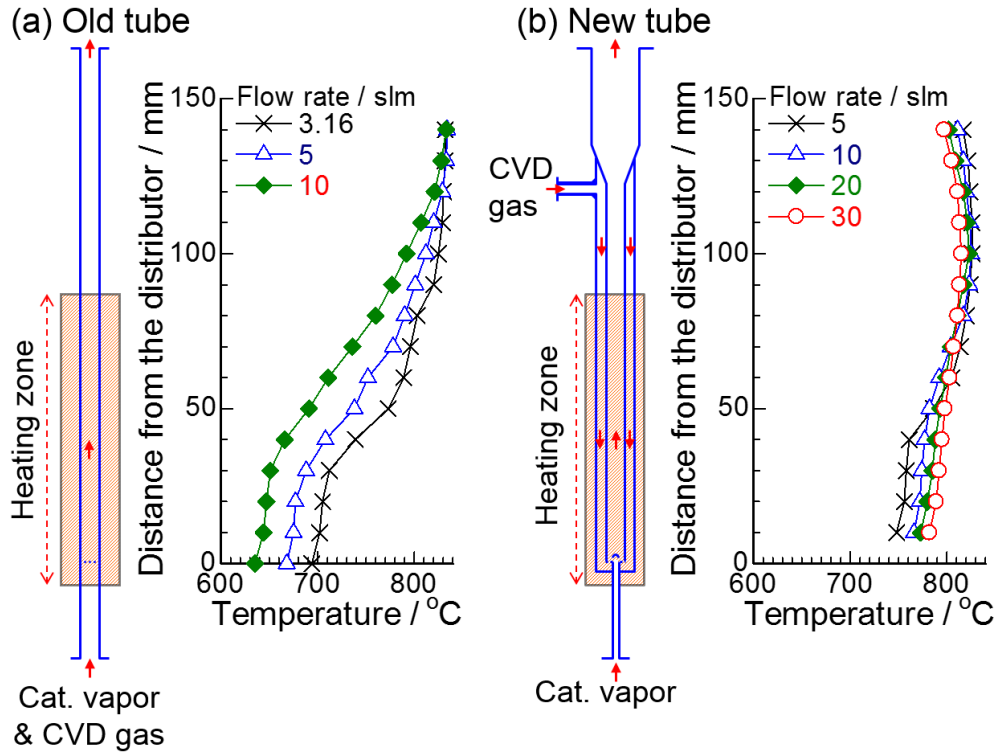


Figure 3-2. Schematics of (a) the old single tube and (b) the new coaxial double tube with temperature distributions for various Ar gas feeds. In (a), Ar gas was fed at 3.16–10 slm to the bed through the distributor at the bottom. In (b), Ar gas was fed through two inlets: constantly from the catalyst line at the bottom at 1 slm and from the top through the heat-exchange and preheating zone and the distributor at the bottom at 4–29 slm. The inner tube diameter for the bed was 22 mm for (a) and 40 mm for (b), and the set temperature was 820 °C for both (a) and (b).

3.4 Semi-continuous production of CNTs and the resulting CNT structure

Photos of the fluidized-bed reactor were taken at ambient temperature without gas flow at each step by interrupting the semi-continuous operation (Figure 3-3). 82 g of pristine Al_2O_3 beads initially had a bed height of 3 cm (Figure 3-3a). After depositing the Fe/AlO_x catalyst on the beads and reducing them with H_2 , CVD was carried out for 20 min. The bead bed remarkably increased in height (by more than four times) from 3 to 13 cm owing to the sub-

millimeter-long CNT arrays grown on the bead surfaces (Figure 3-3b). These CNT arrays were easily separated from the beads by vigorously fluidizing the beads with an increased Ar carrier gas flow and 0.82 g of CNTs, which corresponds to a carbon yield of 37% (note that 2.23 g carbon was fed as 1.1 vol% C_2H_2 in 20 min), were collected in a 0.5 L bottle (Figure 3-3d). The bead bed height decreased from 13 to around 3 cm (Figure 3-3c), indicating efficient separation of CNTs from the beads. Then, the residual carbon on the beads was removed by oxidation with O_2/Ar for 5 min.

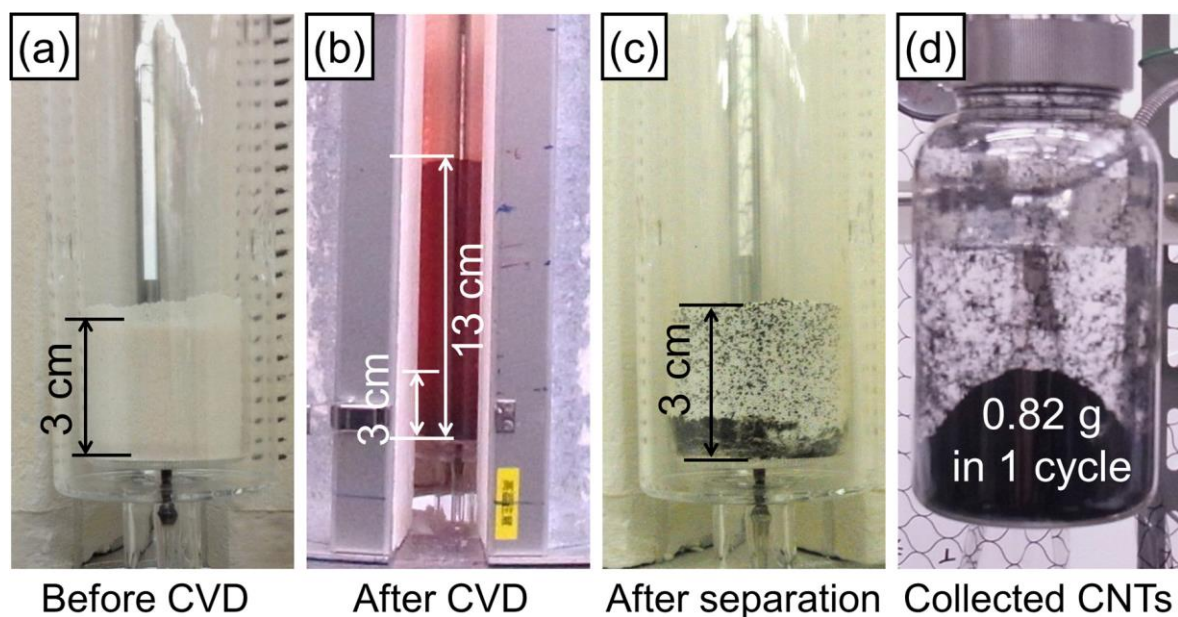


Figure 3-3. Photos of the fluidized-bed reactor taken by stopping the gas flow and interrupting the cycle at each step of the semi-continuous operation: (a) the bed with pristine beads before CVD; (b) the bead bed after CVD; (c) the bead bed after CNT separation; and (d) CNTs collected in a 0.5 L container in one cycle. All steps were simply performed by gas flow modulation at a fixed set temperature of 745 °C in a single fluidized-bed reactor.

Figure 3-4a and b show the SEM images of the CNT arrays collected in the container (Figure 3-3d). The CNTs were 0.3–0.4 mm long and appeared well-aligned (Figure 3-4a). Note that CVD was carried out with a lower gas flow rate of 9.48 slm than for CNT separation (~20 slm) so that CNTs could continuously grow without separation during CVD. However, in the enlarged image in Figure 3-4b, the CNT array had rather poor alignment, which is sometimes observed for VA-CNT arrays. Figure 3-4d–f shows the TEM images of the CNTs taken near the top (Figure 3-4d), middle (Figure 3-4e), and bottom (Figure 3-4f) of a single piece of the CNTs taken out of the array. The inset histograms of the CNT diameter distributions show that the diameter increased with increasing depth. Figure 4c shows the average diameter of the CNTs at different depths from the top of the VA-CNTs. The diameter increased from 9.9 to 12.5 nm with an average diameter of 11 nm. Because CNTs grow in root growth mode, this result indicates that the diameter of the CNTs increases with time because of gradual coarsening of the catalyst particles during CVD, which is in good agreement with the diameter increase in growing SWCNTs during rapid growth on flat substrates by CVD [22,23,28,29]. Therefore, we have achieved the semi-continuous production of sub-millimeter-long CNTs using the new reactor tube with a larger cross-section than our previous method. However, the resulting CNTs had a rather disordered structure with a large diameter. Next, we carried out the experiment with careful control of the catalyst and CVD conditions. The N₂ adsorption measurement (Figure 3-5) for CNT powders at 77 K showed that the CNTs had a BET surface area of 367 m² g⁻¹ based on the BET plot.

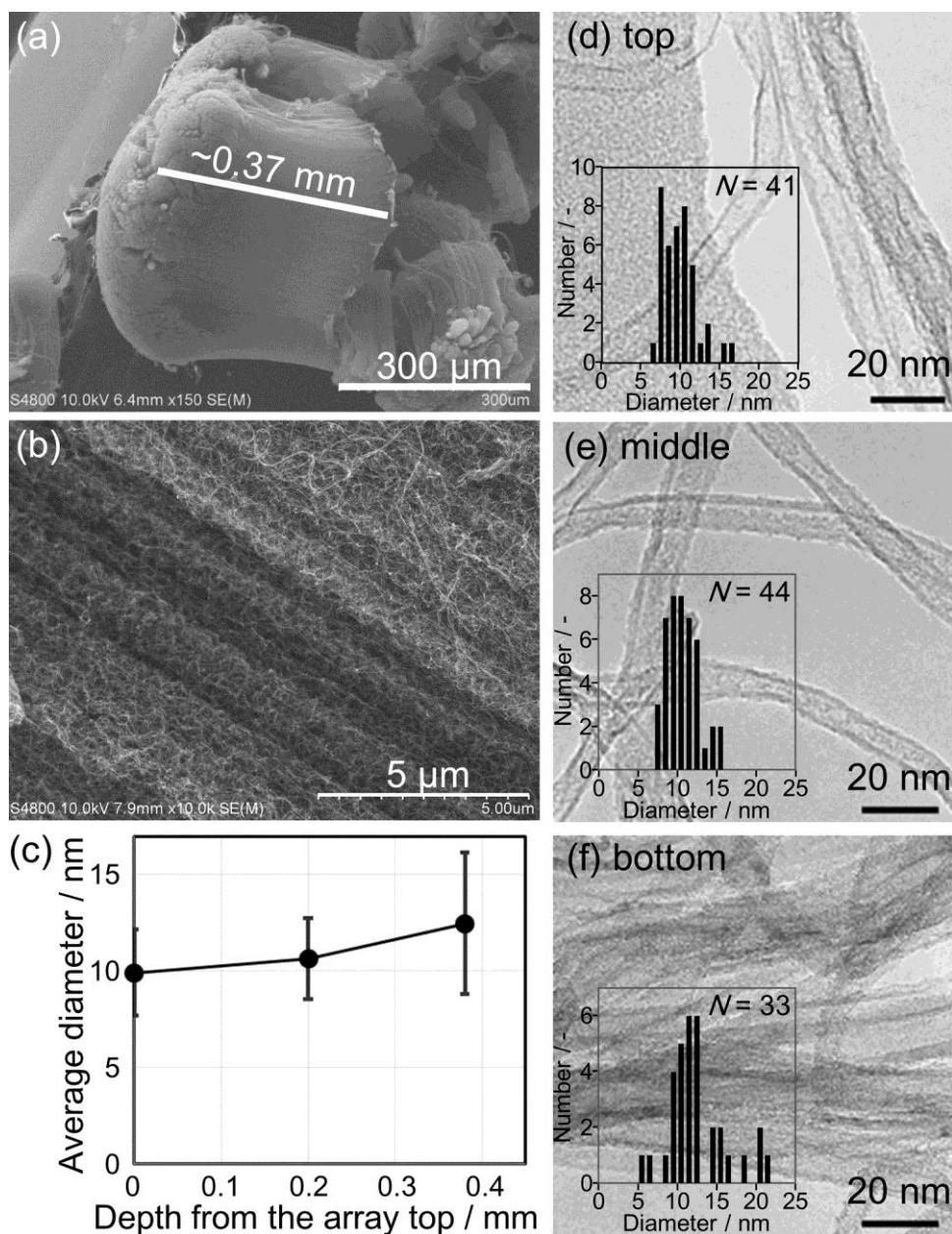


Figure 3-4. (a, b) SEM images of the CNTs separated from the beads by the gas flow and collected in the container bottle. (c) The change in the average diameter of the CNTs plotted against the depth from the top of the CNT arrays. The error bars show the standard deviation. (d–f) TEM images and diameter distributions of CNTs at the top, middle, and bottom of a single piece of the CNTs taken out from the array, respectively.

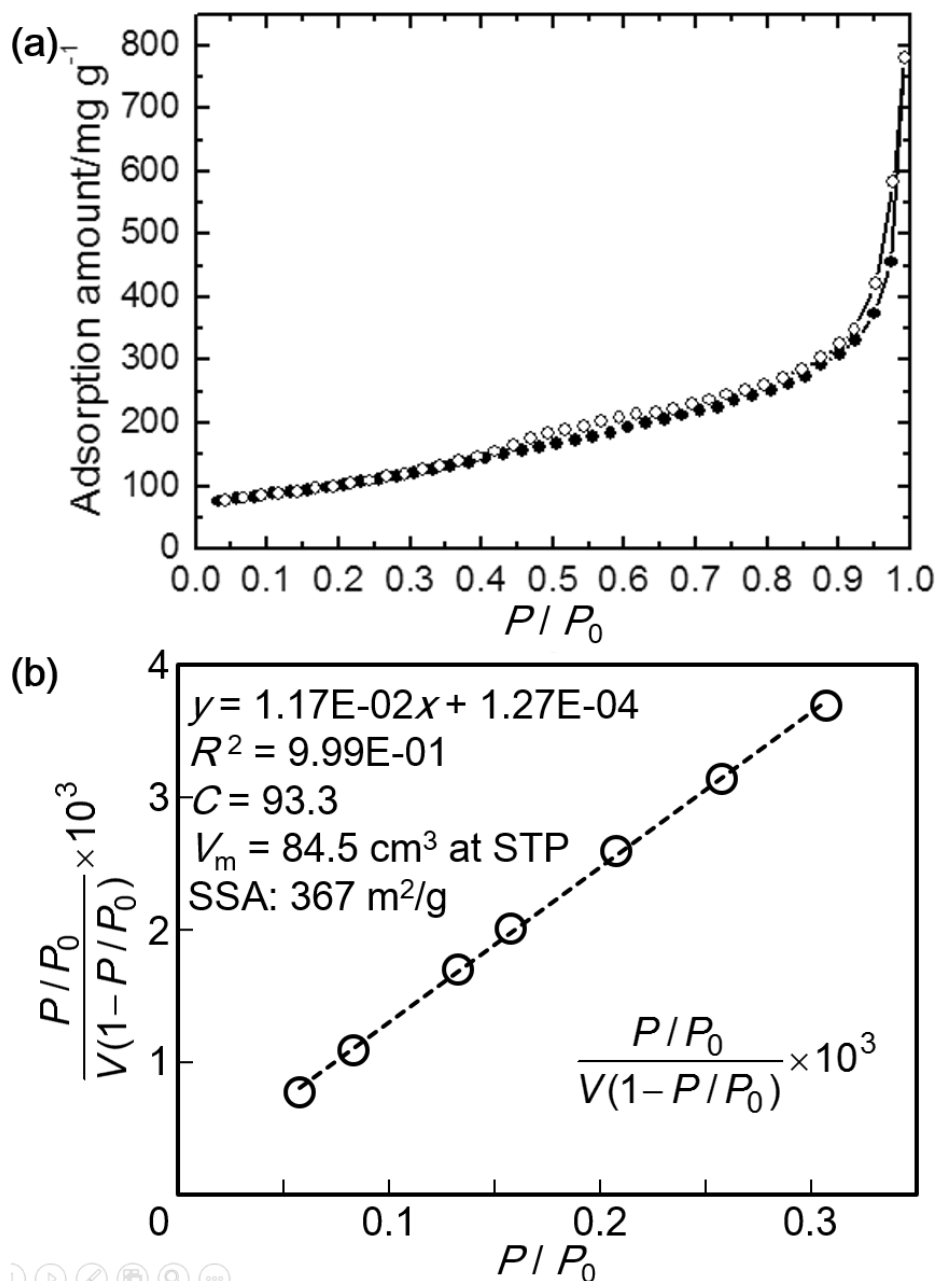


Figure 3-5. (a) N₂ adsorption isotherm at 77 K and (b) corresponding BET plot of the sub-millimeter-long CNTs. CNTs were separated from the beads by vigorous fluidization. The closed and open symbols in (a) indicate adsorption and desorption processes, respectively.

Figure 3-6a showed that the CNTs had a carbon purity of 97.2 wt.%, with a small content of amorphous carbon of 2 wt.%, and an oxidation stability of about 660 °C. We

analyzed the compositions of the ash after TG-DTA by EDX (Figure 3-6b) The ash contained Fe and Al, which are attributed to the Fe catalyst and AlO_x support layer being scraped off during the vigorous fluidization for CNT separation. The small Si content should be attributed to the reactor tube made of quartz glass being scraped off slightly. The weight of ash was 0.25 mg, which is in good agreement with carbon purity of 97.2 wt.% in the 9.7 mg CNTs used for the TG-DTA measurement.

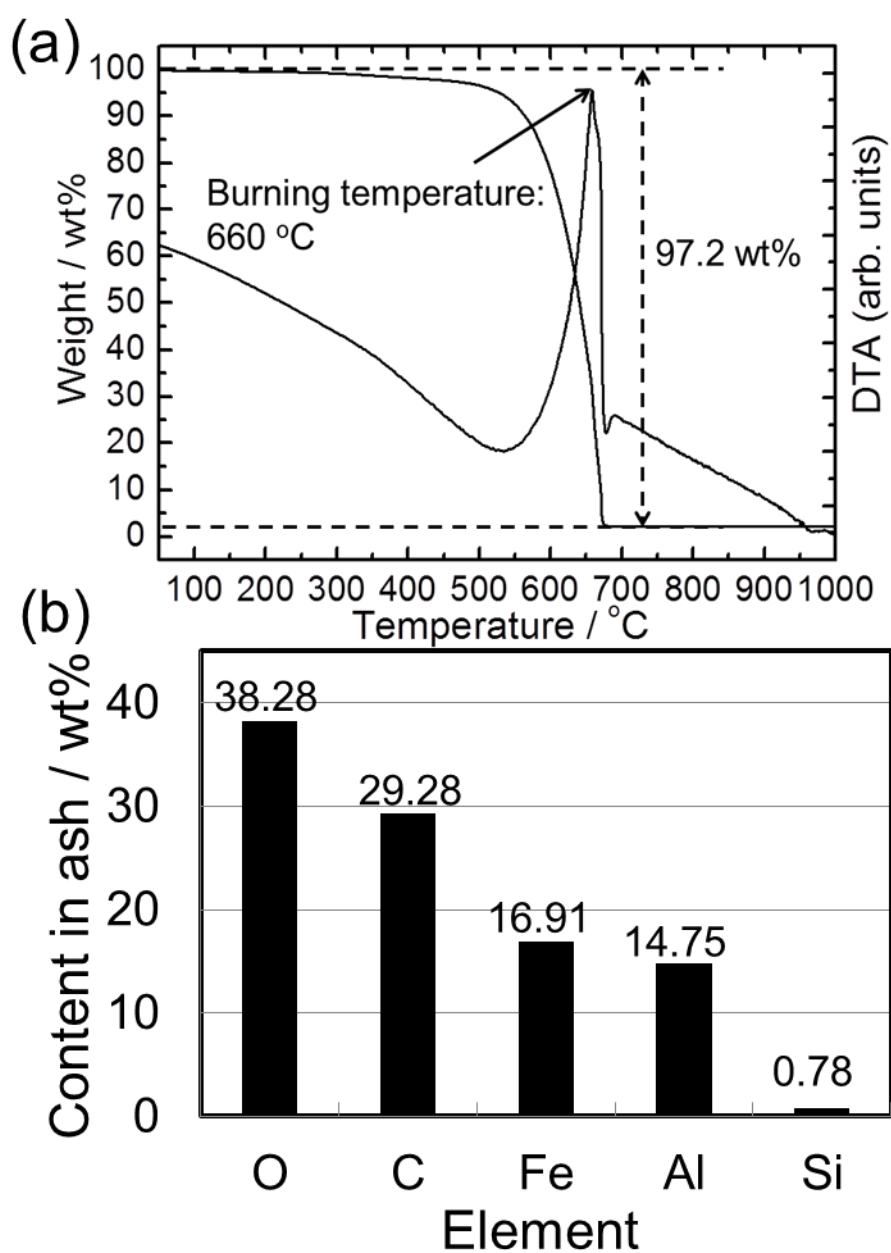


Figure 3-6. TG-DTA curves of the CNTs (sample weight of 9.7 mg) synthesized by FBCVD and separated from the beads by vigorous fluidization. (b) Elemental composition of the ash after the TG-DTA measurement.

We analyzed the composition of the carbon-containing species in the effluent gas from the FBCVD reactor by GC-FID at 2 min interval during 20 min CVD (Figure 3-7). We first supplied the CVD gas to the tube filled with pristine beads at room temperature (r. t.) to eliminate the influence of the catalytic reaction, and used the data as the reference. For the effluent gas during CVD, CH₄, C₂H₂, CO₂ and C₂H₄ were the main carbon containing species. Small peaks for C₂H₆ and CO were also detected. There were two stages for CNT growth. One is the early stage from 0 to 6 min, where the conversion of C₂H₂ to undetectable carbon (mostly CNTs) was as high as 70–80%. The other is the later stage from 8 to 20 min, where the catalyst gradually deactivated and the conversion decreased to 70–40%. The total conversion was around 60%. From this graph, we find that a certain fraction of catalyst has a lifetime longer than 10 min.

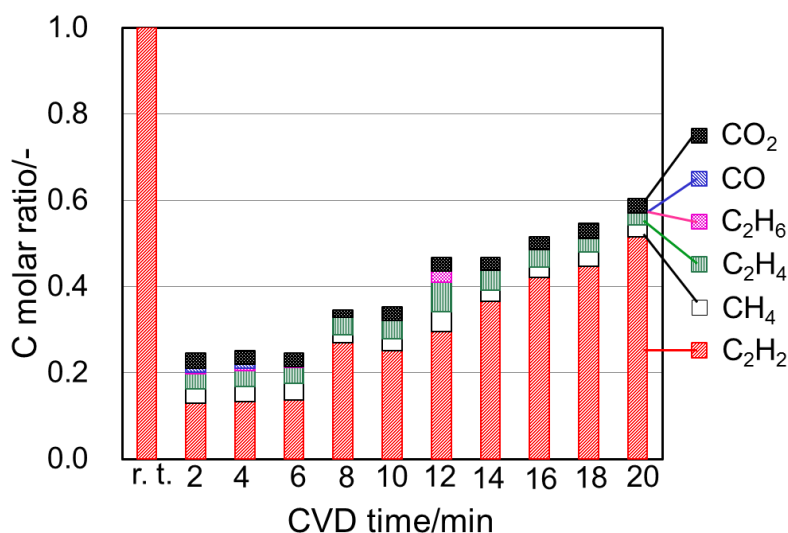


Figure 3-7. Composition of the effluent gas from the FBCVD reactor for different CVD times analyzed by GC-FID.

3.5 Conclusions

Aiming at efficient synthesis of CNTs at low cost with controlled structure to put them for practical application, we designed and developed a new heat-exchange reactor for FBCVD. The sufficient heating of reaction gas and large reaction area provided the bead bed realized the synthesis of CNTs with an increased scale. Internal heat-exchange reactor enabled semi-continuous production of submillimeter-long CNTs with an increased reactor volume of ~ 0.5 L, and will enable further scale-up as predicted by the computational fluid dynamics simulation. But some problem arose in the resulting CNT structure, that is, FWCNTs proved to have an increased average diameter of 11 nm and a reduced carbon purity of 97.2 wt%. Careful control over the catalyst and CVD conditions are needed for improvements both in quantity and quality of CNTs, which is made in the next chapter.

References

- [1] A. L. M. Reddy, M. M. Shaijumon, S. R. Gowda, P. M. Ajayan, *Nano Lett.* 9 (2009) 1002.
- [2] Y. Jiang, P. Wang, X. Zang, Y. Yang, A. Kozinda, L. Lin, *Nano Lett.* 13 (2013) 3524.
- [3] A. B. Phillips, R. R. Khanal, Z. Song, R. M. Zartman, J. L. DeWitt, J. M. Stone, P. J. Roland, V. V. Plotnikov, C. W. Carter, J. M. Stayancho, R. J. Ellingson, A. D. Compaan, M. J. Heben, *Nano Lett.* 13 (2013) 5224.
- [4] Y. Zou, Q. Li, J. Liu, Y. Jin, Q. Qian, K. Jiang, S. S. Fan, *Adv. Mater.* 25 (2013) 6050.
- [5] K. Fu, O. Yildiz, H. Bhanushali, Y. Wang, K. Stano, L. Xue, X. Zhang, P. D. Bradford, *Adv. Mater.* 25 (2013) 5109.
- [6] B. You, N. Li, H. Zhu, X. Zhu, J. Yang, *ChemSusChem* 6 (2013) 474.
- [7] S. J. Tans, M. H. Devoret, H. Dai, A. Thess, R. E. Smalley, L. J. Geerligs, C. Dekker, *Nature* 386 (1997) 474.
- [8] A. Javey, J. Guo, Q. Wang, M. Lundstrom, H. Dai, *Nature* 424 (2003) 654.
- [9] A. Thess, R. Lee, P. Nikolaev, H. Dai, P. Petit, J. Robert, C. Xu, Y. H. Lee, S. G. Kim, A. G. Rinzler, D. T. Colbert, G. E. Scuseria, D. Tomanek, J. E. Fischer, R. E. Smalley, *Science* 273 (1996) 273.
- [10] P. Nikolaev, M. J. Bronikowski, R. K. Bradley, F. Rohmund, D. T. Colbert, K. A. Smith, R. E. Smalley, *Chem. Phys. Lett.* 313 (1999) 91.
- [11] H. J. Jeong, K. K. Kim, S. Y. Jeong, M. H. Park, C. W. Yang, Y. H. Lee, *J. Phys. Chem. B* 108 (2004) 17695.

-
- [12] M. Endo, H. Muramatsu, T. Hayashi, Y. A. Kim, M. Terrones, M. S. Dresselhaus. *Nature* 433 (2005) 476.
- [13] S. Hofmann, C. Ducati, J. Robertson, B. Kleinsorge. *Appl. Phys. Lett.* 83 (2003) 135.
- [14] R. Philippe, A. Morançaïs, M. Corrias, B. Caussat, Y. Kihn, P. Kalck, D. Plee, P. Gaillard, D. Bernard, P. Serp1, *Chem. Vap. Deposition* 13 (2007) 447.
- [15] C. H. See, A. T. Harris, *Ind. Eng. Chem. Res.* 46 (2007) 997.
- [16] Q. Zhang, M. Zhao, J. Huang, J. Nie, F. Wei. *Carbon* 48 (2010) 1196.
- [17] D. Y. Kim, H. Sugime, K. Hasegawa, T. Osawa, S. Noda, *Carbon* 49 (2011) 1972.
- [18] W. Z. Li, S. S. Xie, L. X. Qian, B. H. Chang, B. S. Zou, W. Y. Zhou, R. A. Zhao, G. Wang, *Science* 274 (1996) 1701.
- [19] K. Hata, D. N. Futaba, K. Mizuno, T. Namai, M. Yumura, S. Iijima, *Science* 306 (2004) 1362.
- [20] S. Noda, K. Hasegawa, H. Sugime, K. Kakehi, Z. Zhang, S. Maruyama, Y. Yamaguchi, *Jpn. J. Appl. Phys.* 46 (2007) 399.
- [21] H. Sugime, S. Noda, *Carbon* 48 (2010) 2203.
- [22] K. Hasegawa, S. Noda, *ACS Nano* 5 (2011) 975.
- [23] Z. Chen, D. Y. Kim, K. Hasegawa, S. Noda, *ACS Nano* 7 (2013) 6719.
- [24] R. Xiang, G. Luo, W. Qian, Y. Wang, F. Wei, Q. Li, *Chem. Vap. Deposition* 13 (2007) 533.
- [25] Q. Zhang, J. Huang, M. Zhao, W. Qian, Y. Wang, F. Wei, *Carbon* 46 (2008) 1152.

-
- [26] R. Xiang, G. Luo, Z. Yang, Q. Zhang, W. Qian, F. Wei, *Mater. Lett.* 63 (2009) 84.
- [27] Q. Zhang, M. Zhao, J. Huang, Y. Liu, Y. Wang, W. Qian, F. Wei, *Carbon* 47 (2009) 2600.
- [28] K. Hasegawa, S. Noda, *Appl. Phys. Express* 3 (2010) 045103.
- [29] K. Hasegawa, S. Noda, *Carbon* 49 (2011) 4497.

Chapter 4 - Semi-continuous production of CNTs with smaller diameter using an internal heat-exchange reactor

(Part of this chapter has been published in: Zhongming Chen, et al., Carbon, 2014.)

4.1 Introduction

CVD method, which offers a versatile control and possibility of scale-up, is the most promising method of producing CNTs with controlled structure [1-6]. In order to produce CNTs with high productivity and desired atomic structures, lots of efforts have been made toward uncovering the mechanism of CNT growth in CVD process [7-11]. The unique properties of CNTs are closely linked to their structural parameters. Their diameter and number of walls belong to such parameters, which can affect their flexibility and conductivity. With the goal of putting CNTs in practical application, precise control of the diameter of produced CNTs is therefore a goal of this thesis. In most CVD processes, one catalyst particle nucleates one CNT. In consequence, the diameter of the CNT is closely related to the size of the catalyst particle. With this basic knowledge, many researchers try to grow CNTs with smaller diameter and/or narrow diameter distribution by using smaller and/or identical catalyst particles [11-15]. Cheung et al. reported that by controlling the catalyst particle size, the diameter of CNTs could be controlled [16]. Lu et al. further proposed that there exists a unified theory on the relationship between nanoparticle size, growth condition, growth temperature, and diameter of the resulting CNTs. The key parameter for the proposed relationship is the carbon feed rate at the growth step in a CVD process [17].

We previously developed the “combinatorial masked deposition” (CMD) method and applied this method to screening and optimization of the catalyst conditions for SWCNT growth [18-22]. Using the combinatorial catalyst libraries coupled with real-time monitoring of SWCNT growth, the catalyst and CVD conditions were systematically studied. The keys for this growth are to maintain the C_2H_2 pressure below its upper limit to prevent the killing of the catalysts and to grow the SWCNTs before the catalyst particles lose their activity because of coarsening through Ostwald ripening. Control of the catalyst particle size is crucially important to control the diameter of CNTs. Because the catalyst particle size can be controlled by the nominal thickness of the catalyst layer to a large extent [22,23], we changed the Ar carrier volume for ferrocene and examined the structure of resulting Fe particles by AFM. By reducing the feed of the catalyst vapor and the catalyst particle size, and by reducing the C_2H_2 feed and preventing the deactivation of small catalyst particles, we realized the semi-continuous production of 99.6–99.8 wt%-pure, 0.2-mm-long FWCNTs with an average diameter of 6.5 nm with a carbon yield of 42% and the gas-residence time of 0.3 s.

4.2 Methods

The methods are described in Chapter 3. Typically, all processes for catalyst (re-)deposition, catalyst reduction, CNT growth, CNT separation, and removal of residual carbons were performed in a single FBCVD reactor of coaxial double tube. All the gases except for the catalyst vapor were fed to the outer tube, flown down and preheated by the furnace and the hot effluent gas in the inner tube, and then flown into the inner tube through the distributor at the bottom. In Chapter 3, we realized the synthesis of CNTs with a large diameter ~11 nm. We tried to produce CNTs with smaller diameters by reducing catalyst

source for smaller catalyst particles and reducing carbon feed not to deactivate such catalyst particles. Firstly, total Ar carrier for ferrocene was changed from 50 to 250 standard cm³ with the same Ar carrier volume for aluminium isopropoxide supply. CVD was carried out with the same condition as before with CVD times of 10 and 20 min. Hereafter, with Ar carrier for ferrocene of 50 and 250 standard cm³, CVD was performed by flowing 0.73 vol% and 0.37 vol% C₂H₂/ 26 vol% H₂/ 600 ppmv H₂O/ Ar at 9.48 slm for 10 and 20 min, respectively. The same analytical method as in Chapter 3 is applied to the resulting CNTs.

4.3 Controlling the amount and size of Fe particles

Figure 4-1a shows the nominal thickness of Fe deposited on the AlO_x layer on the Al₂O₃ beads, measured by SEM-EDS. To determine the average value for different beads, three different points were measured for each bead and five beads were measured for each condition. The nominal Fe thickness was 1.77 nm with 250 standard cm³ Ar used to carry ferrocene, and it decreased linearly with the Ar carrier volume to 0.28 nm with 50 standard cm³ Ar for ferrocene. Figure 4-1b–d shows the AFM images of the Al₂O₃ bead surface with (b) AlO_x support layer and (c,d) Fe catalyst particles on AlO_x support layer. The AlO_x support layer had roughness with in-plane size of several tens nanometers (Figure 4-1b). Ferrocene carried by 250 standard cm³ Ar formed Fe particles of around 20–40 nm in diameter (Figure 4-1c), and that carried by 50 standard cm³ Ar formed smaller Fe particles of around 10–20 nm in diameter (Figure 4-1d). The nominal Fe thickness was in a similar range with the sputtered catalyst for millimeter-tall SWCNTs on flat substrates (0.5–1.0 nm, typically) [18,21,24], however the number density of Fe particles was about one-order smaller (10^{10–11} cm⁻²) than the sputtered catalyst (typically ~1×10¹² cm⁻² [21]). The difference possibly arises from the

different reactivity of depositing Fe species; Fe atoms by sputtering attach to both the AlO_x support layer and the nucleated Fe particles whereas ferrocene may preferentially attaches to the nucleated Fe particles, resulting in the larger Fe particles with smaller number density.

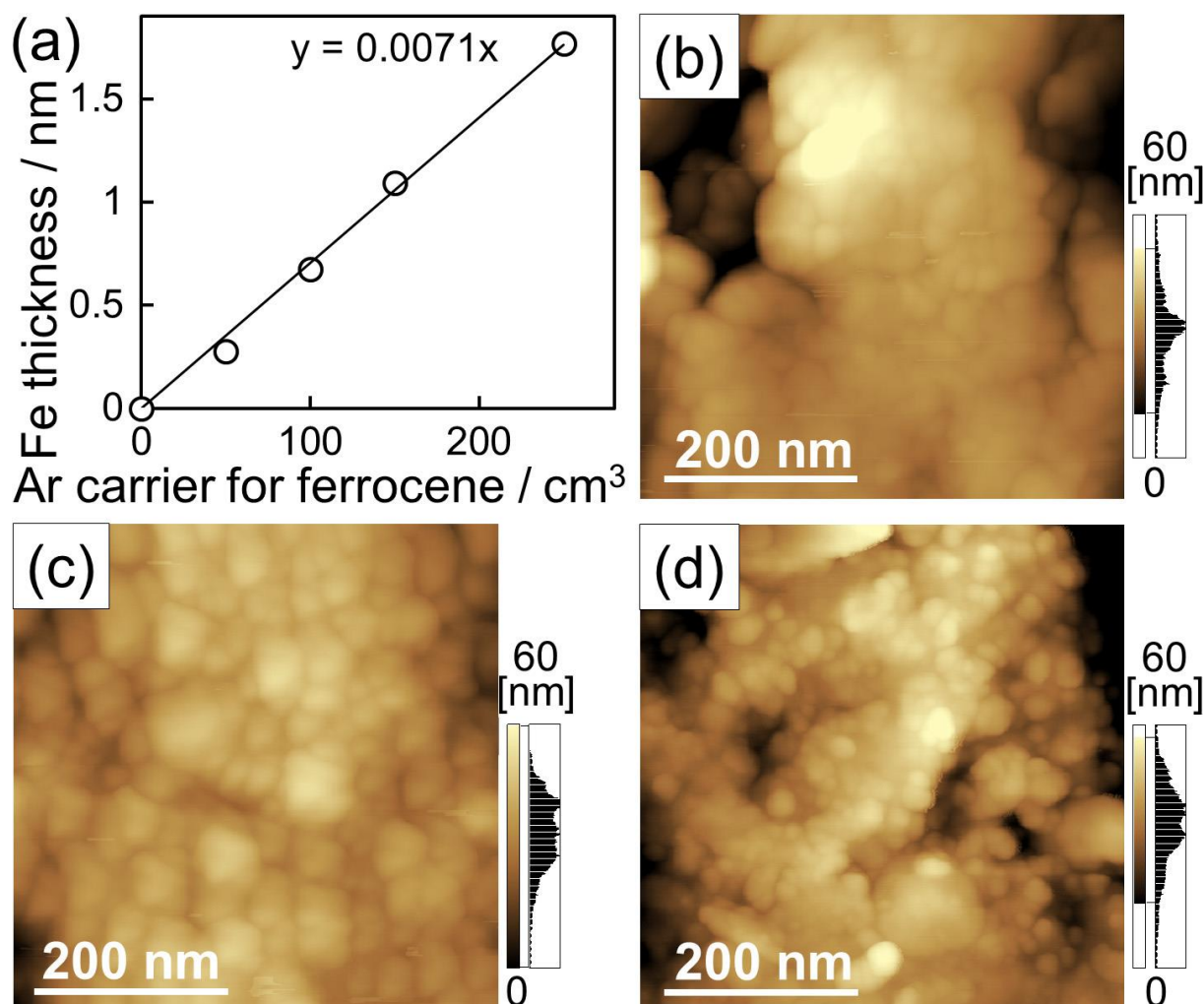


Figure 4-1. (a) Relationship between the nominal Fe thickness and the Ar carrier gas volume for ferrocene. AFM images of the alumina bead surface with different catalyst layers: (b) AlO_x , (c) 1.77 nm Fe on AlO_x , and (d) 0.28 nm Fe in AlO_x . The AlO_x layer was deposited by carrying aluminum isopropoxide using 450 standard cm^3 Ar gas in all cases. The Fe catalyst was deposited on the AlO_x layer by carrying ferrocene using (c) 250 and (d) 50 standard cm^3 Ar gas and reduced with 26 vol% H_2 /0.06 vol% H_2O /Ar at 9.48 slm for 10 min.

4.4 Effects of catalyst feed on the production amount of CNTs

By using these catalysts, we next synthesized CNTs by FBCVD under the same condition as for Figures 3-3 and 3-4 (i.e., 1.1 vol% C_2H_2 / 26 vol% H_2 / 0.06 vol% H_2O / Ar at 9.48 slm and 745 °C). Figure 4-2 shows the SEM images, array lengths, and weight of the CNT arrays collected in the container bottle. From the SEM images, we can see that all the CNTs are aligned and sub-millimeter long, even after vigorous fluidization for separation. Array lengths were longer for larger Ar carrier volume for ferrocene (i.e. larger Fe particles with larger nominal Fe thickness, Figure 4-1), and for longer CVD time of 20 min (Figure 4-2k). The weight of CNTs collected in a container bottle was 0.4–0.5 g per cycle for 10 min CVD and similar for different Fe feeds. Whereas the weight of CNTs increased from 0.45 to 0.81 g per cycle for larger Fe catalyst feeds for 20 min CVD. The big Fe catalyst particles, formed with 250 standard cm^3 Ar carrier for ferrocene (Figure 4-1c), yielded CNTs at increasing amount from 0.52 g in 10 min to 0.81 g in 20 min, meaning that such catalyst remained active for 20 min. Whereas the small Fe catalyst particles, formed with 50 standard cm^3 Ar carrier for ferrocene (Figure 4-1d), yielded CNTs at similar amounts of 0.40 g in 10 min and 0.45 g in 20 min, meaning that such catalyst was mostly deactivated in 10 min. To produce CNTs with smaller diameter at a high yield, it is essential to find the condition that keeps small Fe particles active for long CVD time.

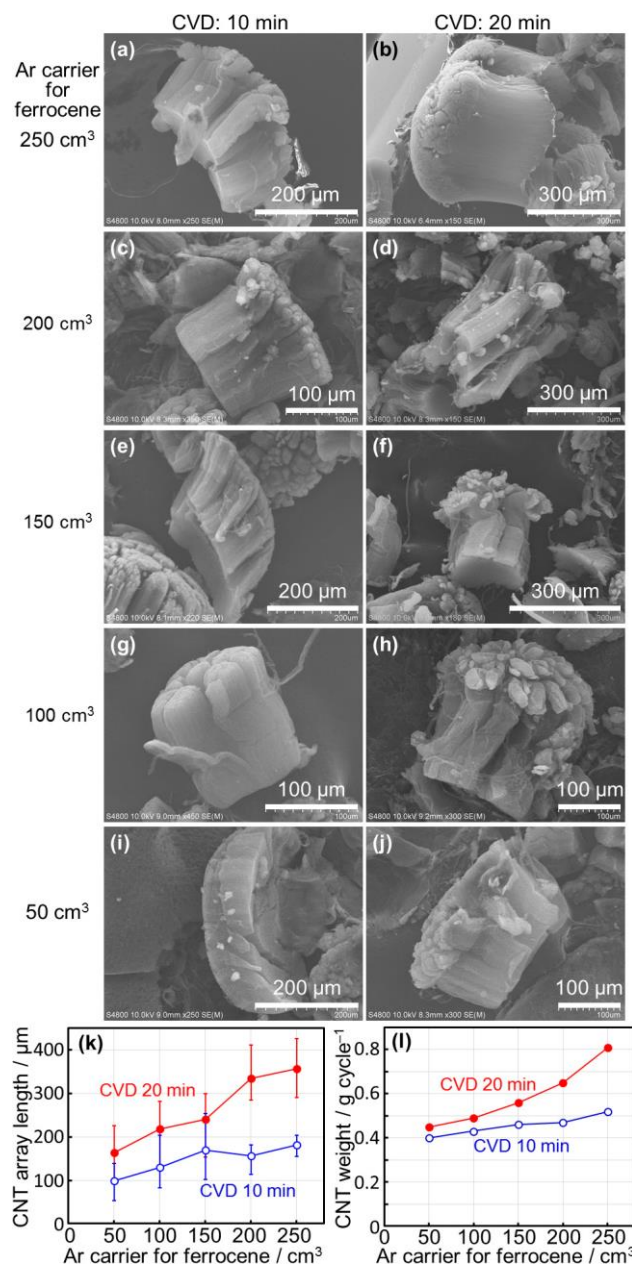


Figure 4-2. (a–j) SEM images, (k) array lengths, and (l) weight of CNT arrays collected in the container bottle. The Ar carrier gas for ferrocene was varied between 50 and 250 standard cm³, and CVD was carried out under the same conditions as Figures 3-3 and 3-4, using 1.1 vol% C₂H₂ for either 10 or 20 min. The array lengths were measured for 10 arrays of each sample and the average value is plotted in (k) with the maximum and minimum values as error bars. The weight of CNTs collected in one cycle of ~1 h is shown in (l).

4.5 Keeping small catalyst particles active by moderating C_2H_2 feed and yielding sub-millimeter-long FWCNTs with reduced diameter and improved purity

As we have previously reported, smaller catalyst particles are more easily deactivated by C_2H_2 of higher concentration [18,20], and thus we reduced the C_2H_2 feeds so as to keep small Fe particles active. Figure 4-3a-h shows the SEM images of CNT forests collected in the container bottle. CNTs are sub-millimeter-long and aligned well for both big and small Fe catalyst particles (Ar carrier ferrocene of 250 and 50 cm^3 , respectively) at any condition of 0.73, 0.37 vol% C_2H_2 and 10, 20 min CVD. The amount of CNTs are shown in histogram for different C_2H_2 concentrations (Figure 4-3i–k). With a high C_2H_2 of 1.1 vol% (Figure 4-3i), for an increased CVD time from 10 to 20 min, the amount of CNTs increased only for big Fe particles, meaning that the small catalyst particles were deactivated quickly within around 10 min. With a low C_2H_2 concentration of 0.37 vol% (Figure 4-3k), the increased CVD time from 10 to 20 min resulted in the increased amount of CNTs for both big and small Fe particles, due to the increased lifetime of small Fe particles. But the significant reduction in C_2H_2 to 1/3 resulted in a significant reduction of the amount of CNTs collected, not only due to the reduced amount of synthesized CNTs but also the reduced separation efficiency of the short CNT arrays from the beads. The moderate C_2H_2 concentration of 0.73 vol% (Figure 4-3j) resulted in the increased CNT amount for the increased CVD time from 10 to 20 min for both big and small Fe particles. CNT arrays grew long enough to be well separated after 20 min CVD for the both catalysts, resulting in more than twice the amount of CNTs collected than for 10 min CVD. The moderate C_2H_2 feed gave the best balance between CNT growth rate and catalyst lifetime, and yielded more CNTs (0.62 g, corresponding to the carbon yield of 42%) after 20 min by small Fe particles (50 cm^3 Ar for ferrocene) than the high C_2H_2 feed of 1.1 vol% (0.45 g, corresponding to the carbon yield of 20%).

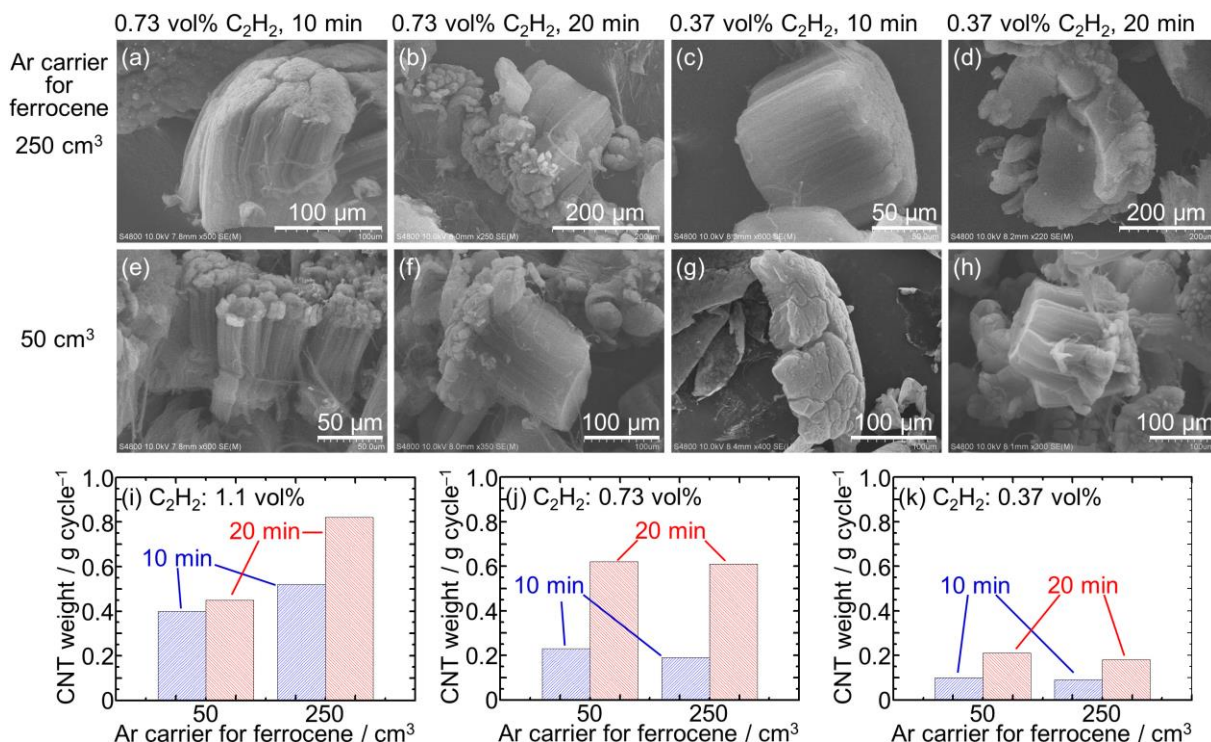


Figure 4-3. (a–h) SEM images and (i–k) weights of CNT arrays collected in the container bottle. The large and small Fe catalyst particles were prepared with (a–d) 250 and (e–h) 50 standard cm³ Ar carrier gas for ferrocene, respectively. The CNTs were synthesized by 10 min CVD for (a, c, e, g), and 20 min CVD for (b, d, f, h). The C₂H₂ concentrations were 0.73 vol% for (a, b, e, f), and 0.37 vol% for (c, d, g, h). The weights of CNTs obtained with C₂H₂ concentrations of (i) 1.1 (the same data as in Fig. 6), (j) 0.73, and (k) 0.37 vol%.

We then examined the diameter of the CNTs synthesized with the moderate C₂H₂ of 0.73 vol% by TEM (Figure 4-4). CNTs by small Fe particles (50 standard cm³ Ar for ferrocene) with 0.73 vol% C₂H₂ (Figure 4-4d–f) had smaller diameter, thinner walls and cleaner surfaces compared with those by the big Fe particles (250 standard cm³ Ar for ferrocene) with either 1.1 vol% (Figure 3-4d–f) and 0.73 vol% (Figure 4-4a–c) C₂H₂. The inset histograms of the CNT diameter distributions as well as the graph of average diameter vs. the depths from the

top of the arrays (Figure 4-4g) show the gradual diameter increase from the top to the bottom for both cases. The average diameter increased from 8.7 to 11.6 nm for the case of big Fe particles with the average diameter of 10.1 nm, while it increased from 5.6 to 7.3 nm for the small Fe particles with the average diameter of 6.5 nm. Because CNTs grow via the root growth mode, the diameter of CNTs increased with time during CVD. Although the CNTs increased in diameter regardless of the Ar carrier volume for ferrocene and thus the Fe particle size, CNTs with smaller diameters nucleated and grew from the smaller catalyst particles, and retained their smaller diameters when CVD was performed at moderate carbon feed of 0.73 vol% C₂H₂. The N₂ adsorption measurement at 77 K showed that the CNTs had a BET specific surface area of 440 m² g⁻¹ for the CNTs synthesized with the small Fe particles and moderate C₂H₂ feed of 0.73 vol% (Figure 4-5), while it was 367 m² g⁻¹ for the big Fe particles and high C₂H₂ feed of 1.1 vol% (Figure 3-5). The value of 440 m² g⁻¹ is about one sixth of the theoretical value for monolayer graphene (2730 m² g⁻¹) and thus about one third that of SWCNTs with closed ends [25,26]. This result indicates that the number of walls of the synthesized CNTs was three on average for the small Fe particles (50 cm³ Ar for ferrocene) with the moderate carbon feed (0.73 vol% C₂H₂).

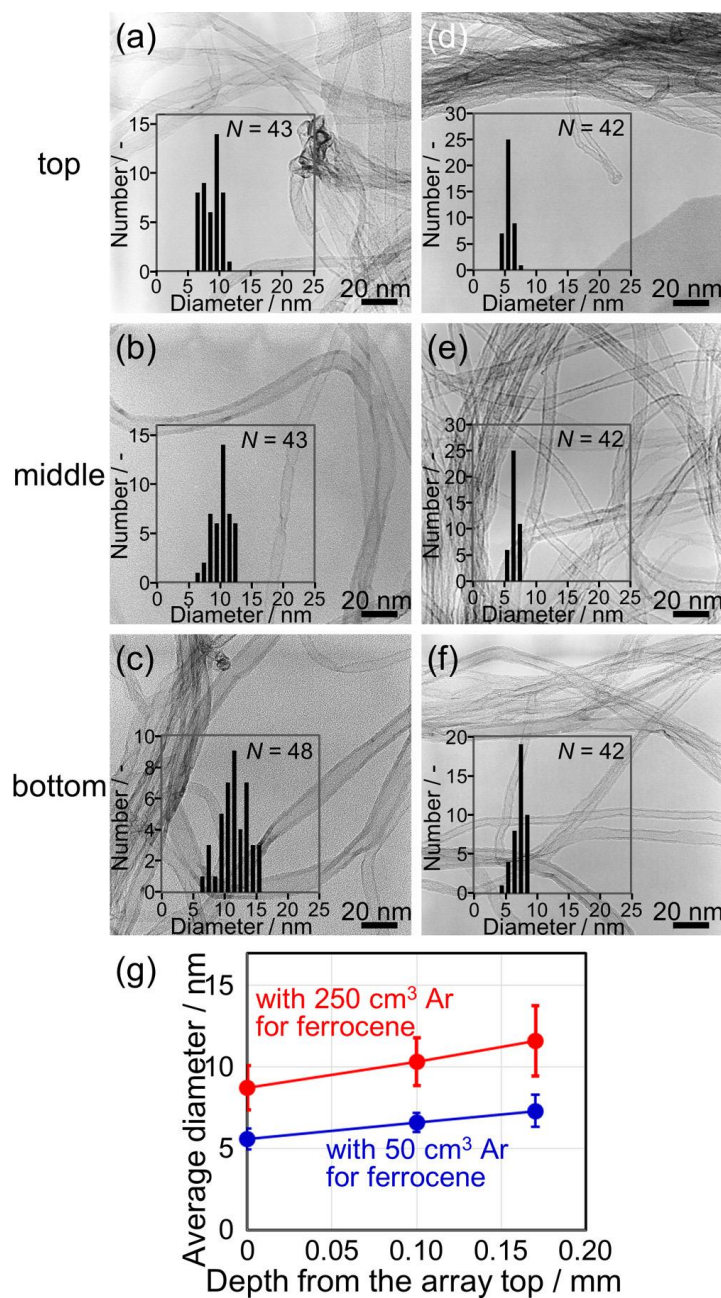


Figure 4-4. TEM images and diameter distributions of CNTs synthesized with 0.73 vol% C_2H_2 for large and small Fe catalyst particles prepared with (a–c) 250 and (d–f) 50 standard cm^3 Ar carrier gas for ferrocene, respectively: (a, d) top, (b, e) middle, and (c, f) bottom of a single piece of CNTs taken out of the array. In (g), the changes in the average diameter of the CNTs with 250 cm^3 and 50 cm^3 Ar carrier gas for ferrocene are plotted against the depth from the top of the CNT arrays. The error bars show the standard deviation.

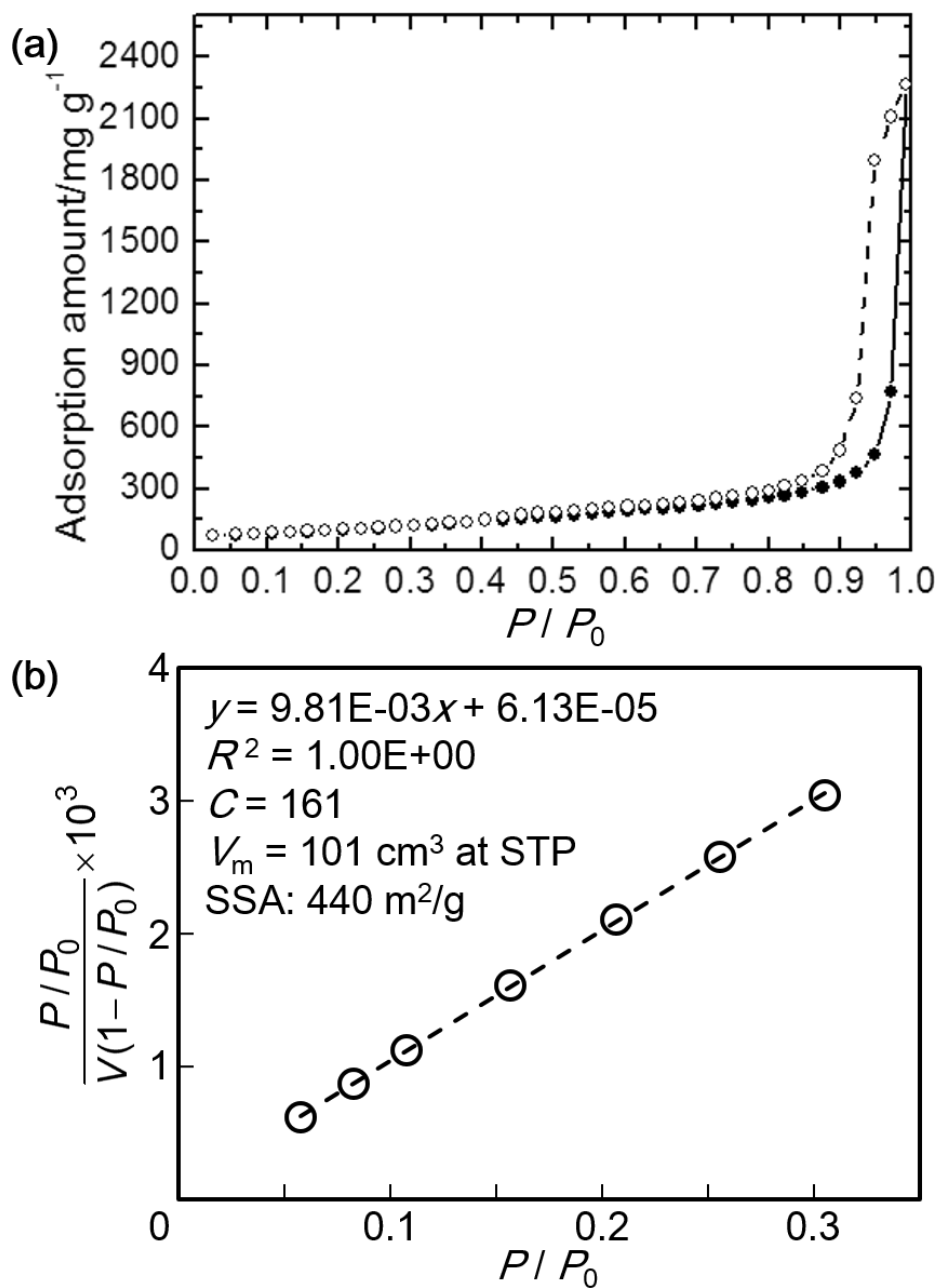


Figure 4-5. (a) N₂ adsorption isotherm at 77 K and (b) corresponding BET plot of the sub-millimeter-long CNTs. The CNT sample is the same as that in Figure 4-4d-f and was synthesized by small Fe particles (50 cm³ Ar carrier gas for ferrocene) with 0.73 vol% C₂H₂. The closed and open symbols in (a) indicate adsorption and desorption processes, respectively.

We analyzed the purity of CNTs synthesized with small Fe particles (50 cm³ Ar gas for ferrocene) and moderate carbon feed (0.73 vol% C₂H₂) by XRF and TG-DTA. We prepared two CNT papers for analysis by XRF. One paper is prepared by dispersing CNT powders (3 mg) in ethanol (30 mL) by ultrasonication (3 min) and filtrating all of the dispersion. The other is prepared by dispersing CNT powders (4 mg) with sodium dodecylbenzenesulfonate surfactant (SDBS, 50 mg) in water (40 mL) by ultrasonication (3 min), centrifuging the dispersion mildly (3000 rpm, 10 min), and then filtrating the supernatant. Note that no other purification, such as acid treatment, was applied in making these papers. Table 4-1 shows the elemental composition of these papers. The paper The XRF result of CNT paper prepared by dispersion in ethanol followed by vacuum filtration shows that the CNTs prepared by filtrating all dispersion without centrifugation (and thus without any purification) had a high carbon purity of 99.8 wt% (Table 4-1). Such high purity is sometimes reported for SWCNT arrays synthesized on flat substrates [6] but not for FBCVD. The other paper prepared by filtrating the supernatant after a mild centrifugation showed even smaller contaminations of Al and Fe (1/6–1/7 of the paper without centrifugation). These Fe and Al contaminations should be contained mainly as powders just mixing with CNTs, which are easily separated from the CNT dispersion by settling during centrifugation. Note that if these catalyst impurities are encapsulated by CNTs, they cannot be removed just by dispersion and centrifugation. The TG-DTA result shows that the as-synthesized CNT powder had a carbon purity of 99.6 wt% with amorphous carbon of ~2 wt% and a high oxidation stability of ~650 °C (Figure 4-6a). We analyzed the compositions of the ash after TG-DTA by EDX (Figure 4-6b). The ash contained Fe and Al, which are attributed mainly to the Fe catalyst and AlOx support layer being scraped off during the vigorous fluidization for CNT separation. The small Si content can be attributed to the reactor tube made of quartz glass being slightly scraped off. The weight of the ash was 0.05 mg, which is in good agreement with the 0.4 wt%

impurity in the 10.2 mg CNTs used for the TG-DTA measurement when we take into account the weight increase from 0.019 mg Fe in the CNT powder to 0.027 mg Fe₂O₃ in the ash. There was a slight deviation in the carbon purity and Fe/Al ratio between the two measurements (XRF in Table 4-1 and TG-DTA with SEM-EDS in Figure 4-6). However, it is clear that the CNTs synthesized by our FBCVD method with careful control of the catalyst and carbon feeds gave 99.6 – 99.8 wt%-pure sub-millimeter-long CNT arrays, and that the small catalyst contamination can be reduced further easily by dispersion and centrifugation. Such pure and long CNTs are attractive especially for use as electrodes and 3D current collectors in secondary batteries [27] and electrochemical capacitors [28].

Table 1 – Elemental composition of the CNT papers* by XRF

Element	C	O	Al	Si	Fe
without centrifugation	99.81	0.10	0.06	0.01	0.02
with centrifugation**	99.84	0.14	0.01	0.01	0.003

*No chemical purification was applied in making the CNT papers.

**S is also contained at 0.61 wt% due to SDBS used in dispersion.

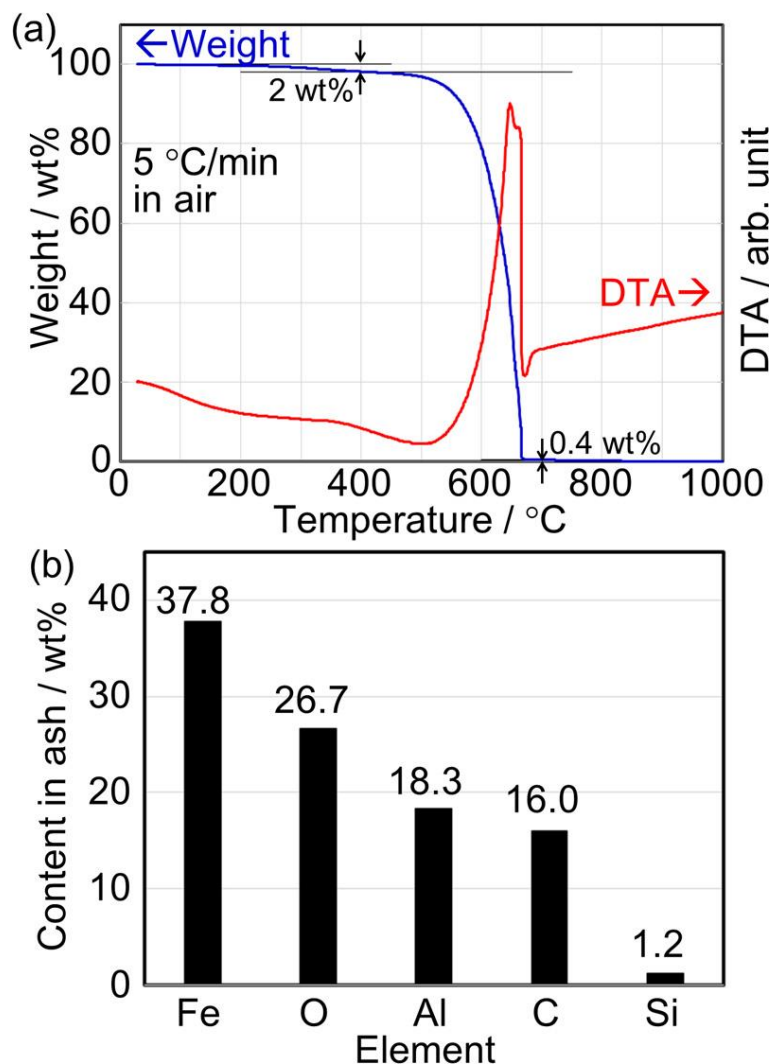


Figure 4-6. TG-DTA curves of the CNTs synthesized by small Fe particles (50 cm^3 Ar carrier for ferrocene) with 0.73 vol% C_2H_2 . The sample was the same as that in Figure 4-4d–f. (b) Elemental composition of the ash after the TG-DTA measurement.

We analyzed the composition of the carbon-containing species in the effluent gas from the FBCVD reactor by GC-FID at 2 min interval during 20 min CVD (Figure 4-7). We first supplied the CVD gas to the tube filled with pristine beads at room temperature (r. t.) to eliminate the influence of the catalytic reaction, and used the data as the reference. For the

effluent gas during CVD, CH_4 , C_2H_2 , CO_2 and C_2H_4 were the main carbon containing species. Small peaks for C_2H_6 and CO were also detected. The contents of CO_2 and CO were around 0.1 and 0.03 vol%, respectively, which are somewhat higher than the expected value from the 0.06 vol% H_2O feed, presumably due to some leakage and/or adsorbed species on the beads. There were two stages for CNT growth. One is the early stage from 0 to 10 min, where the conversion of C_2H_2 to undetectable carbon (mostly CNTs) was as high as 70–80%. The other is the later stage from 10 to 20 min, where the catalyst gradually deactivated and the conversion decreased to 70–40%. The total conversion was around 60%. There is a deviation in the conversion of C_2H_2 to undetectable carbon (~60% by GC) and the carbon yield of CNTs (42% from the weight of collected CNTs). To clarify the reason, we analyzed the CNT arrays on beads without separating them by the gas flow (Figure 4-8). Both the pristine beads and the beads with CNTs had certain distributions in radius. The CNT arrays on beads also had a certain distribution in height and were shorter on the beads (Figure 4-8d) than in the container bottle (Figure 4-2k). The catalyst line directly feeding the catalyst vapors to the center of the bed (Figure S1) prevented the stacking of the distributor while caused some distribution in the catalyst thickness among different beads, resulting in the distribution in the CNT array height. It is probable that long CNT arrays were separated from the beads while the short CNT arrays remained on the beads, resulting in the smaller CNT yield than the C_2H_2 conversion. Development of more efficient separation method is now underway.

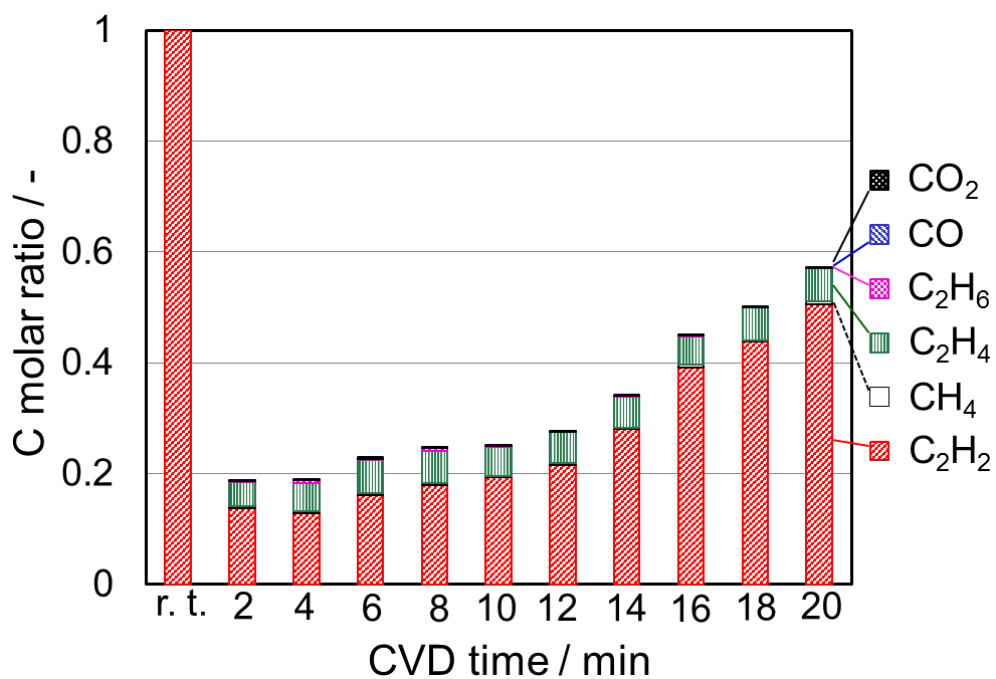


Figure 4-7. Composition of the effluent gas from the FBCVD reactor for different CVD time analyzed by GC. CVD is carried out with the moderate carbon feed of 0.73 vol% C₂H₂ and the small Fe particles with 50 cm³ Ar carrier gas for ferrocene.

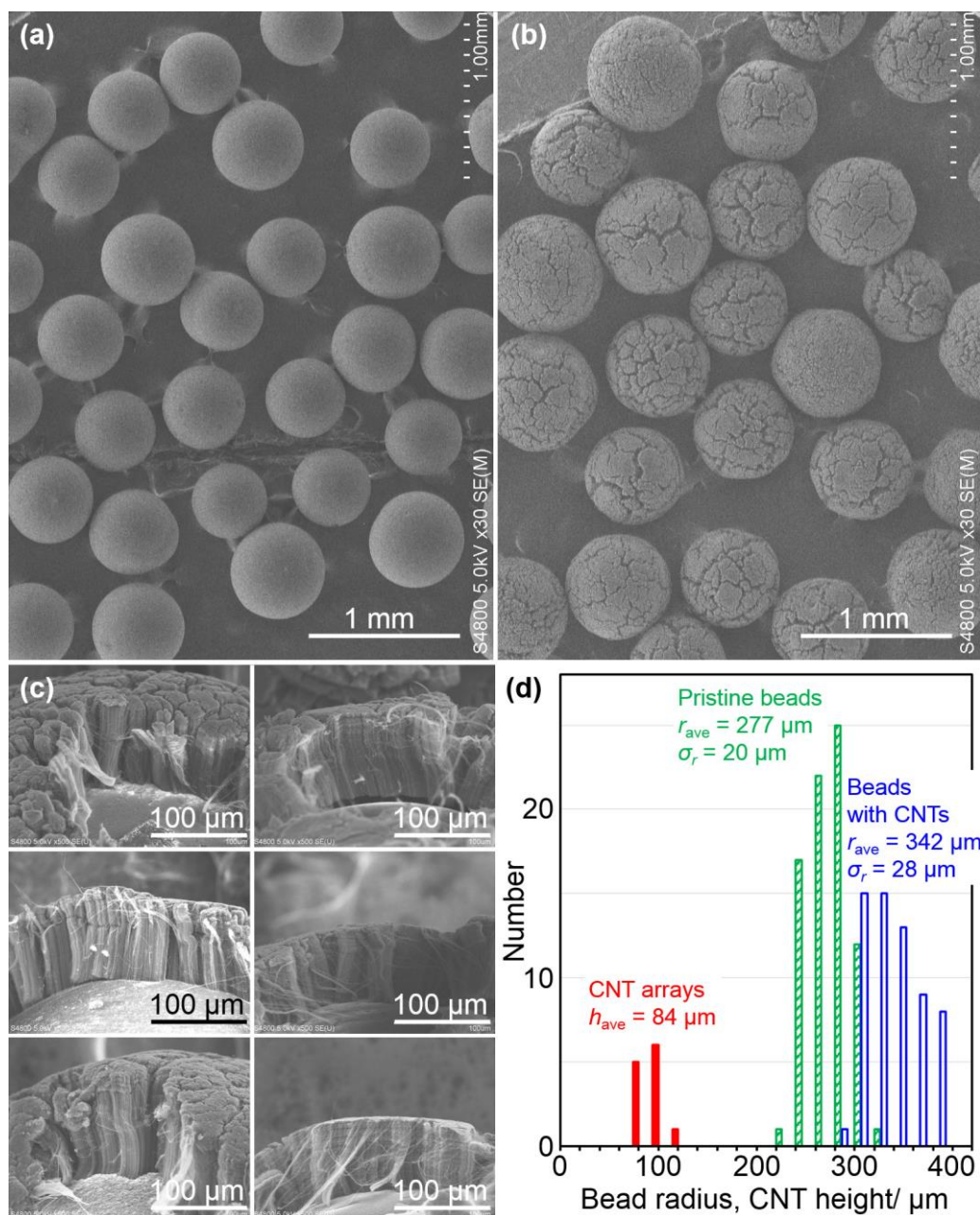


Figure 4-8. Low magnification SEM images of (a) pristine beads and (b) beads with CNT arrays. (c) Enlarged SEM images of the sidewalls of the CNT arrays on beads. (d) Histogram of the radius of the pristine beads, that of the beads with CNT arrays, and the height of the CNT arrays. The CNTs were synthesized by 20 min CVD using 1.1 vol% C_2H_2 and small Fe catalyst particles (50 standard cm^3 Ar carrier gas for ferrocene). The beads with CNTs were taken out from the reactor without separation by the gas flow.

4.6 Conclusions

Targeting at the production of CNTs with improved quantity and quality, careful control was made over the catalyst and CVD conditions. By decreasing the total Ar carrier gas for ferrocene supply to 50 from 250 cm³, the size of the Fe catalyst was reduced. But smaller catalyst particles resulted in the reduced amount of CNTs with a 1.1 vol% C₂H₂ for CVD time of 20 min. Small catalyst particles showed similar amount with large catalyst particles when CVD is carried out for 10 min with a 1.1 vol% C₂H₂, and thus the reduced CNT amount by 20 min CVD is attributed to the reduced lifetime of small catalyst particles. C₂H₂ feed was then reduced to 0.73 and 0.37 vol% to avoid the catalyst deactivation due to carbonization. CNT amounts were reduced for 10 min CVD but they increased with increased CVD time for 20 min, showing the increased lifetime of small catalyst particles at a reduced C₂H₂ feed. 0.73 vol% was optimum for the C₂H₂ feed, which realize both fair CNT growth rate and fair catalyst lifetime. Resulting CNTs had a reduced average diameter of 6.5 nm, an increased specific surface area of 440 m²/g, an increased carbon purity of 99.6–99.8 wt%, at a similar CNT amount of 0.61 g/cycle (11 nm, 367 m²/g, 97.2 wt%, and ~0.8 g/cycle, respectively, in Chapter 3). Such FWCNTs with a sub-millimeter length are attractive for many applications for electrodes/current collectors in batteries/capacitors and wirings/electrodes in flexible electronic devices. Additionally, the conclusion "moderating the feeds for both catalyst and carbon sources for improved quantity and quality of CNTs" should be common for many CNT production processes.

References

- [1] H. J. Dai, A. G. Rinzler, P. Nikolaev, A. Thess, D. T. Colbert, R. E. Smalley, Chem. Phys. Lett. 260 (1996) 471.
- [2] J. Kong, A. M. Cassell, H. J. Dai, Chem. Phys. Lett. 292 (1998) 567.
- [3] J. H. Hafner, M. J. Bronikowski, B. R. Azamian, P. Nikolaev, A. G. Rinzler, D. T. Colbert, K. A. Smith, R. E. Smalley, Chem. Phys. Lett. 296 (1998) 195.
- [4] M. Su, B. Zheng, J. Liu, Chem. Phys. Lett. 322 (2000) 321.
- [5] J. Kong, H. T. Soh, A. M. Cassell, C. F. Quate, H. J. Dai, Nature 395 (1998) 878.
- [6] K. Hata, D. N. Futaba, K. Mizuno, T. Namai, M. Yumura, S. Iijima, Science 306 (2004) 1362.
- [7] Y. M. Li, W. Kim, Y. G. Zhang, M. Rolandi, D. W. Wang, H. J. Dai, J. Phys. Chem. B 105 (2001) 11424.
- [8] S. M. Huang, M. Woodson, R. Smalley, J. Liu, Nano Lett. 4 (2004) 1025.
- [9] M. S. He, X. J. Duan, X. Wang, J. Zhang, Z. F. Liu, C. Robinson, J. Phys. Chem. B 108 (2004) 12665.
- [10] G. L. Hornyak, L. Grigorian, A. C. Dillon, P. A. Parilla, K. M. Jones, M. J. Heben, J. Phys. Chem. B 106 (2002) 2821.
- [11] L. M. Wagg, G. L. Hornyak, L. Grigorian, A. C. Dillon, K. M. Jones, J. Blackburn, P. A. Parilla, M. J. Heben, J. Phys. Chem. B 109 (2005) 10435.

-
- [12] G. H. Jeong, A. Yamazaki, S. Suzuki, H. Yoshimura, Y. Kobayashi, Y. Homma, J. Am. Chem. Soc. 127 (2005) 8238.
- [13] S. J. Han, T. K. Yu, J. Park, B. Koo, J. Joo, T. Hyeon, S. Hong, J. Im, J. Phys. Chem. B 108 (2004) 8091.
- [14] H. J. Jeong, K. H. An, S. C. Lim, M. S. Park, J. S. Chang, S. E. Park, S. J. Eum, C. W. Yang, C. Y. Park, Y. H. Lee, Chem. Phys. Lett. 380 (2003) 263.
- [15] Q. Fu, S. M. Huang, J. Liu, J. Phys. Chem. B 108 (2004) 6124.
- [16] C. L. Cheung, A. Kurtz, H. Park, C. M. Lieber, J. Phys. Chem. B 106 (2002) 2429.
- [17] C. Lu, J. Liu, J. Phys. Chem. B 110 (2006) 20254.
- [18] K. Hasegawa, S. Noda, ACS Nano 5 (2011) 975.
- [19] S. Noda, K. Hasegawa, H. Sugime, K. Kakehi, Z. Zhang, S. Maruyama, Y. Yamaguchi, Jpn. J. Appl. Phys. 46 (2007) L399.
- [20] K. Hasegawa, S. Noda, Carbon 49 (2011) 4497.
- [21] Z. Chen, D. Y. Kim, K. Hasegawa, S. Noda, ACS Nano 7 (2013) 6719.
- [22] H. Sugime, S. Noda, Carbon 48 (2010) 2203.
- [23] K. Kakehi, S. Noda, S. Maruyama, Y. Yamaguchi, Jpn. J. Appl. Phys. 47 (2008) 1961.
- [24] S. Noda, K. Hasegawa, H. Sugime, K. Kakehi, Z. Zhang, S. Maruyama, Y. Yamaguchi, Jpn. J. Appl. Phys. 46 (2007) 399.
- [25] T. Hiraoka, A. Izadi-Najafabadi, T. Yamada, D. N. Futaba, S. Yasuda, O. Tanaike, H. Hatori, M. Yumura, S. Iijima, K. Hata, Adv. Fun. Mater. 20 (2010) 422.

-
- [26] A. Peigney, C. Laurent, E. Flahaut, R. R. Bacsa, A. Rousset, Carbon 39 (2001) 507.
- [27] S. W. Lee, B. M. Gallant, Y. Lee, N. Yoshida, D. Y. Kim, Y. Yamada, S. Noda, A. Yamada, and Y. Shao-Horn, Energy Environ. Sci. 5 (2012) 5437.
- [28] R. Quintero, D. Y. Kim, K. Hasegawa, Y. Yamada, A. Yamada, S. Noda. RSC Adv. 4 (2014) 8230.

Chapter 5 – Conclusions

CNTs having high electric conductivity, flexibility, surface area and thermal, chemical and mechanical stability are attractive candidates for many kinds of applications. There are various potential applications for CNTs in the field of electric energy storage devices, for example, mobile electronics, electric vehicles, and the storage of renewable energies. Many researchers put their interests in using CNTs in electrochemical energy storage application, and try to improve their conductivity by different dispersion method or doping them with other materials, but it is still far away from industrial application because of the insufficient understanding of their synthesis mechanisms. Thus, understanding the mechanism for and developing practical process of their production are crucial for breakthrough toward their nanotechnology application.

When we consider the production of CNTs at a low cost below 100 USD/kg, high-purity experimental-grade feed gases need be replaced with cheaper ones. Especially, H_2 is a common feed gas in most CVD processes for CNT production, and hence, there is a practical motivation for replacing the high purity H_2 with the low purity H_2 that is available at a low cost and/or as a byproduct in chemical factories. We examined the use of low purity H_2 (96 vol% H_2 with 4 vol% CH_4) in CVD using a C_2H_2 feedstock, and obtained SWCNTs with unexpectedly smaller diameters, larger height, and higher quality compared with those grown using pure H_2 .

We used the low purity H_2 in the millimeter-scale growth of SWCNTs from 0.3 vol% C_2H_2 on flat substrates with an Fe/Al_2O_x catalyst, and unexpectedly found that SWCNTs grew taller with the low purity H_2 . Raman scattering spectroscopy showed that the taller SWCNTs grown

with low purity H_2 had an improved quality. AFM showed that Fe particles were smaller and denser and TEM showed that SWCNTs had smaller diameters with the low purity H_2 . XPS revealed that a small amount of carbon is deposited on/in Fe particles with the low purity H_2 . The 1 vol% CH_4 in 25 vol% H_2 / 74 vol% Ar was found responsible for that carbon, which presumably kept Fe particles small and dense by reducing their surface energy. These effects were observed only for CH_4 ; CNTs with lower quality grew when C_2H_4 or C_2H_2 were fed with H_2 . The low reactivity of CH_4 is considered to be essential to just stabilize the Fe particles but not to grow CNTs. This CH_4 -assisted CVD is an efficient and practical method that uses H_2 containing CH_4 that is available as a byproduct in chemical factories.

Based on the understanding of the synthesis mechanism for CNTs on flat substrates, producing CNTs with increased scale and improved purity for practical application is another goal during my PhD study. During mass production of CNTs by FBCVD, to make the sufficient heating of gas is important. From Chapter 3, we proposed and developed a new FBCVD reactor with internal heat-exchanger and preheater with the aim of efficiently synthesizing CNTs with controlled structure. The new reactor realized uniform heating of the bed even for a space velocity as high as 3600 h^{-1} (corresponding to a gas residence time $<0.3 \text{ s}$ at $745 \text{ }^\circ\text{C}$) and direct feeding of cold catalyst vapor source into the bed. Using this new reactor, sub-millimeter-long CNTs were semi-continuously produced from C_2H_2 using a Fe/AlO_x catalyst at $745 \text{ }^\circ\text{C}$ with careful control of the structures of the catalyst and CNTs. With the high production efficiency (all processes for catalyst re-deposition, catalyst reduction, CNT growth, CNT separation, and removal of residual carbons were performed in a single fluidized bed reactor), it enabled semi-continuous production of submillimeter-long CNTs with an increased reactor volume of $\sim 0.5 \text{ L}$ ($\sim 1 \times 10^3 \text{ h}^{-1}$). At the beginning, semi-continuous synthesis of CNTs with amount of around 0.8 g/cycle with 11 nm diameter in

average was realized under the condition of 1.1 vol% C₂H₂ and 250 standard cm³. However, CNTs had a large average diameter of 11 nm and a reduced carbon purity of 97.2 wt%.

Hereafter, the Ar carrier gas volume for ferrocene supply was carefully controlled because the amount of the Ar carrier determines the nominal thickness of the Fe layer. The nominal thickness and size of the catalyst Fe particles could be easily controlled by the amount of ferrocene feed, whereas it was difficult to control the number density of the Fe particles, which remained at around 10¹⁰–10¹¹ cm⁻² (one order of magnitude smaller than those prepared on flat substrates by sputtering). With a high C₂H₂ feed (1.1 vol% C₂H₂), the weight of produced CNTs remained almost constant for different Fe catalysts for a short reaction time (10 min) whereas it was larger for higher Fe feed for a longer reaction time (20 min), meaning that the small Fe particles were easily deactivated within 10 min. A moderate C₂H₂ feed (0.73 vol%) increased the catalyst lifetime to ~20 min and realized the efficient production of small diameter FWCNTs (6.5 nm on average) at a purity of 99.6–99.8 wt% and a carbon yield >40 at%. This semi-continuous FBCVD process with careful control of the CNT structure can be used to produce CNTs for practical applications.

In summary, I have developed the CH₄-assisted CVD method which yields longer VA-SWCNTs with reduced diameters and the semi-continuous FBCVD process using a heat exchange reactor which yields over 99.6 wt%-pure submillimeter-long FWCNTs with a reduced diameter (6.5 nm in average) at a high carbon yield of 42 at%. The common key for the controlled production of CNTs is: moderating the catalyst feed to yield small catalyst particles and moderating the carbon feed to keep such small catalyst particles active.

Supporting information

Detailed structure of the bottom of the FBCVD reactor with an internal preheater and heat exchanger in Chapter 3:

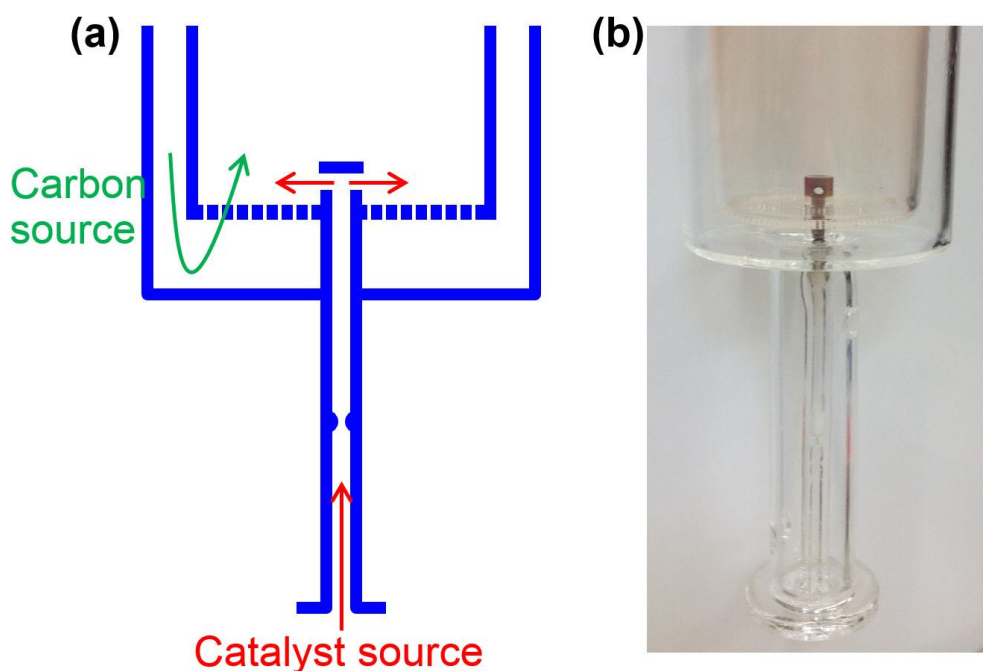


Figure S1. A schematic (a) and a photo (b) showing the detailed structure of the bottom of the FBCVD reactor with an internal preheater and heat exchanger. The catalyst line penetrates the distributor to prevent the catalyst deposition on the distributor. Catalyst vapors were fed without preheating and at a high velocity in order to minimize the catalyst deposition on the inner wall of the catalyst line. Some catalyst deposits on the inner wall of the catalyst line, but there is no carbon source gas and thus the stacking of the catalyst line due to the carbon deposition is prevented. Ar carrier gas is continuously fed at 1 slm through the catalyst line whole over the cycle in order to prevent the beads to fall down the catalyst line.

Fluent simulation and heat transfer for old singular tube (a) and the new coaxial double tube in Chapter 3:

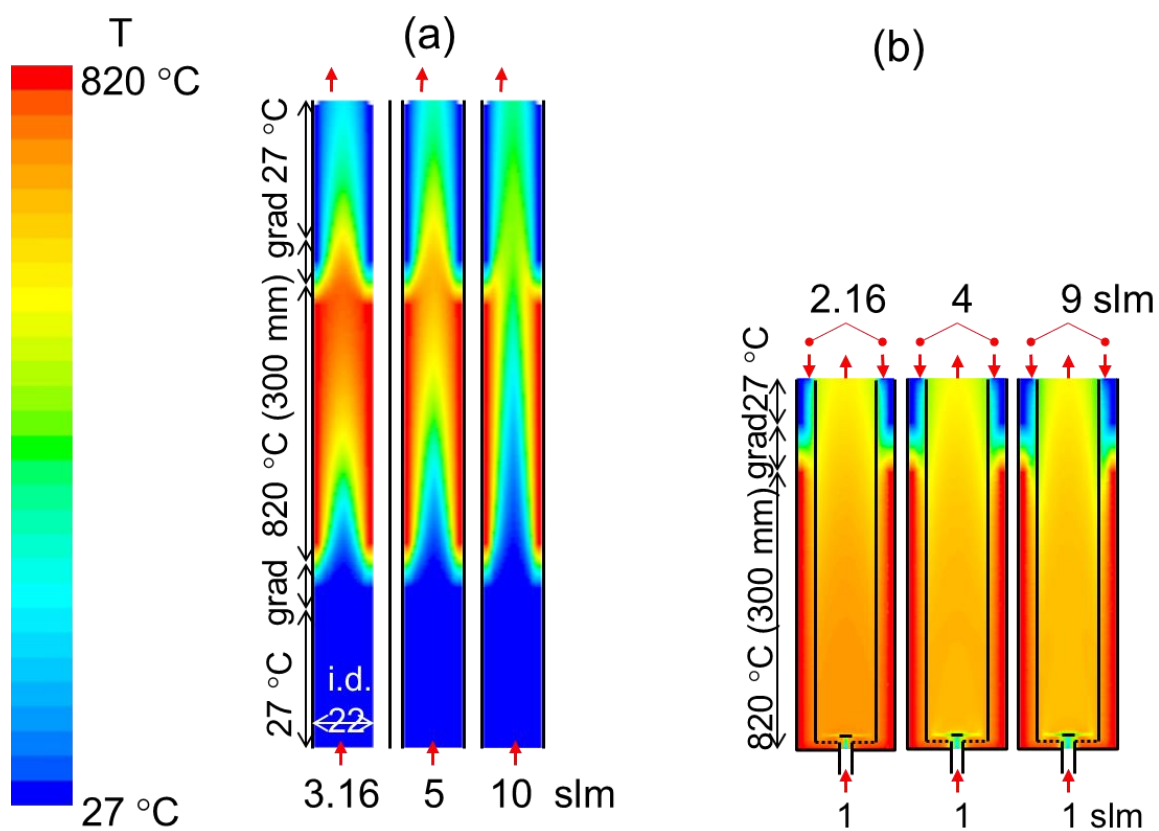


Figure S2. Fluent simulation for the old singular tube (a) and the new coaxial double tube (b) with different flow rate of gas.

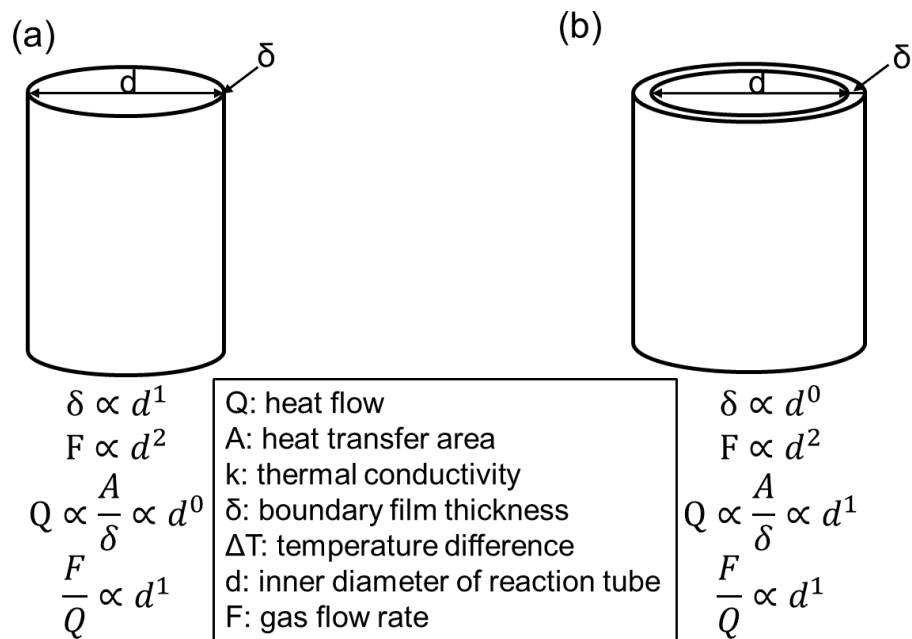


Figure S3. Schematics of the old singular tube (a) and the new coaxial double tube (b),

bottom shows the name of each factor and the relationships between each other.

Copy right for Figure 1-1:

Copyright Clearance

Content: Schematics for single wall carbon nanotubes (SWCNTs) and multi-wall carbon nanotubes (MWCNTs).

Author: Shigeo Maruyama.

Access: <http://www.photon.t.u-tokyo.ac.jp/index.html>.

Permission for this particular request is granted for print and electronic formats, and translations, at no charge. Schematics may be modified. Appropriate credit should be given. Please print this page for your records and provide a copy to your publisher. Appropriate credit should read: "Reprinted with permission from {COMPLETE REFERENCE CITATION, <http://www.photon.t.u-tokyo.ac.jp/index.html> }.





Shigeo MARUYAMA Ph.D.

Professor

Department of Mechanical Engineering

The University of Tokyo

Copy right for Figure 1-6:

**RightsLink®**

[Home](#) [Create Account](#) [Help](#)

Title: Atomic-Scale In-situ Observation of Carbon Nanotube Growth from Solid State Iron Carbide Nanoparticles

Author: Hideto Yoshida, Seiji Takeda, Tetsuya Uchiyama, Hideo Kohno, and Yoshikazu Homma

Publication: Nano Letters

Publisher: American Chemical Society

Date: Jul 1, 2008

Copyright © 2008, American Chemical Society

☐ Enable Auto Login

[Forgot Password/User ID?](#)

[If you're a copyright.com user, you can login to RightsLink using your copyright.com credentials. Already a RightsLink user or want to learn more?](#)

Quick Price Estimate

Permission for this particular request is granted for print and electronic formats, and translations, at no charge. Figures and tables may be modified. Appropriate credit should be given. Please print this page for your records and provide a copy to your publisher. Requests for up to 4 figures require only this record. Five or more figures will generate a printout of additional terms and conditions. Appropriate credit should read: "Reprinted with permission from {COMPLETE REFERENCE CITATION}. Copyright {YEAR} American Chemical Society." Insert appropriate information in place of the capitalized words.

If credit is given to another source for the material you requested, permission must be obtained from that source.

- Number of Table/Figure/Micrographs is a required field. Please make a selection.

I would like to...
Requestor Type
Portion
Number of Table/Figure/Micrographs
Format
Select your currency
Quick Price

reuse in a Thesis/Dissertation

Non-profit

Table/Figure/Micrograph

1

Electronic

JPY - ¥

Click Quick Price

This service provides permission for reuse only. If you do not have a copy of the article you are using, you may copy and paste the content and reuse according to the terms of your agreement. Please be advised that obtaining the content you license is a separate transaction not involving Rightslink.

Note: Individual Scheme and Structure reuse is free of charge and does not require a license. If the scheme or structure is identified as a Figure in the article, permission is required.

To request permission for a type of use not listed, please contact [the publisher](#) directly.

Copyright © 2014 Copyright Clearance Center, Inc. All Rights Reserved. [Privacy statement](#). Comments? We would like to hear from you. E-mail us at customerservice@copyright.com

Copy right for Figure 1-8:

**ACS Publications**
MOST TRUSTED. MOST CITED. MOST READ.

RightsLink®

[Home](#)[Create Account](#)[Help](#)

Title: In situ Observations of Catalyst Dynamics during Surface-Bound Carbon Nanotube Nucleation

Author: Stephan Hofmann et al.

Publication: Nano Letters

Publisher: American Chemical Society

Date: Mar 1, 2007

Copyright © 2007, American Chemical Society

User ID

Password

☐ [Enable Auto Login](#)

[Forgot Password/User ID?](#)

If you're a [copyright.com](#) user, you can login to RightsLink using your [copyright.com](#) credentials. Already a [RightsLink](#) user or want to [learn more?](#)

PERMISSION/LICENSE IS GRANTED FOR YOUR ORDER AT NO CHARGE

This type of permission/license, instead of the standard Terms & Conditions, is sent to you because no fee is being charged for your order. Please note the following:

- Permission is granted for your request in both print and electronic formats, and translations.
- If figures and/or tables were requested, they may be adapted or used in part.
- Please print this page for your records and send a copy of it to your publisher/graduate school.
- Appropriate credit for the requested material should be given as follows: "Reprinted (adapted) with permission from (COMPLETE REFERENCE CITATION). Copyright (YEAR) American Chemical Society." Insert appropriate information in place of the capitalized words.
- One-time permission is granted only for the use specified in your request. No additional uses are granted (such as derivative works or other editions). For any other uses, please submit a new request.

If credit is given to another source for the material you requested, permission must be obtained from that source.

[BACK](#)

[CLOSE WINDOW](#)

Copyright © 2014 [Copyright Clearance Center, Inc.](#) All Rights Reserved. [Privacy statement](#). Comments? We would like to hear from you. E-mail us at customerservice@copyright.com

Acknowledgements

At first, I would like to express my deep respect and gratitude to my thesis advisor, Professor Suguru Noda, who gave me this precious chance to study in his lab. He has taught me many things since I joined his lab. Many thanks for his advice, patience and understanding, I grow up very much both in my life and research during these three years. I have been greatly influenced by his creative approach to science. Particularly I am surprised that he knows and understands every group member very well even in such a big group. This three year experience in his group will benefit me the rest of my life. I would also like to thank Professor Yukio Yamaguchi for all his support after moving to Waseda University and his precious advices for my PhD defence.

I would also like to thank my PhD thesis committee, Prof. Yukio Yamaguchi, Prof. S. Ted Oyama, Prof. Tatsuya Okubo, Prof. Shigeo Maruyama, Prof. Ryuji Kikuchi, and Prof. Suguru Noda. I have learned a lot of knowledge from your careful review of my PhD thesis and valuable comments on my defence.

It is very joyful to work with Dr. Dong Young Kim, who advised me a lot and helped me start experiments for SWCNT synthesis on substrates to understand the basic theory of them and learning the technic for CNT mass production by FBCVD. Many thanks to Dr. Kei Hasegawa for the great discussion for my experiments and technician Toshio Osawa for his support on constructing of the FBCVD apparatus. I am also gratitude to all the help and discussions from all the group members in Noda group.

I greatly appreciate the China Scholarship Council (CSC), which financially supported my stay in Japan and grant me the opportunity to pursue my PhD study here.

Finally, I appreciate all the great support and encouragement from my family and friends.

Publication list

Peer review journals

1. Z. Chen, D.Y. Kim, K. Hasegawa, T. Osawa, and S. Noda, "Over 99.6 wt%-pure, sub-millimeter-long carbon nanotubes realized by fluidized-bed with careful control over catalyst and carbon feeds," Carbon, 2014, accepted.
2. Z. Chen, D.Y. Kim, K. Hasegawa, and S. Noda, "Methane-assisted chemical vapor deposition yielding millimeter-tall single-wall carbon nanotubes of smaller diameter," ACS Nano 7 (8),6719-6728 (2013).
3. E. Ou , X. Zhang , Z. Chen, Y. Zhan, Y. Du, G. Zhang, Y. Xiang, Y. Xiong, W. Xu, Macroscopic, free-standing Ag-reduced, graphene oxide janus films prepared by evaporation-induced self-assembly, Chemistry - A European Journal, 17 (32), 8789-8793 (2011).
4. G. Wu, Z. Chen, S. Zeng, P. Yu, Y. Xie, Y. Xiong, W. Xu, UV exposure effects on photoinitiator-grafted styrene-butadiene-styrene triblock copolymer, Journal of Applied Polymer Science, 20 (5), 2627-2631 (2011).
5. Z. Chen, S. Pan, H. Yin, L. Zhang, E. Ou, Y. Xiong, W. Xu, Facile synthesis of superhydrophobic TiO₂/Polystyrene core-shell microspheres, eXPRESS Polymer Letters, 5 (1), 38-46 (2011).
6. S. Pan, R. Guo, J. Peng, Z. Chen, H. Liu, W. Xu, A facile method to fabricate hierarchical particulates for superhydrophobic surfaces by diisocyanate reactions. Journal of Adhesion Science and Technology, 25 (12), 1393-1401, (2011)
7. L. Zhang, Y. Xiong, E. Ou, Z. Chen, Y. Xiong, W. Xu, Preparation and properties of nylon 6/carboxylic silica nanocomposites via in situ polymerization, Journal of Applied Polymer Science, 122 (2), 1316-1324 (2011).
8. H. Yin, Z. Xiong, S. Yan, Z. Chen, Y. Xiong, W. Xu, UV-curable hybrids of hyperbranched and linear polyurethane dispersions, Journal of Macromolecular Science, Part B: Physics, 51 (2), 209–223, (2012).

Conference contributions

1. Z. Chen, et al. The Fifth International Conference on the Science and Application of Nanotubes (NT14), Los Angeles, California, USA, June 2-6, 2014.
2. Z. Chen, et al. The Sixth Guadalupe Workshop 2013, San Antonio, Texas, USA, April 12-16, 2013.
3. Z. Chen, et al. The Thirteenth International Conference on the Science and Application of Nanotubes (NT12), Brisbane, Australia, June 25-29, 2012.
4. Z. Chen, et al. The SCEJ 79th Annual Meeting, March 18-20, 2014, Gifu, Japan.
5. Z. Chen, et al. The 46th Fullerenes-Nanotubes-Graphene General Symposium, March 2014, Tokyo, Japan.
6. Z. Chen, et al. The SCEJ 45th Auttom Meeting, Sepertember 2013, Okayama, Japan.
7. Z. Chen, et al. The 44th Fullerenes-Nanotubes-Graphene General Symposium, March 2013, Tokyo, Japan.
8. Z. Chen, et al. The SCEJ 44th Auttom Meeting, Sepertember 2012, Sendai, Japan.

August 2014

Zhongming CHEN

Tokyo, Japan